Ph.D. DISSERTATION

Efficient photoelectrochemical water splitting electrodes using nanostructures and catalysts

By

Dinsefa Mensur Andoshe

August 2017

SEOUL NATIONAL UNIVERSITY

COLLEGE OF ENGINEERING

DEPARTMENT OF MATERIALS SCIENCE AND ENGINEERING

Efficient photoelectrochemical water splitting electrodes using nanostructures and catalysts

Advisor: Prof. Ho Won Jang

By

Dinsefa Mensur Andoshe

A thesis submitted to the Graduate Faculty of Seoul National University in partial fulfillment of the requirements for the Degree of Doctor of Philosophy

Department of Materials Science and Engineering

May 2017

Approved

By

Chairman of Advisory Committee: Seungwu Han

Vice-chairman of Advisory Committee: Ho Won Jang

Advisory Committee: Ki Tae Nam

Advisory Committee: Soo Young Kim

Advisory Committee: Chul-Ho Lee

Abstract

The Sustainable and efficient conversion of solar energy to transportable green energy and storable fuels, hydrogen, represents a solution to the energy crisis and can decreases the consumption of fossil fuels, which are mainly responsible for the rise of global temperature. Therefore, this thesis presents about photoelectrochemical water splitting electrodes, silicon based photocathode and titanium oxide based photoanode, in three main chapters. The second and third chapters are focus on silicon based photocathode. The solar to hydrogen conversion efficiency of a silicon photoelectrode is suppressed by overpotential, high reflectance and instability in the liquid electrolytes. These drawbacks were managed by synthesizing a multifunctional metal oxide and metal chalcogenides on the surface of silicon. First, the limitation of *p*-type silicon for solar water splitting coped using a solution processed TiO_2 nanorods with controlled heights and diameters on a 4-inch *p*-type silicon wafer. The overpotential of bare *p*-type silicon photocathode was decreased from –0.75 V vs. RHE to 0.0 V vs RHE after catalytic TiO_2 NRs were grown. The reflectance of silicon was decreased from about 37 % (arithmetic mean) to 1.4 %. The dramatic reduction of reflectance of silicon enhances the charge generation efficiency of the photocathode and resulted in increment of the saturated current density from 32 to 40 mA cm^{-2}. After very small Pt nanoparticle, 1–2.5 nm diameter, were deposited on the surface of TiO_2 NRs the photocathode (Pt/TiO_2 NRs/*p*-Si) showed turn on potential of 440 mV and short circuit current density

of 40 mA cm^{-2}. The photocathode were generate hydrogen for 52 h without noticeable degradation and with 2.5 % ideal cell regenerative cell efficiency.

Second, the limitation of *p*-type silicon photocathode for efficient PEC water splitting was managed by incorporation of a 3-dimenstional MoS_2 thin film with high density of catalytic edge-sites on a TiO_2 coated *p*-type silicon. The 3D MoS_2 HER catalyst were synthesized directly on TiO_2 coated 4-inch *p*-type silicon. Unlike the transferred MoS_2 to *p*-type silicon, the direct growth brings many advantages such as, 1. Can decrease the lengthy transfer time, 2. The directly grown MoS_2 catalysts can be immune from organic residue, 3. Better charge transfer between the $MoS_2/TiO_2/p$-Si interfaces and 4. Excellent adhesion of MoS_2 on TiO_2 coated *p*-type silicon. Therefore, the 3D $MoS_2/TiO_2/p$-Si photocathode were showed an onset potential of 0.35 V versus RHE at 1 mA cm^{-2} with a short circuit current density of 28 mA cm^{-2} and a saturation current density 37 mA cm^{-2}. The optical reflectance of the 3D $MoS_2/TiO_2/p$-Si is 14% (arithmetic mean) lower than that of a TiO_2/p-Si photocathode over the entire visible range. This antireflective 3D MoS_2 layer enhanced the charge generation efficiency which result in higher saturation current density than TiO_2/p-Si photocathode. Hydrogen generation in this photocathode lasts for more than 181 h without noticeable degradation.

The third main chapter describes the studies of TiO_2 NRs for solar water splitting. The drawback of TiO_2 photoanode, which is transparent for visible light/no visible light absorption and low carrier kinetics, for solar water splitting were improved by incorporation of dual atoms sulfur and nitrogen. The codoped TiO_2(S, N) NRs shows four times higher photocurrent density than

pristine, specifically 2.82 mA cm^{-2} at 1.23 V vs. RHE and 0.7 mA cm^{-2} for codoped and pristine TiO_2 NRs, respectively. The extracted photocurrent density from codoped TiO_2 (S, N) NRs is found be the highest among the co-catalyst free TiO_2 photoanodes reported up to date. Furthermore, the measured applied bias photon to-current conversion efficiency (ABPE) and incident photon-to-current conversion efficiency (IPCE) of the TiO_2 (S, N) photoanode found to be 1.46 % and 97 % at wavelength of 360 nm, respectively. The partial density of states calculation shows all dopant configuration can induces defect/dopant energy states between the conduction and valance band of TiO_2. The [N_O-S_O] configuration in the TiO_2 shows higher optical absorption coefficient followed by S_O and [S_{Ti}-N_O] configuration. Moreover, codoping of sulfur and nitrogen in the TiO_2 results higher optical absorption coefficient than individual doping. However, the dopant formation energy of [S_{Ti}-N_O] in the TiO_2 is lower than [N_O-S_O]. Therefore, the [S_{Ti}-N_O] configuration may exists more than the [S_O-N_O] configuration. The outperformance of the photoanode mainly resulted from the induced defect energy states between E_{CB} and E_{VB}. Codoping of sulfur and nitrogen in TiO_2 photoanode cannot impair the stability of the TiO_2, which is confirmed by measuring the chronoamperometry of TiO_2 (S, N) NRs for ~58 hours at 1.23 V vs. RHE.

Keywords: Photoelectrochemical water splitting, *p*-type silicon, titanium dioxide, molybdenum disulfide, solution processed

Student Number: 2014-31422

Dinsefa Mensur Andoshe

Table of Contents

List of Tables

List of Figures

Chapter 1

Photoelectrochemical Water Splitting: Principles and Photoelectrode Materials

1.1. Introduction

The biggest challenges of humanity facing this days are air pollution and climate change; which are mainly caused by the greenhouse gas emission. Even though by tireless work this day the molecule of the fuel is became smaller, decreasing the carbon content and reach in hydrogen molecule (wood→ Coal→Petroleum→Propane→Methane) we need very clean energy source/carriers to reduce the greenhouse gas and keeping the global temperature rise below 2 °C above the average global temperature of preindustrial time [1,2]. Among the alternative energy source/carriers; hydrogen molecule is getting considerable attention as an ideal future energy carrier due to, 1. Highest energy carrier per unit mass of any fuel, 2. It can be stored in gaseous, liquid and metal hydride form, 3. It can be transported over large distances, 4. It can be converted in to other form of energy, 5. It is environmentally compatible; combustion and/or using for fuel cells yield water as its waste byproduct, since its production do not produce pollutants and greenhouse gases.[3] However, hydrogen cannot be exist in nature as a gas rather exists combined with other elements but it can be produce from different materials integrated with energy sources and using appropriate production methods.

1.1.1. The Probable Paths to Hydrogen

Hydrogen can be produce by using a number of different process /method as shown in Figure 1, based on the energy source used to drive the reaction to produce hydrogen the production process can be classified as a carbon neutral and greenhouse gas emitter production methods. Currently, the dominant

hydrogen production method is a steam reforming, which uses fossil fuel and emits large amount of carbon dioxide. Some of carbon free hydrogen production methods are: (1) thermochemical water splitting which is mainly use nuclear energy,

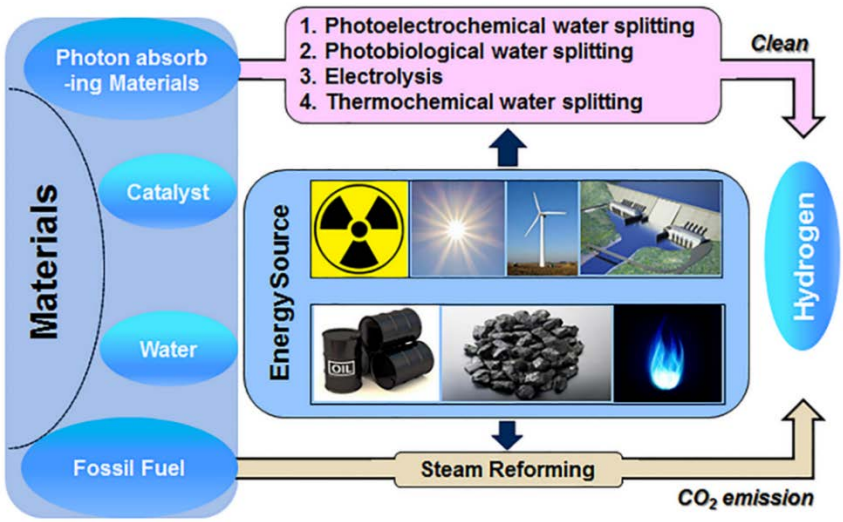

Figure 1.1. Some representative methods and energy source for hydrogen production.

(2) Electrolysis water splitting, that use electricity from hydropower, wind and solar energy, (3) Photobiological and photoelectrochemical water splitting which use solar energy to split water into its constituent atom, hydrogen and oxygen. Among these carbon free hydrogen production methods the photoelectrochemical water splitting is considered as one of the potential future eco-friendly rout that could enable the production of hydrogen using water as reactant and solar energy as primary energy source.

1.2. Solar water splitting

The required ideal Gibbs free energy to split water into its constituent molecule H_2 and $½O_2$ under standard condition is ΔG = 237.12 KJ/mole, which is corresponds to $\Delta E°$ = 1.23 eV per electron transfer according to Nernst equations[4]. The lower unoccupied molecular orbital (LUMO) level/reduction potential of water is aligned to 0.0 V and HOMO level/oxidation potential is aligned to 1.23 V relative to electrochemical energy scale at zero pH as shown in Figure 1.2.

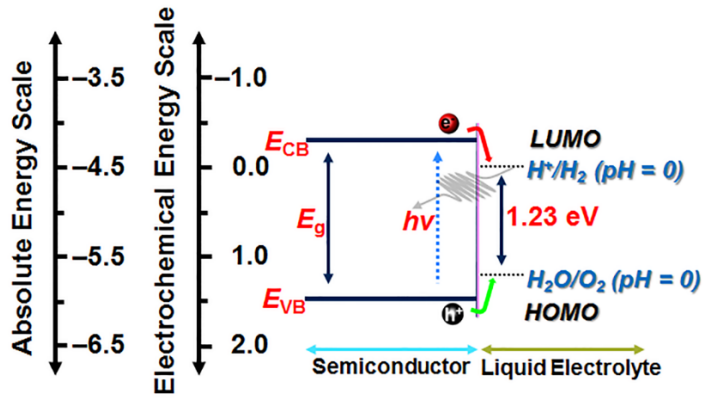

Figure 1.2. Schematics for Overall Solar Water Splitting under Zero pH Liquid Electrolyte. The semiconductor (photon absorbing materials)/electrolyte with their conduction band (E_{CB}) edge position/LUMO level and valance band (E_{VB}) edge position/HOMO level vs. absolute energy scale and electrochemical energy scale.

Integrating the solar radiation with solar capturing/absorbing material, which must have conduction band edge position /LUMO level more negative than water reduction potential and valance band edge/highest occupied molecular

orbitals (HOMO) level more positive than water oxidation potential vs. electrochemical energy scale is said to be solar water splitting. The absorbed photon result an e^-/h^+ pairs and the photogenerated electron reduce the proton/hydrogen ion while the hole oxidized the water as shown using red and green arrow in the Figure 1.2. The overall water splitting reaction is shown below.

$$H_2O \rightarrow H_2 + 1/2O_2 \text{ ----- (1.1)}$$

$$\Delta E° = E°_{cat} - E°ano = -1.23 \text{ eV}$$

The water splitting reactions in the acidic and basic electrolyte can be written as eq. (1.2-1.3) and (1.4-1.5), respectively[5].

$$4H^+ + 4e^- \rightarrow 2H_2, \qquad E°_{red} = 0.000 \text{ V vs. NHE ---- (1.2)}$$

$$2H_2O + 4h^+ \rightarrow 4H^+ + O_2, \quad E°_{ox} = 1.229 \text{ V vs. NHE ---- (1.3)}$$

$$4H_2O + 4e^- \rightarrow 2H_2 + 4OH^-, E°_{red} = -0.828 \text{ V vs. NHE ---- (1.4)}$$

$$4OH^- + 4h^+ \rightarrow 2H_2O + O_2, \quad E°_{ox} = 0.401 \text{ V vs. NHE ---- (1.5)}$$

These two reactions can be appear in the surface of two separated photon absorbing semiconductors. The semiconductors which used for the reduction reaction of water is a photocathode materials and oxidation reaction is a photoanode materials. The solar water splitting device contain working, counter and reference (optional) electrode which are connected with external circuit, one of the two electrodes either working or counter electrode comprised semiconductor is said to be photoelectrochemical (PEC) cell. PEC cell is a monolithic devices in which the electromagnetic energy is converted in to chemical energy, H_2 and O_2, at macroscopically different location, as shown in the Figure 1.3.

1.1.2. Basic Working Principle of PEC Water Splitting Cell

A PEC cell consists of semiconducting photoelectrodes, *n*-type and *p*-type semiconductor hereafter it will be known as photoanode and photocathode respectively. The photoelectrodes absorb a photons energy with higher than their bandgap energy, generating electrons and holes in the conduction and valence bands, respectively. The photoexcited electron-hole pairs must be separated and migrate to the water/electrode interfaces and to the back contact without/low carrier recombination. If the charge injections into the adsorbed species through the interfaces are thermodynamically favorable, then the electrons and holes have reduce and oxidize the adsorbed species (H^+ and OH^-), respectively.

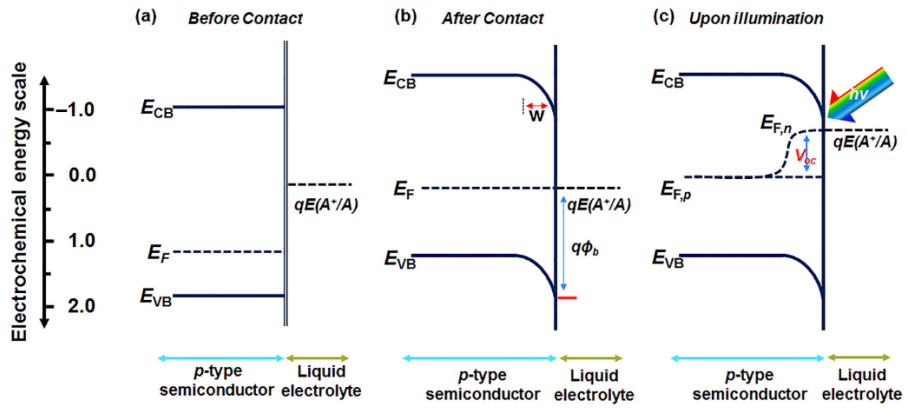

Figure 1.3. Schematic a p-type semiconductor liquid electrolyte interface (a) before contact (b) after contact the fermi level of a semiconductor align with the LUMO of the electrolyte. (c) Up on illumination E_{CB} is conduction band, E_{VB} is valance band, E_F is Fermi level, $qE(A^+/A)$ is LUMO level of the electrolyte, w is space charge region and $q_{\phi b}$ is barrier height, V_{oc} is

photovoltage, $E_{F,n}$ is a quasi-fermi level of minority charge carrier, $E_{F,p}$ is a quasi-fermi level of majority charge carrier.

When a photoelectrode is inserted in to an electrolyte (water), the charge carriers have transfer between the electrode and the electrolyte. The electrolyte donates (accepts) electrons to (from) the photoelectrode when the Fermi level of the electrode is more negative (positive) than the redox potential of the electrolyte. The density of charge carriers in a semiconductor is finite comparing to the density of state in the electrolyte and the potentials of the band positions at the interfaces in the given pH assumed to be pinned; therefore, the electron transfer between the photoelectrode and electrolyte result in a band bending due to the internal electric field that is built up. Consequently, the Fermi level is equilibrated with the redox potential of the electrolyte as shown in Figure 1.3. [4,6,7]

In the photoanode the photogenerated holes migrate to the semiconductor /electrolyte interface and oxidize the adsorbed reactant (OH^- or H_2O). At the same time, electrons are transferred to a counter electrode via back contact through an external circuit and reduce the adsorbed reactant (H^+) (Fig. 1.4(b)).

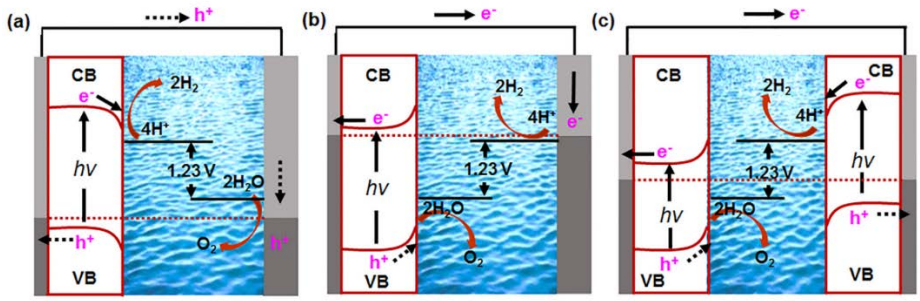

Figure 1.4. Schematics of photoelectrochemical water splitting (a) photocathode for hydrogen evolution reaction (b) photoanode for oxygen evolution reaction (c) photoanode and photocathode in tandem configuration.

Likewise, in the photocathode the photogenerated electrons move to the semiconductor /electrolyte interface and reduce the adsorbed hydrogen ion (H^+) while holes are transport to the counter electrode via back contact through an external circuit and oxidized the OH^- or H_2O. [6-9] The photoanode and photocathode can be connected in a tandem configuration (Z-scheme water splitting) as shown in Figure 1.4 (c). In a tandem configuration visible light can be utilize more efficiently than in the conventional water splitting systems.

Even though the theoretical thermodynamic free energy change to drive the water splitting reaction ($H_2O \rightarrow H_2 + 1/2O_2$) is ΔG = 237.12 kJ/mole and using Nernst equation, which is corresponds to $\Delta E°$ = –1.23 eV per electron transferred, practically the PEC water splitting process consume more potential than the theoretical estimated value due to the potential loss in the bulk of semiconductor electrode, in the interfaces between the semiconductors and the high Gibbs free energy of the photoelectrodes for hydrogen/oxygen adsorption. Therefore, the practical free energy needed for solar water splitting can be

written as $\Delta E = \Delta E° + \eta_{ovp}$, where $\Delta E°$ is the theoretical water splitting potential per electron transfer and η_{ovp}, is the overpotential that will lose during charge transfers, transport and adsorption/desorption process, which is mainly depend on the process and assembly, and the inherent nature of material. The potential drop (overpotential) during charge transfer between the photoelectrode semiconductor and electrolyte, which is due to the high Gibbs free energy of hydrogen/oxygen adsorption, can be decrease by applying a catalysts/co-catalysts on the surface of photoelectrode. The catalysts can decrease the adsorption free energy and facilitate the desorption of hydrogen/oxygen kinetics from the surface of the photoelectrode with minimum energy as shown in the figure 1.5.

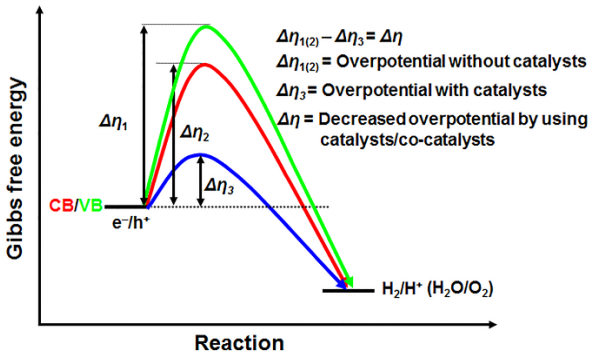

Figure 1.5. Schematic of free energy for charge transfer between the photoelectrode and electrolyte interfaces. CB is conduction band minimum for photocathode, VB is valance band maximum for photoanode. The green curve is for OER, the red curve is for is for HER and the blue curve is for OER/HER after catalyst/co-catalysts incorporated. Usually the OER show a higher overpotential than HER.

1.3. Efficiency for photoelectrochemical cell

Efficiency of the PEC cell can be defined as solar to hydrogen conversion efficiency (η_{STH}), which is the ratio of the amount of hydrogen output from the PEC cell to input light energy. The STH can be obtained using equation 1.1.

$$\eta_{STH} = \left[\frac{(H_2 mmol/s) \times (\triangle G)}{(P\ in\ (mW cm^{-2})) \times A\ (cm^{-2})}\right] \text{-------(1.1)}$$

where, H_2 mmol/s is the amount of hydrogen molecule produced using only solar power, which is measured by mass spectroscopy or gas chromatography analytical instruments, $\triangle G$ = 237. 2 kJ/mol is the change in Gibbs free energy of water splitting, P_{in} is normalized input/incident solar power to the PEC photoelectrode; in the laboratory the illumination source must be equivalent to 1 sun value AM 1.5 global spectrum, A (cm^{-2}) the area of the PEC electrode exposed to the electrolyte and the solar irradiation. It can be calculated the STH using the following alternative equation (1.2) since the PEC cell produce only hydrogen and oxygen without adding any sacrificial agent (electron donor or/and acceptor) to the electrolyte. Moreover, the working electrode (WE) and counter electrode (CE) must be immersed in the same pH electrolyte.

$$\eta_{STH} = \left[\frac{\left|J_{Sc} mA\ cm^{-2}\right| \times (\Delta E°) \times \varepsilon_{fe}}{P_{in}\ (mW cm^{-2})}\right] \text{-------(1.2)}$$

where J_{sc} is short circuit current density, which correspond to the rate of molar hydrogen generation. $\Delta E°$ = 1.23 V is the theoretical standard water splitting potential, ε_{fe} is the faradic efficiency of fuel production (H_2 and O_2).

Even though, measurement of the overall efficiency (η_{STH}) of the PEC cell is an important benchmarking parameter, there are other kind of efficiencies that use

to diagnose a specific properties of PEC photoelectrode materials and screening purpose. For example, if the current density/amount of fuel from the PEC cell is a function of both solar energy and applied bias voltage then the measured quantity does not reflect the true solar to hydrogen conversion efficiency of the PEC cell due to the applied bias which can enhance and exaggerate the performance of the device. In this case, the measured quantity is ratio of the net chemical output power with the incident solar power and which can be acquired by modifying equation (1.2), i.e., subtracting the applied bias from the theoretical standard water splitting potential $\Delta E°$. The calculated quantity after modification is known as Applied bias photon to current conversion efficiency (ABPE) (see eq. 1.3), which usually used for PEC photoelectrode materials screening. The linear sweep voltammogram (LSV) measurement of the PEC must be performed using two electrode configuration, WE and CE. The two electrode should have in the same pH electrolyte and without adding sacrificial donor and/or acceptor.

$$\text{ABPE} = \left[\frac{\left|J_{mpp}\ mA\ cm^{-2}\right| \times \left(|\Delta E°| - |V_{mpp}|\right) \times \varepsilon_{fe}}{P_{in}\ (mW cm^{-2})}\right] \text{------- (1.3)}$$

Where J_{mpp} is the photocurrent density at maximum power point, $\Delta E° = 1.23$ V is the theoretical standard water splitting potential, V_{mpp} is the applied bias potential at the maximum power point, ε_{fe} is the faradic efficiency, P_{in} is the input power. Unlike ABPE that must be measured in two electrode configuration (WE and CE), the ideal regenerative cell efficiency (IRCE) can measured using three electrode configuration (WE, CE and reference electrode

(RE)).[10] The IRCE is described by using equation (1.4) which is analogues to the efficiency of photovoltaic cell.

$$\eta_{IRCE} = \frac{V_{mpp}\,(V) \times J_{mpp}\,(mA\,cm^{-2})}{P_{in}(mWcm^{-2})} \times 100\% \text{-------(1.4)}$$

where V_{mpp} is measured potential at the maximum power point, J_{mpp} is the current density obtained from the LSV measurement at maximum power point.

The three fundamental process of the photoelectrode involved during PEC water splitting, which are the charge generation (e^-/h^+), the photogenerated carrier transport and the charge transfer in the interfaces give the incident photon to current conversion efficiency (IPCE) of the device. The IPEC is defined as a measure of the ratio of the photocurrent with the rate of incident photons as a function of wavelength.

$$IPCE = \frac{hc}{e}\left(\frac{J_{pho}(\lambda)}{\lambda P(\lambda)}\right) = \eta_{e^-/h^+}\,\eta_{transport}\,\eta_{transfer} \text{ ------- (1.5)}$$

Where, η_{e^-/h^+} is charge generation efficiency, $\eta_{transport}$ is charge transport efficiency and $\eta_{transfer}$ is charge transfer efficiency at the interfaces.[11]

1.4. Semiconductors for PEC electrode application

In addition to the band edges are straddle the oxidation and reduction potential of H_2O, a semiconductor should absorb the largest portion of the solar radiation to design efficient PEC water splitting device. Figure 1.6 shows a solar radiation (SR) contains electromagnetic wavelengths divided in to three bands, ultraviolet, visible and a portion of infrared wavelength. The ultraviolet radiation covers a range of 315 nm-400 nm wavelength, which is about 8 % of

the SR. Likewise the visible wavelength (400 nm-700 nm) covers ~47 % of the SR and the near-infrared (NIR) wavelength covers about 45 % portion from the SR. Even though theoretically the solar water splitting process can be drive using a solar radiation bellow 1000 nm wavelength (NIR), considering the ideal water splitting potential is 1.23 eV due to the electrochemical overpotential usually the NIR radiation will dissipate. Therefore, the target single semiconductor PEC electrode should absorb the visible region of the SR.

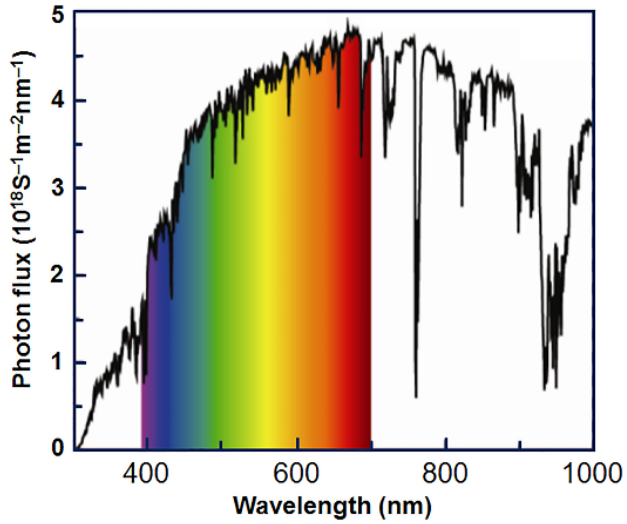

Figure 1.6. The Solar radiation spectrum at 1.5AM a wavelength from 300 nm to 1000 nm the maximum wavelength that drive theoretically the solar water splitting reaction.

Others basic requirements of a semiconductor to design efficient PEC device is chemical/ photochemical stability in the liquid electrolyte and fast carrier transport to overcome the charge recombination. Furthermore, the semiconductor should have a catalytic properties to facilitate the adsorption and desorption of the reactant with the smallest Gibbs free energy change, and

should be abundant, environmental friendly and low cost. However, these basic requirements appear to be in conflict and certain tradeoff have to be made. In some cases, these tradeoffs can be avoided by adopting suitable morphology and materials combination.

1.5. Scope and objective of the thesis

This thesis focuses on the development of efficient silicon based photocathode by avoiding the tradeoffs of silicon by adopting smart architectures and materials combination. More specifically, the synthesis of passivation, antireflective and catalytic layers on a *p*-type silicon photocathode using earth abundant materials for PEC application. Moreover, it also present about a foreign atoms incorporated TiO_2 photoanode for oxygen evolution reaction with detail of electrical, optical and photoelectrochemical analysis to verify the influence of codopant in the PEC performance of titanium dioxide.

1.6. Reference

1 Gupta, R. B. *Hydrogen fuel: production, transport, and storage*. (Crc Press, 2008).

2 McGlade, C. & Ekins, P. The geographical distribution of fossil fuels unused when limiting global warming to 2 ° C. *Nature* **517**, 187-190 (2015).

3 Grimes, C. A., Varghese, O. K. & Ranjan, S. *Hydrogen generation by water splitting*. (Springer, 2008).

4 Walter, M. G. *et al.* Solar water splitting cells. *Chemical reviews* **110**, 6446-6473 (2010).

5 Van de Krol, R. & Grätzel, M. *Photoelectrochemical hydrogen production*. Vol. 90 (Springer, 2012).

6 Hisatomi, T., Kubota, J. & Domen, K. Recent advances in semiconductors for photocatalytic and photoelectrochemical water splitting. *Chemical Society Reviews* **43**, 7520-7535 (2014).

7 Kudo, A. & Miseki, Y. Heterogeneous photocatalyst materials for water splitting. *Chemical Society Reviews* **38**, 253-278 (2009).

8 Batzill, M. Fundamental aspects of surface engineering of transition metal oxide photocatalysts. *Energy & Environmental Science* **4**, 3275-3286 (2011).

9 Osterloh, F. E. Inorganic materials as catalysts for photochemical splitting of water. *Chemistry of Materials* **20**, 35-54 (2007).

10 Coridan, R. H. *et al.* Methods for comparing the performance of energy-conversion systems for use in solar fuels and solar electricity generation. *Energy & Environmental Science* **8**, 2886-2901 (2015).

11 Chen, Z., Dinh, H. N. & Miller, E. Photoelectrochemical water splitting. *SpringerBriefs in Energy, New York*, 49-61 (2013).

Chapter 2

A *p*-type silicon photocathode for water reduction with a solution processed titanium dioxide nanorods protection and antireflection layer

2.1. Introduction

The search for an alternative and inexpensive source of green energy is vital to reduce rate of increase of global temperature caused by greenhouse gas emissions and to reduce usage of the limited fossil fuels reserve.[2,12] Water and solar energy are inexhaustible and can get them almost all over the globe. Integrating these abundant natural resources with efficient photoactive materials for hydrogen production is among the best options to satisfy global energy demand and mitigate the global warming caused by fossil fuel burning.[13-15] Among the various photoelectrodes researched for SWS to date[14,16-20], silicon is one of the most widely studied materials since it has a suitable optical band gap (1.12 eV) to absorb the widest part of the solar spectrum (visible light), as shown in Figure 2.1a, and generates a sufficient amount of energy for water splitting ($2H_2O + h\nu \rightarrow 2H_2 + O_2$). However, silicon photoelectrodes suffer photocorrosion in liquid electrolyte due to the position of its thermodynamic redox potentials, which are in the close proximity to the redox potential of water $(H^+/H_2)/(O_2/H_2O)$.[21] Photoelectrochemical, electrochemical and chemical routes corrodes a silicon electrode. The first two routs require net charge transfer between the photoelectrode and electrolyte, whereas the chemical corrosion involves reaction that causes degradation/dissolution of the electrode materials without necessity of net charge transfer between the electrode and the electrolyte solution.[22] The corrosion causes surface defects that

enhance the recombination rate and facilitate the formation of insulator, i.e.

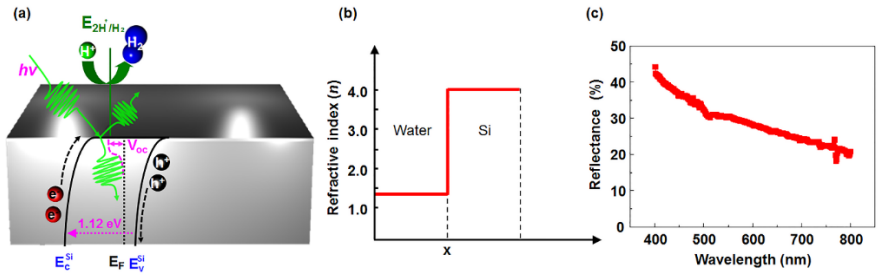

Figure 2.1. (a) Schematics of oblique view p-type Si photocathode during hydrogen production (b) possible assumption of light attenuation in the electrolyte (water) and silicon interface. (c) Optical reflectance of Silicon.

Oxide layer, at the surface. A thick oxide layer can hinder the transfer of minority carriers from silicon to electrolyte solution and/or from the electrolyte to silicon.[22] Moreover, planar silicon has a more than 4.0 refractive index as shown in **Figure 2.1**, in the entire solar radiation about 37% (arithmetic mean) of the incident light on the surface of silicon is reflected.[23-25] The severe photocorrosion, high reflectance and high overpotential of silicon jeopardizes the solar to hydrogen conversion (STH) efficiency and hinders the prolonged operation of the electrode.[26]

Recently, researches in the silicon photoelectrode not only focused on synthesizing a surface passivation layer that can protect the chemical and/or photo-induced corrosion without degrading the inherent photoactive ability of silicon but also developing low cost efficient catalysts to reduce the high over potential of silicon photoelectrode.[15,24,27-31] A significant improvement in the

reduction of overpotential and stability of silicon photocathode was reported using an epitaxially grown strontium titanate ($SrTiO_3$) protective layer with Pt/Ti thin film catalysts.[27] Likewise, a thermally grown SiO_2 interfacial tunnelling layer between Pt/Ti thin film and *p*-type silicon shows better onset potential for reducing water but low photocurrent density.[28] TiO_2 thin films have been widely studying to passivate a silicon photoelectrode.[22] For example, Seger et al. [30], reported 72 h stability with a 520 mV onset potential for a silicon photocathode using conductive TiO_2 thin film and 1M $HClO_4$ electrolyte. Furthermore, a TiO_2 thin film can improve the performance of *p*-InP photocathode due to the large valance band offset between the photoactive material and the passivation layer.[32 33-36] Although many materials have been studied as a passivation layer and catalysts for silicon photoelectrodes, the reported STH efficiencies have not yet economically viable. [15,37-39] The possible reason could be (1) the high reflectance of a planar silicon photoelectrode was not seriously considered. (2) The stability issue of the silicon photoelectrode in the liquid electrolyte for the long operation time is not solved. (3) The usage of the noble metal thin film catalysts increase the cost of H_2 production. Therefore, considering abundant, eco-friendly/non-toxicity, catalysts properties and easy synthesis of different nanostructure, TiO_2 nanorods (NRs) are employed on the surface of *p*-type silicon to address the aforementioned silicon photoelectrode problems for photoelectrochemical water splitting.

2.2. Effects of TiO_2 nanorods on *p*-Si

TiO_2 is an *n*-type wide bandgap semiconductor with a bandgap energy of 3.0 -3.2 eV. When an *n*-type TiO_2 films is deposited/grown on a *p*-Si substrate, an *n*-TiO_2/*p*-Si heterojunction is formed. Since the electron affinity of *p*-Si ($X_{si} \approx$ 4.0 eV)[40] is smaller than that of TiO_2 ($X_{TiO2} \approx$ 4.3 - 4.5 eV)[41,42] and the work function of *p*-Si ($\Phi_{p\text{-}Si} \approx$ 4.9 eV) is slightly higher than that of TiO_2 ($\Phi_{TiO2} \approx$ 4.6 - 4.8 eV)[43-49], the offset between the conduction band minimums and the downward band banding is facilitate the transport of photogenerated minority carriers (electrons) from *p*-Si through TiO_2 to the location where hydrogen ions are reduced. Simultaneously the majority (holes) carriers travel to the back contact of the photocathode as shown in **Figure 2.2a**. The TiO_2 films exhibit a high transmittance of visible light, therefore, most of the illuminated sunlight can reach to the surface of silicon photoelectrode. Moreover, the TiO_2 films have refractive index of $n_{TiO2} \sim 2.64$ at 550 nm, [50] which can suppresses the Fresnel reflection at the electrolyte/*p*-Si ($n_{Si} \sim 4.09$ at 550 nm)[51] interface over a broad range of wavelengths. [52,21]

Use of TiO_2 NRs rather than a planar TiO_2 layer on *p*-Si have several advantages. TiO_2 NRs, which have a much larger surface area than the planar layer, have an increased number of reaction sites for HER. TiO_2 NRs can further reduce light reflection at the electrolyte/*p*-Si interface compared with a planar TiO_2. If the areal density of TiO_2 NRs changes gradually (denser at the bottom than at the top), the incident light is propagated into the *p*-Si substrate with negligible reflection at both electrolyte/TiO_2 NRs and TiO_2 NRs/*p*-Si interfaces, as shown **in Figure 2.2a**. When the areal density near the top surface of NRs

approaches zero, then the refractive index of the top surface is expected to become identical to that of the electrolyte, leading to perfect antireflection at the interface, as shown in Figure 2.2b.

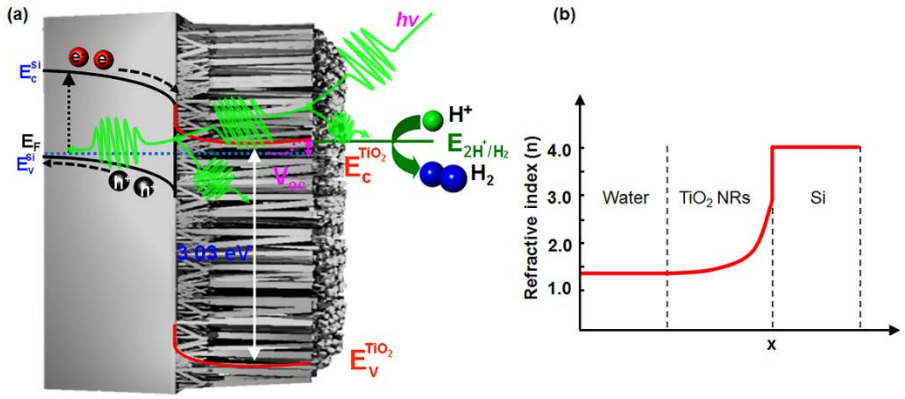

Figure 2.2. (a) Schematics of oblique view p-type Si/TiO2 NRs photocathode during hydrogen production (b) The light attenuation in the electrolyte (water)/TiO2NRs/p-Si photocathode.

2.3. Wafer-Scale Synthesis of TiO_2 NRs on *p*-type silicon

To achieve the desired density gradient in TiO_2 NRs on the surface of silicon and considering the cost effectiveness and facileness a hydrothermal synthesis method was employed. First, a *p*-Si (100) wafer was cleaned with acetone and isopropanol alcohol, in conjunction with ultrasonication and soaked for 1 min in 2% HF to remove residual organic solvent from the surface. Then, a 5-nm-thick seed layer of TiO_2 film (nominal thickness 20Å) was deposited using an electron-beam evaporator (KVE-E2004L) and annealed for 5 min under high vacuum using a rapid thermal analyser. TiO_2 NRs were grown on the pre-deposited 5 nm TiO_2 seed layer by hydrothermal synthesis using a large

autoclave with precursors tetrabutyl titanate, DI−water, and HCl solutions with volume ratios of 1.6, 49.2, and 49.2%, respectively. The precursors were added to glass beaker and stir vigorously using magnetic stirrer until the cloudy colour changed to watery. Then the solution was transferred to the Teflon beaker in which the silicon substrate was placed at the bottom keeping the active face up. The Teflon beaker which had the precursor solution and the TiO_2 coated silicon substrate was inserted in the autoclave and sealed carefully. The Growth was carried out for 30 to 120 min and 180-220°C in the oven. Subsequently, Pt nanoparticles (diameter 1-2.5 nm) were deposited on the surface of hydrothermally grown TiO_2 NRs using an electron-beam evaporator.

2.4. Characterization

2.4.1. Physical characterization

The XRD data were acquired using a Bruker Miller Co., D8-Advance diffractometer with Cu Kα radiation (λ = 1.5406 Å) operating at 40 kV and 40 mA at a scanning rate of 0.06° sec^{-1}. Specimens for XRD measurements were taken for both as-grown TiO_2 nanorods and annealed at 500°C. The morphology of the synthesized sample were observed by a field emission scanning electron microscope (ZEISS, MERLIN Compact) and transmission electron microscope (JEOL JEM 2100F). X-ray photoelectron spectroscopy measurements were carried out using a Kratos AXIS-His and a monochromated Al-Kα (*hv* = 1486.58 eV) X-ray source to determine the composition of the synthesized sample. The high-resolution spectra of the Ti2*p*, O1s, and C1s and Pt4f core level were identified using a pass energy of 100eV through a 0.4 mm

analyser slit width. Each high-resolution scan was measured four times and summed, using 50 meV steps with a dwell time of 157 ms per step. Film composition was estimated using CasaXPS (ver. 2.3.16) peak fitting, in which the integrated intensities were divided by the Wagner relative-sensitivity factors after a Shirley background subtraction. Angle-dependent reflectance measurement of the sample was carried out using a homemade system equipped with an automatic rotating sample stage and a photodetector. The incident light was generated from a Xe arc lamp source with a monochromator (Mmac-200).

2.4.2. Photoelectrochemical characterization

The PEC properties of the synthesized photocathode were measurement using a three-electrode configuration consisting of the prepared working electrode, calomel reference electrode, and a Pt wire /Graphite rod as a counter electrode with a 0.5 M H_2SO_4 electrolyte solution. All potentials were applied versus the calomel reference electrode and converted into the reversible hydrogen electrode (RHE) based on the Nernst equation:

$$V_{RHE} = V_{calomel} + E_{calomel} + 0.059 * pH \text{ ----- (2.1)}$$

Where V_{RHE} and $V_{calomel}$ are the applied potentials against RHE and calomel reference electrode, respectively. $E_{calomel}$ = 0.24 vs. the standard hydrogen electrode. A Xe arc lamp was used as a light source and calibrated to 1 sun (100 mW cm^{-2}) at the sample location using a standard Si photodiode. In each PEC measurement of the photocurrent, the sample was cathodically polarized at a scan rate of 10 mV s^{-1} under illumination or in the dark. The photocurrent was recorded using a computer-controlled multichannel electrochemical analyser

Potentiostat (IVIUMnSTAT), which was simultaneously used to control the applied potential. The chronoamperometry measurements were performed using applied potential of 0.0 V vs. RHE. The IPCE measurements were carried out using a computer-controlled monochromator (MonoRa150) and an amplifier for photocurrent detection. Electrochemical impedance spectroscopy (EIS) of the photocathode were recorded using the same potentiostat in the preceding three-electrode configuration and presented as Nyquist plot. A sinusoidal voltage perturbation with an amplitude of 10 mV and frequencies ranging from 350 KHz to 1 Hz was superimposed on the bias voltage to gather the EIS data under illumination. The EIS data were fit to the equivalent circuits, as discussed in the text, using the Z plot 2.x software.

2.5. Result and discussion

2.5.1. Physical and optical properties of the synthesized TiO_2 nanorods on *p*-Si

TiO_2 NRs were successfully grown uniformly in the entire 4-inch Si wafers. The TiO_2 NRs were grown uniformly over the entire wafer. The *p*-Si wafers with TiO_2 NRs became dark blue–black in colour due to highly enhanced diffuse scattering, for comparison the optical image of both e-beam coated (5 nm) TiO_2 film/*p*-Si and hydrothermal grown TiO_2 NRs/*p*-Si samples are shown in the Figure 2.3.

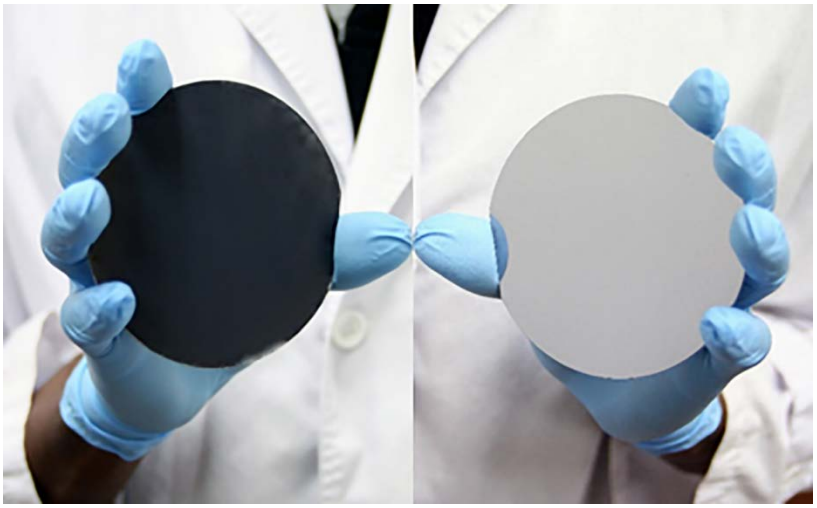

Figure 2.3. Optical image of hydrothermal grown TiO_2 NRs on the 4-inch silicon wafer (left) and e-beam deposited TiO_2 film on the 4-inch silicon wafer (right).

The TiO_2 NRs with different morphologies on *p*-Si substrates were grown using a solution-processed hydrothermal method. The TiO_2 NRs are tilts from the surface in the normal direction of the substrate. Fixing the concentration of the precursor, the length and diameter of the NRs were highly dependent on the synthesis time, temperature and cooling condition of the autoclave. When the temperature was fixed at 180°C, the synthesis time vary from 30 to 120 min and the autoclave cooled naturally to the 100 °C and subsequently to room temperature by dousing with water, the heights of the synthesized NRs were, For example, the heights of the TiO_2 NRs grown at the temperature of 180 °C for 30 min were about 100 nm see **Figure 2.4** a and b, likewise employing the same growth temperature for 1 and 2 h , the heights of the TiO_2 NRs were 1 and 2 µm, respectively as shown in the **Figure 2.4 e-h**. Furthermore, a 350 nm

TiO_2 NRs were obtained by the growth temperature of 180 °C for 1 h and the autoclave was removed from the oven when the growth time (1h) was completed and cooled to room temperature by dousing water see **Figure 2.4 c-d**.

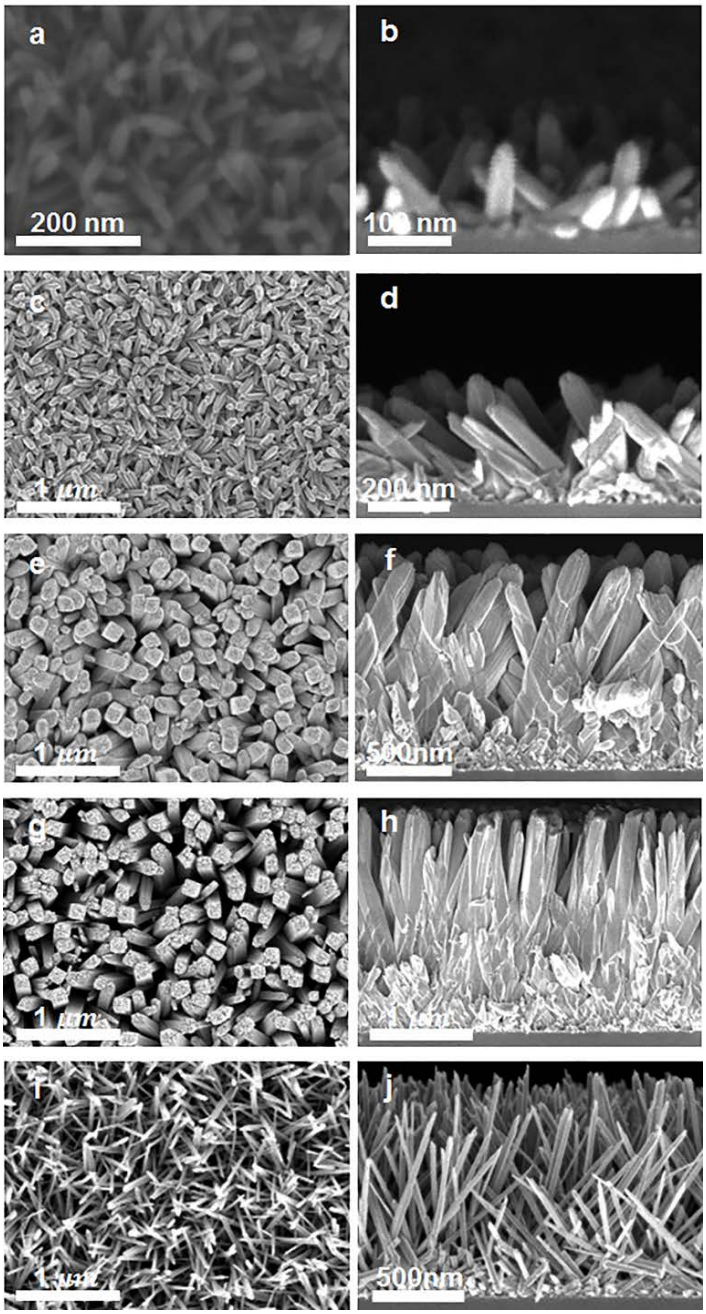

Figure 2.4. FSEM images of hydrothermally grown TiO_2 NRs on *p*-Si substrate. (a)-(b), ~100 nm high, (c)-(d), ~ 350 nm high, (e)-(f), (i)-(j), ~ 1 μm high g-h, ~ 2 μm high and their diameters is ~ 120 nm- 160 nm for sample (a-h) and ~ 32 nm for i,j samp

When the growth temperature was changed to 220 °C for 2 h keeping other condition fixed as Figure 2.4 g and h, the height and diameter of the resulting TiO_2 NRs were 1 μm and ~32 nm, respectively. Therefore, fixing the concentrations of the precursors at the high synthesis temperature for long reaction time in the oven result in a thinner and longer TiO_2 NRs. A 5 nm TiO_2 seed layer were coated on *p*-Si substrate which is high enough for nucleation and growth of TiO_2 NRs on the surface, and thus the areal density of TiO_2 NRs is high. As the synthesis time increases, the concentrations of the precursors decrease, since little amount of the precursor was used to nucleate and formation of TiO_2 NRs on the surface of silicon. For sufficient growth time, the density of TiO_2 NRs could decrease from the bottom to the top. Furthermore, the fully grown TiO_2 NRs could dissolute gradually for extended growth time at the higher temperatures in the acidic solution, which also results the change in areal density from the bottom to the top. Therefore, the areal density of NRs becomes smaller with increasing the length of NRs, leading to density gradients in the TiO_2 NRs. Bothe the high-resolution transmission electron microscopy and x-ray diffraction measurements were revealed the synthesized TiO_2 NRs on the *p*-Si substrate were polycrystalline rutile phase.

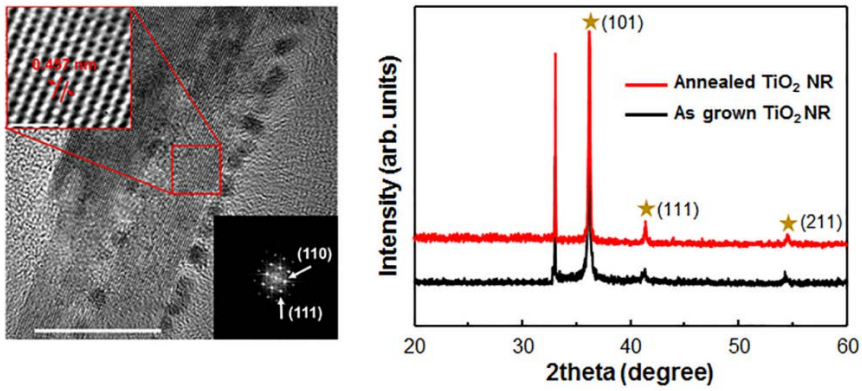

Figure 2.5. HRTEM image and XRD spectra of hydrothermal grown TiO_2 NRs/p-Si substrate

Significant change was not observed on the measured XRD peaks for annealed at the temperature of 500 °C and as synthesized TiO_2 NRs/*p*-Si except negligible peak intensity difference. The e-beam decorated Pt nanoparticles (nominal thickness 3Å) on the surface of hydrothermal grown TiO_2 NRs/*p*-Si could not be visible by SEM due to the size of the nanoparticles, However, using TEM coupled with energy dispersive spectroscopy (EDS) were observed and revealed the diameter of the Pt nanoparticles were ~2.5 nm and coated uniformly on the surface the TiO_2 NRs. Likewise, the X-ray photoelectron spectroscopy (XPS) measurement indicate the existence of –OH and $–H_2O$ bonds on the TiO_2 surface, which may facilitate adsorption of H^+ ions for HER,[44, 45] see Figure 2.6. [53,54 43,44]

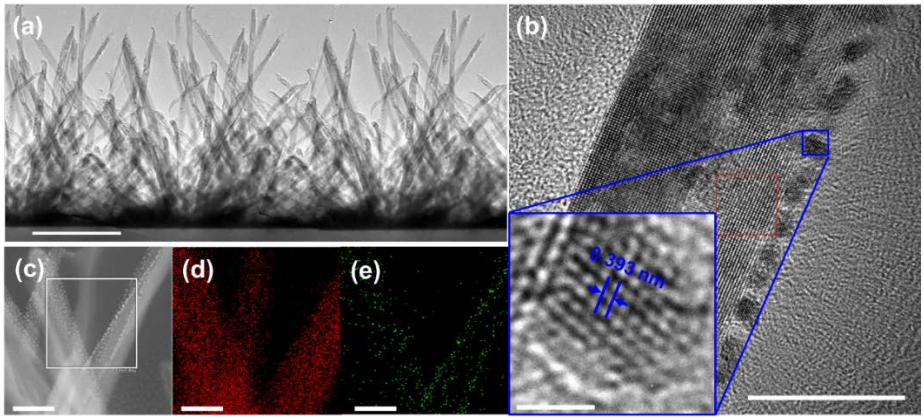

Figure 2.6. (a) Low magnification TEM image of TiO2 NR/p-Si (b), high magnification of single TiO2 nanorod and the decorated Pt particle (blue square) (c)-(e) EDS image with Ti and Pt distribution on the rod respectively. Scale bars, (a) 500 nm (b) 20 nm (c)-(d) 25 nm and in the blue square 2 nm.

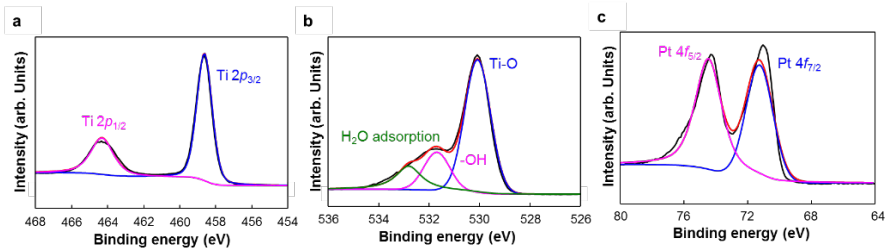

Figure 2.7. (a)-(c) High resolution X-ray photoelectron spectra of Pt decorated hydrothermally grown TiO2 NRs/p-Si sample.

The optical reflectance of the synthesized samples in the range of 400-1200 nm wavelength are shown in the **Figure 2.8**. The bare *p*-Si and TiO_2 seed layer (5 nm)/*p*-Si samples have the optical reflectance of 37.5% and 34.4% (arithmetic mean), respectively, which was measured with incident angle of 40^o and 550 nm wavelength. In contrast, the light reflectance of the TiO_2 NRs/*p*-Si sample was very low. The highlighted Figures 2.8 d and e show the dramatic reduction

of reflectance in the TiO_2 NRs/*p*-Si sample compared with *p*-Si and TiO_2 seed layer/*p*-Si samples. For example, the reflectance of the TiO_2 NRs/*p*-Si sample was 1.4% for an incident angle of 40° at a wavelength of 550 nm. Such a dramatic reduction of optical reflectance in the TiO_2 NRs/*p*-Si sample would enhance the photogenerated carrier efficiency of the photoelectrode.

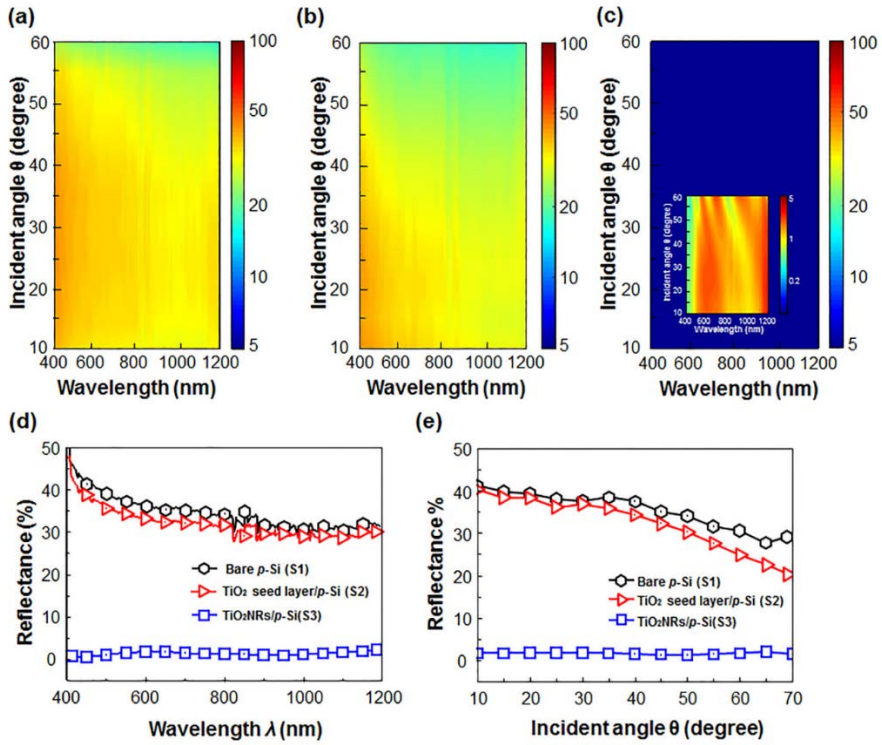

Figure 2.8. Angle dependent reflectance. (a) Reflectance of bare silicon (b) Reflectance of e-beam deposited 5nm thick TiO_2 film/*p*-Si, (c) Reflectance of hydrothermally grown TiO_2 NRs /*p*-Si and inset with 5% reflectance scale (d) Reflectance vs wavelength at 40° incident angle (e) Reflectance vs incident angle at 500 nm irradiation.

2.5.2. Photoelectrochemical properties

Figure 2.9. Show the linear sweep voltammetry (LSV) curves of bare *p*-Si (S1), TiO_2 seed layer (5 nm)/*p*-Si (S2), as grown and annealed TiO_2 NRs/*p*-Si (S3) photocathode. The LSVs were measured using a single compartment glass cell with a three electrode set-up and 0.5 M H_2SO_4 electrolyte without any sacrificial reagent and stirrer. The average exposed area of the photocathodes to the light illumination and electrolyte solution were about 0.5 cm^2. The S1 sample showed an onset potential of about -0.75 V [the voltages provided are relative to RHE, unless noted otherwise] and the saturated current density was ~32 mA/cm^2, which is similar to previous reports.[55-57] After the 5-nm-thick TiO_2 film was deposited over *p*-Si using an electron-beam evaporator, the onset potential is anodically shifted by 0.25 V and the saturated current density is increased by ~1 mA/cm^2. The improvement is attributed to the catalytic properties of the TiO_2 layer and the slight reduction in the light reflectance. The S3 photocathode was shown an anodic shift of ~0.75 V and the increment of the saturated current density by ~8 mA/cm^2 compared to the S1 sample. However, when the S3 sample was annealed at 500°C for 1 h under ambient air, the PEC performance decreased markedly (Figure S4). The annealed TiO_2 NRs/*p*-Si sample exhibited a hump in the middle of the LSV curve, which is a result of the high series resistance of the TiO_2 layer. The hydrothermally grown TiO_2 NRs, which are probably nonstoichiometric and defective[58,59] allow the transfer of carriers though the oxide layer with a small potential drop. This finding corroborates previous reports that as-grown TiO_2 films exhibited better water splitting ability than annealed TiO_2 films.[29,30]

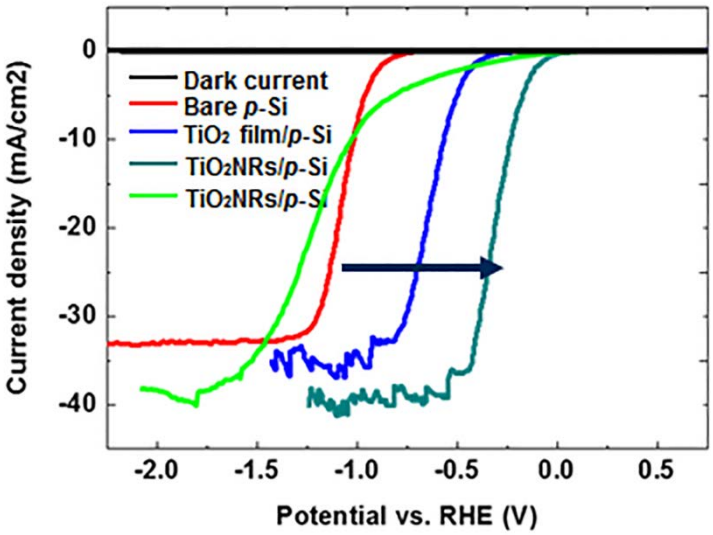

Figure 2.9. The LSV curves of bare *p*-Si (S1), TiO_2 seed layer (5 nm)/*p*-Si (S2), as grown TiO_2 NRs/*p*-Si (S3) and annealed TiO_2 NRs/*p*-Si photocathode. The arrow indicated the onset potential shift.

Photocathode	Onset potential vs. RHE (V)	Saturation current density (mA/cm^2)
Bare *p*-Si	–0.75	32
TiO_2 film/*p*-Si	–0.50	33
TiO_2 NRs/*p*-Si	0.0	40

Table 2-1. Summary of saturation current density and turn on potential

The short circuit photocurrent density of TiO_2NRs/*p*-Si photocathode is 40 mA/cm^2, which is the highest photocurrent ever reported for photocathodes based on planar *p*-Si for solar water splitting.[27,30,57] However, at -0.4 V the current density is about 45 mA/cm^2 which is slightly higher than the theoretical limit current density of crystalline silicon, i.e., 44 mA/cm^2.[60] The large increase in photocurrent is attributed to the antireflective properties of the density-

graded uniform TiO_2 NRs layer. Moreover, the antireflective layer, TiO_2 NRs, could absorbs a UV light better than silicon and thus probably contribute to the total current density of the photocathode.

The LSV curve of the photocathodes after Pt were decorated, Pt/*p*-Si (S4), Pt/TiO_2 seed layer (5 nm)/*p*-Si (S5) and Pt/TiO_2 NRs/*p*-Si (S6) Shown in Figure 2.10. The decoration of Pt nanoparticles significantly improved the onset potentials of the three samples as. The saturated current densities of S4, S5 and S6 samples were ~33 mA/cm^2, 32 mA/cm^2 and 40 mA/cm^2 at 0 V vs. a reference hydrogen electrode (RHE), respectively. The variation of current density in the negative potential regions of each electrode originates from the hydrogen bubbling on the surface of photocathodes. The saturated photocurrent density was not affected by Pt decoration because the amount of deposited Pt nanoparticles was very small; the nominal thickness of Pt deposited by electron-beam deposition was 0.3 nm.

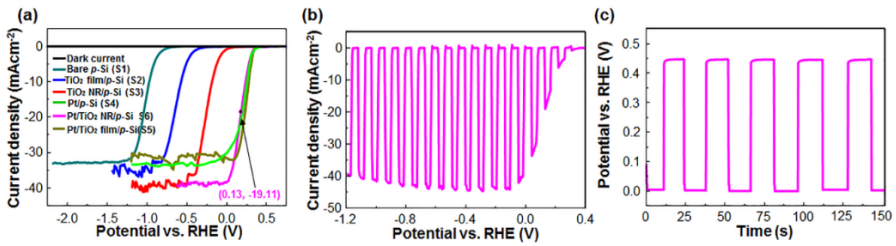

Figure 2.10. (a) LSV curves of the photocathodes, the dark blue arrow shows the onset potential shift due to the catalytic properties of TiO_2 and the red arrow shows onset potential shift due Pt decoration (b) Chronoamperometry of Pt/TiO2/p-Si photocathode measurement with chopped light at 0.0 V vs. RHE

The dark current is 0.0 mA/cm^2 even at -1.2 V vs. RHE and the photocurrent density is higher than 40 mA/cm^2 above 0.0 V vs. RHE shown in the Figure 2.10 b. The slight decrease in the photocurrent toward highly negative potentials is due to the crowded hydrogen bubbling at the surface of TiO_2 NRs. Boettcher et al,[57] reported a Si-based photocathodes with the photocurrent saturation within ~100 mV vs RHE, however, the photocathode (S6) didn't reach the saturation photocurrent within ~100 mV probably due to the density of Pt nanoparticle particle on the surface of TiO_2 NRs. With the chopped light, we could measure the open circuit voltage of the photocathode. The open circuit voltage was ~440 mV, which is similar to the potential difference (~0.45 eV) between the Fermi level and the middle of the band energy of *p*-Si Figure 2.10c.

The LSV curves were converted to Tafel plots, the potentials were plotted as functions of the logarithm of current density (Figure S5). The linear portions of the curves were collected to determine the Tafel slopes. With the TiO_2 NRs, the Tafel slope decreased from 178 mV/dec to 123 mV/dec. Water reduction for the evolution of hydrogen occurs by the accepted three-step mechanism, such as, the Volmer (Tafel slope of 120 mV/dec in an acidic electrolyte), Heyrovsky (40 mV/dec), and Tafel (30 mV/dec) steps.[61-63] The Tafel slope of 123 mV/dec for the TiO_2 NRs/*p*-Si sample indicates the HER occurred by the Volmer reaction with this cathode structure. After the Pt decoration, the Tafel slope for the S6 sample was evaluated be 49 mV/dec, which indicates that the Pt nanoparticles promote the HER on the surface of TiO_2 NRs by the Heyrovsky reaction mechanism.[61-63]

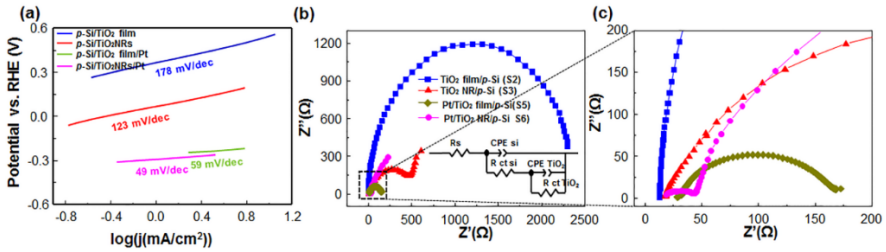

Figure 2.11. (a) Tafel slopes of TiO_2 films/*p*-Si, Pt/TiO_2 film/*p*-Si, TiO_2 NRs/*p*-Si and Pt/TiO_2 NRs/p-Si photocathodes plotted as log (j) against potential vs. RHE. (b)-(c) The corresponding Nyquist impedance plots and its equivalent circuit (inset).

The electrochemical impedance spectroscopy (EIS) measurements to elucidate the charge-transfer resistances in the S2, S3, S5 and S6 samples as shown in figure 2.11 (b) and (c). The external bias voltages for the EIS measurements of the samples were selected by considering the onset potentials of the individual samples. The S2 sample showed a single semicircle in the Nyquist plot due to the negligible series resistance of the thin TiO_2 layer. The other three samples displayed two semicircles, as shown in Figures 4b and 4c. The measured data were fitted to the equivalent circuit in the inset of Figure 4b, consisting of constant phase elements (CPEs) associated with the Si substrate (CPE_{Si}) and the TiO_2 layer (CPE_{TiO2}) and charge-transfer resistances (R_{ct}) from the Si to TiO_2 (R_{ct_Si}) and from TiO_2 to the redox couples in the electrolyte (R_{ct_TiO2}). The first semicircles in the Nyquist plot yield R_{ct_Si}, whereas the second semicircles are related to R_{ct_TiO2}. The charge-transfer resistances obtained from the fittings are summarized in **Table 2.1**. The R_{ct_TiO2} of the S3 sample (346 Ωcm^2) was still lower than that of the S2 sample (505.97 Ωcm^2), confirming that the

electron transfer from as-grown TiO_2 NRs to the redox couples where protons were reduced was indeed enhanced. After the TiO_2 surface was decorated with Pt nanoparticles, the R_{ct_TiO2} decreased to 20.3 Ωcm^2 for the S5 sample and 51.96 Ωcm^2 for the S6. Following Pt decoration, R_{ct_Si} also decreased due to the charge transfer between the TiO_2 and the electrolyte affects that between the *p*-Si and the TiO_2

Photocathode	R_{ct_si} (Ω cm^2)	R_{ct_TiO2} (Ω cm^2)	App. volt.
TiO_2 seed layer/*p*-Si (S2)	23.94	505.97	–450 mV
Pt/TiO_2 seed layer/*p*-Si (S5)	2.94	20.3	~ 300 mV
Pt/TiO_2 NRs/*p*-Si (S6)	1.57	51.96	~ 300 mV
TiO_2 NRs/*p*-Si (S3)	29.39	346	~ 200 mV

Table 2-2. The fitted charge transfer resistance between the interfaces

Considering the ideal regenerative cell efficiency which can be measure by a three electrode system and the applied-bias photon-to-current efficiency (ABPE) which must be measure by a two electrode systems configuration are comparable. The ideal regenerative cell efficiency (η_{IRC}) of best photocathode, Pt/TiO_2 NRs/*p*-Si, was measured as suggested by Robert H. Coridan et al[10]. The maximum power point potential (V_{mpp}) and the maximum power point current density (J_{mp}) of the photocathode was 0.13 V vs. RHE and 19.11 mA cm^{-2}, respectively as shown in the Figure 2.10a. The calculated V_{mmp} and J_{mmp} of the photocathode was used to calculate the η_{IRC} of the photoelectrode.

The ideal regenerative cell efficiency is given by:

$$\eta_{IRC} = \frac{V_{mp} \times J_{mp}}{I_s} = \frac{J\left(E\left(A/A^-\right)\right) \times V_{oc} \times ff}{I_s} \quad ---(2.1)$$

Where J is the photocurrent density at zero bias, I_s intensity of illuminated light (100 $mWcm^{-2}$) and ff is the fill factor. The calculated ideal regenerative cell efficiency of the Pt/TiO_2 NRs/*p*-Si photocathode was 2.5%.

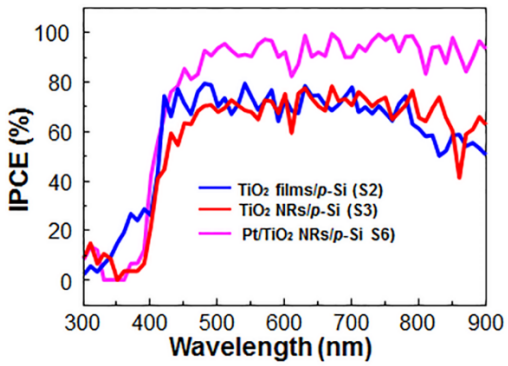

Figure 2.12. The incident photon to current conversion efficiency of TiO_2 films/*p*-Si, TiO_2 NRs/*p*-Si and Pt/TiO_2 NRs/*p*-Si

The ability of a photocathode sample to convert the absorbed photons to useful electrical current was examined by measuring the incident photon to current conversion efficiency (IPCE) as shown in Figure 2.12. The IPCE spectra of S2, S3 and S6 samples were measured using the applied potentials at which the saturated photocurrent of the photocathode was obtained. The Pt/TiO_2 NRs/*p*-Si photocathode was exhibit the IPCE values of ~90% in the entire visible light spectrum. The TiO_2 films/*p*-Si and TiO_2 NRs/*p*-Si photocathodes showed about 70% IPCE values, clarifying the high quantum efficiency of the Pt/TiO_2 NRs/*p*-Si photocathode due to the antireflective properties of TiO_2 NRs.

The chronoamperometry of S4, S5 and S6 photocathode samples were measured Figure 2.13. The photocurrent of S6 was stable for >40 h. The LSV curve measured after 40 h (Figure 2.13, inset) is similar to that measured before the chronoamperometry test. After letting the sample stand in air ambient for 1 week, we measured the LSV curves again. After more than 300 cycles, the sample

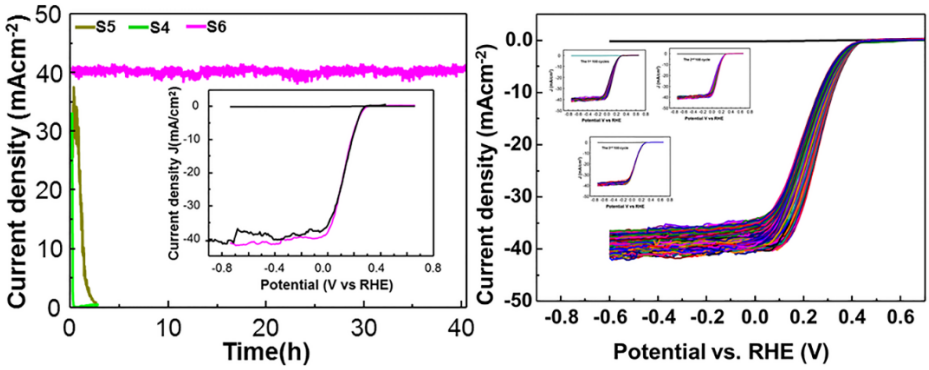

Figure 2.13. Stability test. (a) ChronoAmperometry of (2.5nm)Pt/TiO_2NR/*p*-Si (pink colour) and (2.5nm/5nm film) Pt/TiO_2/*p*-Si (dark yellow colour) and green colour bare *p*-Si measured at 0.0 V vs RHE. Inset LSV curve is measured after 40 h stability test.

Showed no considerable degradation of PEC performance, as shown in Figure 2.13 b. In contrast, the S4 sample was highly degraded and showed no photocurrent in tens of minutes that corroborate with the works of L. Ji, et al.[27,64] However, after etching the photocathode for ~ 20s in 2% HF the photocurrent was restored. It confirms the formation of insulating oxide layer on the surface that causes the bare silicon photocathode unstable.[57] For the S5 sample, the saturated photocurrent was maintained for only 1 h and then the current density

decreased at ~0.23 $mAcm^{-2}$/min, approaching zero after 3 h. This indicates that the TiO_2 seed layer was too thin to protect against corrosion of *p*-Si.[30,65]

Photocathode	Onset potential vs. RHE (V)	Saturation current density (mA cm^{-2})	IPCE %	Reflectance % arithmetic mean	Stability (h)
Bare *p*-Si	–0.75	32	-	37.5	
TiO_2 film/*p*-Si	–0.50	33	~70	34.4	
TiO_2 NRs/*p*-Si	0.0	42	~70	1.4	
Pt/TiO_2 film/*p*-Si	0.44	33			
Pt/TiO_2 NRs/*p*-Si	0.44	42	~90	1.4	More than 52
Pt/*p*-Si	0.44	32			

Table 2-3. Summary of the onset potential, saturation current density, IPCE and arithmetic Reflectance

2.6. Conclusion

Highly uniform and multifunctional TiO_2 NRs with tailored length and dimeter were grown on a 4-inch *p*-silicon substrate using a hydrothermal synthesis method. The synthesized TiO_2 NRs showed better catalytic properties resulted in a high anodic potential shift and facilitates transfer of photogenerated minority carriers from the photon-absorbing substrate (silicon) to the electrolyte. The TiO_2 nanorods also dramatically reduce the optical reflectance of silicon due to the antireflective ability of the nanorods. The reflectance of silicon is decreased from 37.5% to 1.4% and enhances the saturated photocurrent density. The Pt-decorated (1-2.5 nm diameter) TiO_2 NRs/*p*-Si photocathodes was showed a short circuit current density of up to 40 mA cm^{-2}, an open circuit voltage ~440 mV with incident photon to current conversion efficiency of more than 90% using 0.5 M H_2SO_4 electrolyte and simulated 1 sun irradiation. The heterostructure photocathodes are stable more than 52 h without noticeable degradation with an ideal regenerative cell efficiency of 2.5%.

2.7. References

1 McGlade, C. & Ekins, P. The geographical distribution of fossil fuels unused when limiting global warming to 2° C. *Nature* **517**, 187-190 (2015).

2 Benck, J. D., Hellstern, T. R., Kibsgaard, J., Chakthranont, P. & Jaramillo, T. F. Catalyzing the Hydrogen Evolution Reaction (HER) with Molybdenum Sulfide Nanomaterials. *ACS Catalysis* **4**, 3957-3971 (2014).

3 Osterloh, F. E. & Parkinson, B. A. Recent developments in solar water-splitting photocatalysis. *MRS bulletin* **36**, 17-22 (2011).

4 Tachibana, Y., Vayssieres, L. & Durrant, J. R. Artificial photosynthesis for solar water-splitting. *Nature Photonics* **6**, 511-518 (2012).

5 Liu, R., Zheng, Z., Spurgeon, J. & Yang, X. Enhanced photoelectrochemical water-splitting performance of semiconductors by surface passivation layers. *Energy & Environmental Science* **7**, 2504-2517 (2014).

6 Moniz, S. J., Shevlin, S. A., Martin, D. J., Guo, Z.-X. & Tang, J. Visible-light driven heterojunction photocatalysts for water splitting–a critical review. *Energy & Environmental Science* **8**, 731-759 (2015).

7 Kargar, A. *et al.* Tailoring n-ZnO/p-Si branched nanowire heterostructures for selective photoelectrochemical water oxidation or reduction. *Nano letters* **13**, 3017-3022 (2013).

8 Dai, P. *et al.* Solar hydrogen generation by silicon nanowires modified with platinum nanoparticle catalysts by atomic layer deposition. *Angewandte Chemie* **125**, 11325-11329 (2013).

9 Li, X. *et al.* Engineering heterogeneous semiconductors for solar water splitting. *Journal of Materials Chemistry A* **3**, 2485-2534 (2015).

10 Khan, S. U., Al-Shahry, M. & Ingler, W. B. Efficient photochemical water splitting by a chemically modified n-TiO2. *science* **297**, 2243-2245 (2002).

11 Chen, S. & Wang, L.-W. Thermodynamic oxidation and reduction potentials of photocatalytic semiconductors in aqueous solution. *Chemistry of Materials* **24**, 3659-3666 (2012).

12 Hu, S. *et al.* Thin-Film Materials for the Protection of Semiconducting Photoelectrodes in Solar-Fuel Generators. *The Journal of Physical Chemistry C* **119**, 24201-24228 (2015).

13 Chen, Y.-H. *et al.* Three-dimensional heterostructured ZnSe nanoparticles/Si wire arrays with enhanced photodetection and photocatalytic performances. *Journal of Materials Chemistry C* **1**, 1345-1351 (2013).

14 Choi, M. J. *et al.* Long-term durable silicon photocathode protected by a thin Al 2 O 3/SiO x layer for photoelectrochemical hydrogen evolution. *Journal of Materials Chemistry A* **2**, 2928-2933 (2014).

15 Cai, J. & Qi, L. Recent advances in antireflective surfaces based on nanostructure arrays. *Materials Horizons* **2**, 37-53 (2015).

16 Chen, Z., Dinh, H. N. & Miller, E. Photoelectrochemical water splitting. *Standards, Experimental Methods, and Protocols [Online]* (2013).

17 Ji, L. *et al.* A silicon-based photocathode for water reduction with an epitaxial SrTiO3 protection layer and a nanostructured catalyst. *Nature nanotechnology* **10**, 84-90 (2015).

18 Esposito, D. V., Levin, I., Moffat, T. P. & Talin, A. A. H2 evolution at Si-based metal–insulator–semiconductor photoelectrodes enhanced by

inversion channel charge collection and H spillover. *Nature materials* **12**, 562-568 (2013).

19 Hu, S. *et al.* Amorphous TiO_2 coatings stabilize Si, GaAs, and GaP photoanodes for efficient water oxidation. *Science* **344**, 1005-1009 (2014).

20 Seger, B. *et al.* Using TiO_2 as a conductive protective layer for photocathodic H2 evolution. *Journal of the American Chemical Society* **135**, 1057-1064 (2013).

21 Andoshe, D. M., Jeon, J.-M., Kim, S. Y. & Jang, H. W. Two-Dimensional Transition Metal Dichalcogenide Nanomaterials for Solar Water Splitting. *Electron. Mater. Lett* **11**, 323-335 (2015).

22 Lin, Y. *et al.* Role of TiO2 Surface Passivation on Improving the Performance of p-InP Photocathodes. *The Journal of Physical Chemistry C* **119**, 2308-2313 (2015).

23 Cabán-Acevedo, M. *et al.* Efficient hydrogen evolution catalysis using ternary pyrite-type cobalt phosphosulphide. *Nature Materials* (2015).

24 Lukowski, M. A. *et al.* Enhanced hydrogen evolution catalysis from chemically exfoliated metallic MoS2 nanosheets. *Journal of the American Chemical Society* **135**, 10274-10277 (2013).

25 Kim, H. *et al.* Coordination tuning of cobalt phosphates towards efficient water oxidation catalyst. *Nature communications* **6** (2015).

26 Li, H. *et al.* Activating and optimizing MoS2 basal planes for hydrogen evolution through the formation of strained sulphur vacancies. *Nature materials* (2015).

27 Bae, D. *et al.* Protection of Si photocathode using TiO 2 deposited by high power impulse magnetron sputtering for H 2 evolution in alkaline media. *Solar Energy Materials and Solar Cells* **144**, 758-765 (2016).

28 Feng, J. *et al.* Nickel-coated silicon photocathode for water splitting in alkaline electrolytes. *Nano Research* **8**, 1577-1583 (2014).

29 Chen, C.-J. *et al.* An integrated cobalt disulfide (CoS 2) co-catalyst passivation layer on silicon microwires for photoelectrochemical hydrogen evolution. *Journal of Materials Chemistry A* (2015).

30 Sze, S. M. *Semiconductor devices: physics and technology*. (John Wiley & Sons, 2008).

31 Zhao, Z., Li, Z. & Zou, Z. Surface properties and electronic structure of low-index stoichiometric anatase TiO2 surfaces. *Journal of Physics: Condensed Matter* **22**, 175008 (2010).

32 Azarpira, A. *et al.* Efficient and Stable TiO2: Pt–Cu (In, Ga) Se2 Composite Photoelectrodes for Visible Light Driven Hydrogen Evolution. *Advanced Energy Materials* (2015).

33 Bube, R. H. *Electrons in solids: an introductory survey*. (Academic press, 1992).

34 Liu, G., Jaegermann, W., He, J., Sundström, V. & Sun, L. XPS and UPS characterization of the TiO2/ZnPcGly heterointerface: alignment of energy levels. *The Journal of Physical Chemistry B* **106**, 5814-5819 (2002).

35 Xiong, G. *et al.* Photoemission electron microscopy of TiO2 anatase films embedded with rutile nanocrystals. *Advanced Functional Materials* **17**, 2133-2138 (2007).

36 Onda, K., Li, B. & Petek, H. Two-photon photoemission spectroscopy of Ti O 2 (110) surfaces modified by defects and O 2 or H 2 O adsorbates. *Physical Review B* **70**, 045415 (2004).

37 Chung, Y., Lo, W. & Somorjai, G. Low energy electron diffraction and electron spectroscopy studies of the clean (110) and (100) titanium dioxide (rutile) crystal surfaces. *Surface Science* **64**, 588-602 (1977).

38 Zhang, Z. & Yates Jr, J. T. Band bending in semiconductors: chemical and physical consequences at surfaces and interfaces. *Chemical reviews* **112**, 5520-5551 (2012).

39 Scanlon, D. O. *et al.* Band alignment of rutile and anatase TiO2. *Nature materials* **12**, 798-801 (2013).

40 DeVore, J. R. Refractive indices of rutile and sphalerite. *JOSA* **41**, 416-417 (1951).

41 Chandler-Horowitz, D. & Amirtharaj, P. M. High-accuracy, midinfrared (450 cm-1<= omega<= 4000 cm-1) refractive index values of silicon. *Journal of applied physics* **97**, 3526 (2005).

42 Kumar, A., Madaria, A. R. & Zhou, C. Growth of aligned single-crystalline rutile TiO2 nanowires on arbitrary substrates and their application in dye-sensitized solar cells. *The Journal of Physical Chemistry C* **114**, 7787-7792 (2010).

43 Ni, M., Leung, M. K., Leung, D. Y. & Sumathy, K. A review and recent developments in photocatalytic water-splitting using TiO2 for hydrogen production. *Renewable and Sustainable Energy Reviews* **11**, 401-425 (2007).

44 Hu, Y. H. A Highly Efficient Photocatalyst—Hydrogenated Black TiO2 for the Photocatalytic Splitting of Water. *Angewandte Chemie International Edition* **51**, 12410-12412 (2012).

45 Ding, Q. *et al.* Efficient Photoelectrochemical Hydrogen Generation Using Heterostructures of Si and Chemically Exfoliated Metallic MoS2. *Journal of the American Chemical Society* **136**, 8504-8507 (2014).

46 Oh, J., Yuan, H.-C. & Branz, H. M. An 18.2%-efficient black-silicon solar cell achieved through control of carrier recombination in nanostructures. *Nature nanotechnology* **7**, 743-748 (2012).

47 Boettcher, S. W. *et al.* Photoelectrochemical hydrogen evolution using Si microwire arrays. *Journal of the American Chemical Society* **133**, 1216-1219 (2011).

48 Kolen'ko, Y. V. *et al.* Hydrothermal synthesis and characterization of nanorods of various titanates and titanium dioxide. *The Journal of Physical Chemistry B* **110**, 4030-4038 (2006).

49 Einarsrud, M.-A. & Grande, T. 1D oxide nanostructures from chemical solutions. *Chemical Society Reviews* **43**, 2187-2199 (2014).

50 Richter, A., Hermle, M. & Glunz, S. W. Reassessment of the limiting efficiency for crystalline silicon solar cells. *Photovoltaics, IEEE Journal of* **3**, 1184-1191 (2013).

51 Vilekar, S. A., Fishtik, I. & Datta, R. Kinetics of the hydrogen electrode reaction. *Journal of The Electrochemical Society* **157**, B1040-B1050 (2010).

52 Skúlason, E. *et al.* Modeling the electrochemical hydrogen oxidation and evolution reactions on the basis of density functional theory calculations. *The Journal of Physical Chemistry C* **114**, 18182-18197 (2010).

53 Benson, J., Li, M., Wang, S., Wang, P. & Papakonstantinou, P. Electrocatalytic Hydrogen Evolution Reaction on Edges of a Few Layer Molybdenum Disulfide Nanodots. *ACS applied materials & interfaces* **7**, 14113-14122 (2015).

54 Coridan, R. H. *et al.* Methods for comparing the performance of energy-conversion systems for use in solar fuels and solar electricity generation. *Energy & Environmental Science* **8**, 2886-2901 (2015).

55 Kwon, K. C. *et al.* Wafer-scale transferable molybdenum disulfide thin-film catalysts for photoelectrochemical hydrogen production. *Energy & Environmental Science* (2016).

56 Lin, Y. *et al.* Amorphous Si thin film based photocathodes with high photovoltage for efficient hydrogen production. *Nano letters* **13**, 5615-5618 (2013).

Chapter 3

Titanium dioxide-coated *p*-type silicon photocathode for photoelectrochemical water spiting with a three-dimensional molybdenum disulfide hydrogen evolution catalyst

3.1. Introduction

In the previous chapter a hydrothermally grown TiO_2 NRs on *p*-Si photocathode can passivate the surface of the electrode from corrosion for extended operation time and can be a perfect antireflective coating that decrease the reflectance of silicon photocathode. Even though the overpotential of *p*-Si photocathode was decrease after the TiO_2 NRs was grown, the overpotential to derive the water reduction using TiO_2 NRs/*p*-Si photocathode is still high. To lower this overpotential extremely small (0.5-1 nm radius) Pt nanoparticles was deposited and the Pt/TiO_2/*p*-Si photocathode showed best solar water splitting performance. However, due to the scarcity of noble metals have increases the cost of hydrogen fuel and hinders large-scale production. Therefore, it is needed to explore new chemistry to support and facilitate the production of hydrogen fuel at low costs.

It is known that transition metal dichalcogenides (TMDs) exhibit a wide range of electronic, optical, mechanical, chemical, and thermal properties that have been studied for decades. They have been used for different applications such as catalysts for the removal of sulfur (hydrodesulfurization) and nitrogen (hydrogenitrogenation), product quality improvement by hydrotreating and hydroconverting from petroleum feedstock,[66] additives for reducing friction,[67] and as cathodes for rechargeable lithium ion batteries.[68,69]

Because of recent advancement in sample preparation and manipulation of 2D materials, and physical understanding obtained from graphene,[70] recently, there has been a resurgence of scientific and engineering interest in the atomically

thin 2D form of TMD to use as catalysts for electrochemical and photoelectrochemical water splitting. The catalytic activities of nanostructure 2D TMDs for the hydrogen evolution catalyst (HER) makes it a promising candidate to replace the noble metals catalysts, which would expand and enrich the family of materials suitable as efficient HER catalysts since TMDs have reach set of combination as shown in the Figure 3.1.

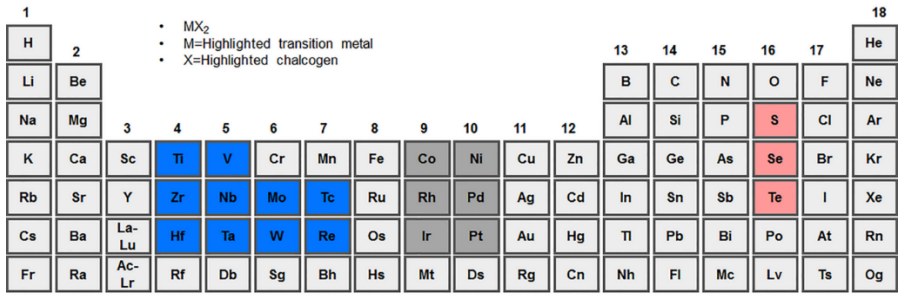

Figure 3.1. Periodic table of the elements with candidate of TMDs (MX_2) highlighted by blue color and red. Among sixty different TMDs, more than two-thirds have layered structures.

Among the TMDs catalysts to decrease the overpotential of the *p*-type Si (*p*-Si) photocathode for the PEC hydrogen production, molybdenum disulfide (MoS_2) has gained considerable attention as a promising hydrogen evolution reaction (HER) catalyst owing to its low hydrogen adsorption free energy and the high photochemical stability at the affordable expenses, compared to conventional catalysts based on precious metals[55,71,72]. Transition from the indirect band-gap structures in bulk MoS_2 to the direct band-gap one in MoS_2 monolayers may also improve the charge transport efficiencies[73,74]. In particular, the edge-sites of MoS_2 are known to exhibit the highest catalytic properties for HER, as well as their sulfur vacancies and grain boundaries[75,76]. Thus, multiplying the

exposed edge-site density is directly related to developing efficient *p*-Si photocathodes with MoS_2 HER catalysts.

p-Si is not the best substrate for the direct deposition of atomically thin MoS_2 using the usual vapor deposition techniques because of the weak van der Waals interaction between Si and sulfur (the surface terminating atom in MoS_2)[77,78]. To date, most of the MoS_2 films have been deposited on silicon dioxides[22] or sapphires and manually transferred to the *p*-Si substrates[64,79-81] to form HER catalysts. However, this manual transfer is not immune from unwanted organic contaminants, and the poor adhesion of transferred MoS_2 layers to the *p*-Si substrates deteriorates the interfacial charge transport. In addition, the MoS_2 catalyst layers can be easily peeled off from the *p*-Si photocathode after several tens of hours of hydrogen production. Thus, direct synthesis of MoS_2 catalysts on *p*-Si substrates is crucial to achieving the efficient solar HER.

3.2. Three-Dimensional MoS_2 film growth on TiO_2/*p*-Si photocathode substrates

3.2.1. TiO_2 coating on a *p*-type silicon substrate.

A *p*-type Si (100) substrate was cleaned using acetone and isopropanol alcohol (IPA) assisting with sonication, and washed repeatedly in DI water. Subsequently, it was soaked in 2% HF for 1 min to remove residues and native oxides and was washed in DI water. Then a 10 nm thick TiO_2 film was deposited at a rate of 0.1 $Åsec^{-1}$ using an electron-beam evaporator (KVE-E2004L) at 3.5 x 10^{-6} Torr.

3.2.2. Growth of 3D MoS_2 layers in wafer scale.

The 4-in. wafer-scale growth of MoS_2 films was carried out using high purity gas precursor molybdenum hexacarbonyl (MHC) (99.9%) and diethyl sulfide (DES) (98%). A 4-in. TiO_2 (10 nm) coated *p*-Si wafer is located in the center of a hot-walled quartz-tube furnace. Prior to heating, the furnace was purged for 30 min to eliminate residual gases, and subsequently was ramped up to 560 °C for 20 min. Then, the precursors and a carrier gas were flowed. We proceeded the growth for 15 minutes and rapidly cooled down to room temperature. The flow rates of precursors were 0.4 sccm for MHC, 10 sccm for DES, 20 sccm for H_2 (99.9999%), and 150 sccm for Ar (99.9999%).

3.3. Characterization

3.3.1. Physical characterization.

For TEM specimen preparations, we transferred our 3D MoS_2 using a wet transfer method. The grown sample was spin-coated by poly (methyl methacrylate) (PMMA) and baked at 180 °C for 1 m and 30 s. Then, substrate (SiO_2) was etched in HF (10%). We transferred floating PMMA/samples to a TEM grid (holey carbon coated with 400-meshed Cu), and then, we removed PMMA films in acetone for 6 hours and annealed in a tube furnace at 300 °C. High-resolution TEM image and EDS elemental analysis was taken using a JEOL JEM-2100F operated at 200 kV (equipped with a Cs-corrector). Furthermore, it was employed field emission scanning electron microscope (ZEISS, MERLIN Compact). Angle-dependent reflectance measurement of the sample was carried out using a homemade system equipped with an automatic

rotating sample stage and a photodetector. The incident light was generated from a Xe arc lamp source with a monochromator (Mmac-200).

3.3.2. Photoelectrochemical measurements.

The photoelectrochemical properties of the photocathode were measured using a computer controlled potentiostat (IVIUM Technologies, nSTAT). All the PEC measurements were performed with a 0.5 M H_2SO_4 electrolyte, single compartment cuvette and three electrodes configuration, such as, the prepared photocathode, saturated calomel electrode and graphite rod as working, reference and counter electrode respectively. A Xe arc lamp was used as a light source and calibrated to 100 mW cm^{-2} using a standard silicon photodiode at the sample location. In all of the linear sweep voltammogram measurements, the photoanodes were cathodically polarized at the scan rate of 20 mV/sec during both illumination and in the dark measurement. The measured potential *V* vs. calomel were converted to reference hydrogen electrode (RHE) using the following equation.

$$V_{RHE} = E + E_{\text{calomel}} + 0.059 \times \text{pH} \text{ ------ (3.1)}$$

Where *E* is applied potential vs. calomel and calomel is 0.24 V vs RHE and V_{RHE} is the applied bias potential vs. RHE. The external quantum efficiency of the samples were measured at applied bias potential vs. calomel using computer controlled monochromator (MonoRa150) and an amplifier for photocurrent detection. The electrochemical impedance spectroscopy (EIS) was measured at 0.0 V vs. calomel with respect to open circuit potential (OCP) and sweeping in

the frequency range of 350 K Hz – 0.1Hz with an AC amplitude of 10 mV. The EIS Nyquist curves were fitted to equivalent circuit using Z-plot 2x software.

3.3.3. DFT Calculations.

DFT calculations were performed by a projector augmented wave (PAW) method,[82] with Vienna Ab initio Simulation Package (VASP)[83,84]. The generalized gradient approximation (GGA) suggested by Perdew, Burke and Ernzrh of (PBE) [85,86] was used for exchange correlation function. Van der Waals force was considered by the Grimme D2 scheme[87]. The basal plane was modeled as 4×4×1 single layer supercell, and the unit cell for the Mo-edge site was modeled by stripe with 5 Mo atoms in both the *x*- and *y*-direction as shown in Fig. 4d inset. Two types of Mo-edges exists in MoS_2; one terminated with S-monomer and the other terminated with S-dimer. It is known in previous researches that hydrogens are absorbed on Mo-edge terminated with S-monomer[88], so only one with S-monomer was calculated. The vacuum region was implemented as 15 Å thickness was used to avoid spurious electrostatic interactions. The plane-wave cutoff energy of 260 eV was used. The Brillouine zone was sampled by 5×5×1 Monkhorst-Pack mesh for unit cell, 2×2×1 for the basal plane, and 4×1×1 for the Mo-edge site. Gibbs free energy of the adsorption was obtained as follows:

$$\Delta G_H = \Delta E_H + ZPE - T\Delta S_H \text{--------} (3.2)$$

where ΔE_H is hydrogen adsorption energy, ZPE is zero-point energy, T is the temperature, and ΔS_H is entropy change on H adsorption. The entropy is only

considered for hydrogen gas. Coverage of hydrogen θ was defined as the proportion of S-monomers at which hydrogen atoms are attached. Adsorption energy ΔE_H was calculated using following equation:

$$\Delta E_H = E(*nH) - E(*(n\text{-}1)H) - \tfrac{1}{2}E(H_2)\text{--------} \qquad (3.3)$$

Where E (*nH) is the total energy of MoS_2 system that n edge sites are covered with hydrogen and E (H_2) is the total energy of a hydrogen molecule.

3.4. Result and Discussion

3.4.1. Physical and optical properties of the deposited 3D MoS_2 on TiO_2 coated *p*-Si

Figure 3.1 shows an optical image of TiO_2 coated and 3D MoS_2 deposited on TiO_2 coated 4-inch *p*-type silicon with their corresponding Raman spectra. The uniform coverage of the 3D MoS_2 films was investigated by Raman scattering spectra is shown in Figure 3.1b, obtained at various areas over the entire wafer. The representative Raman spectra obtained from the marked spots as [1] to [5] in the Figure 3.1a consistently show two characteristic peaks of few-layer MoS_2, *i.e*., the in-plane vibrational E_{2g} mode in the range ~380–381 cm^{-1} and the out-of-plane vibrational A_{1g}

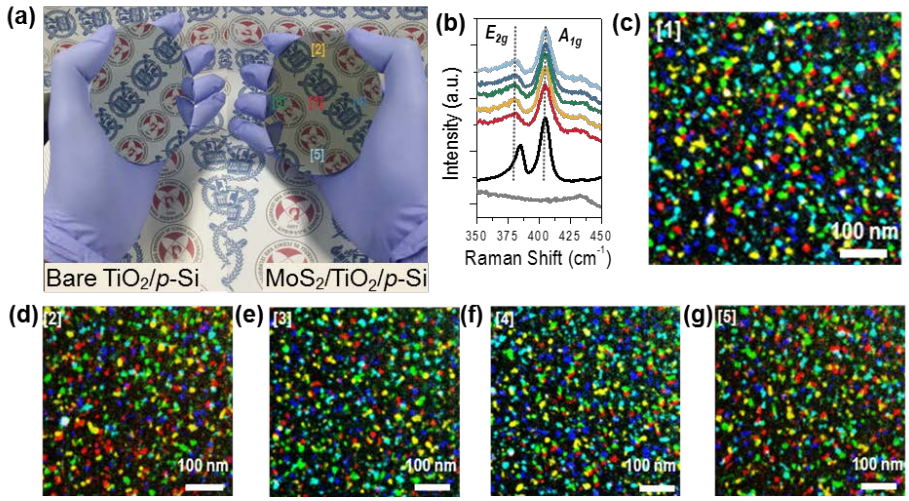

Figure 3.2. Wafer-scale 3D MoS_2 film growth by metal-organic chemical vapor deposition (MOCVD). (a) Optical image of bare TiO_2 coated on 4-inch *p*-type silicon and 3D MoS_2 on TiO_2 coated 4-inch p-type silicon (b) Raman scattering spectra acquired from d different regions in (a) with those of monolayer MoS_2 film (black) and bare TiO_2/*p*-Si (gray) for comparison (c)-(g) Wafer-scale homogeneity of false-color DF-TEM images acquired from region [1]-[5].

Mode in the range ~404–405 cm^{-1}. The frequency difference of the two peaks, $\Delta\omega$, which is strongly dependent on the layer number, was consistently observed to be in the range ~23–25 cm^{-1} ($\Delta\omega$ ~19.5 cm^{-1} for MoS_2 monolayer), indicating the nominal layer number is greater than 3 in our 3D films[89,90]. We also observed that the E_{2g} peaks are weaker, compared to the A_{1g} peaks, with generic peak broadening, suggesting that the film is 3D-textured, instead of 2D monolayers or bilayers[91]; the full width half maximum (FWHM) was estimated to be 13.8 and 11.2 cm^{-1} for the E_{2g} and A_{1g} modes, respectively, while the FWHM in our monolayer films is 12.1 cm^{-1} (E_{2g}) and 8.4 cm^{-1} (A_{1g}).

In stark contrast with the conventional layer-by-layer growth of 2D MoS_2, the 3D MoS_2 growth was characterized by a large fraction of vertically-aligned MoS_2 on the top of underlying MoS_2 polycrystalline films of a relatively small grain size.

This unique film texture of the 3D MoS_2 was obtained at a high flux rate growth, *i.e.*, an MHC flow rate of 0.4 sccm and the DES rate of 8.5 sccm for 15 min. The cross sectional TEM image with the corresponding EDS elemental analysis is shown in the Figure 3.2.

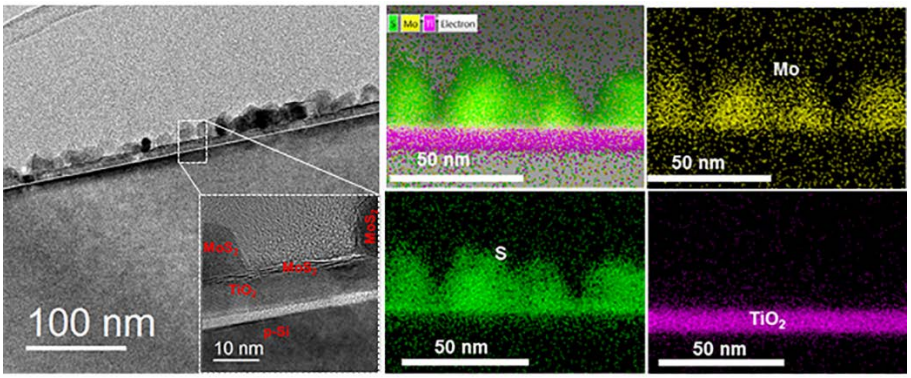

Figure 3.3. Cross sectional TEM image and EDS elemental analysis of 3D MoS_2 grown directly on the TiO_2 coated *p*-type silicon.

Likewise, the plain view of a TEM image, where the edge-exposed vertical MoS_2 few-layers coexist with the underlying MoS_2 films is shown in Figure 3.3a. The high-resolution TEM images, obtained from each region marked with red and blue box in Fig. 3.3a, verify the corresponding vertical and in-plane crystal structures of few-layer MoS_2. The measured inter-planar distances were 0.660 nm Fig. 3b and 0.312 nm (Fig. 3c), consistent with the (0001) and (10-10) plane of hexagonal MoS_2, respectively. The areal density of the vertical

MoS_2 was estimated to be ~50%, according to the representative scanning electron microscope image in Figs. 3d. In Fig. 3e, the in-plane dark-field TEM image with false colors, each of which corresponds to the in-plane crystal orientations, defined by diffraction patterns of Fig. 3f, shows a polycrystalline grain distribution. Quantitatively, its grain size ranged from 2 to 20 nm with an average size of 8 nm by counting its

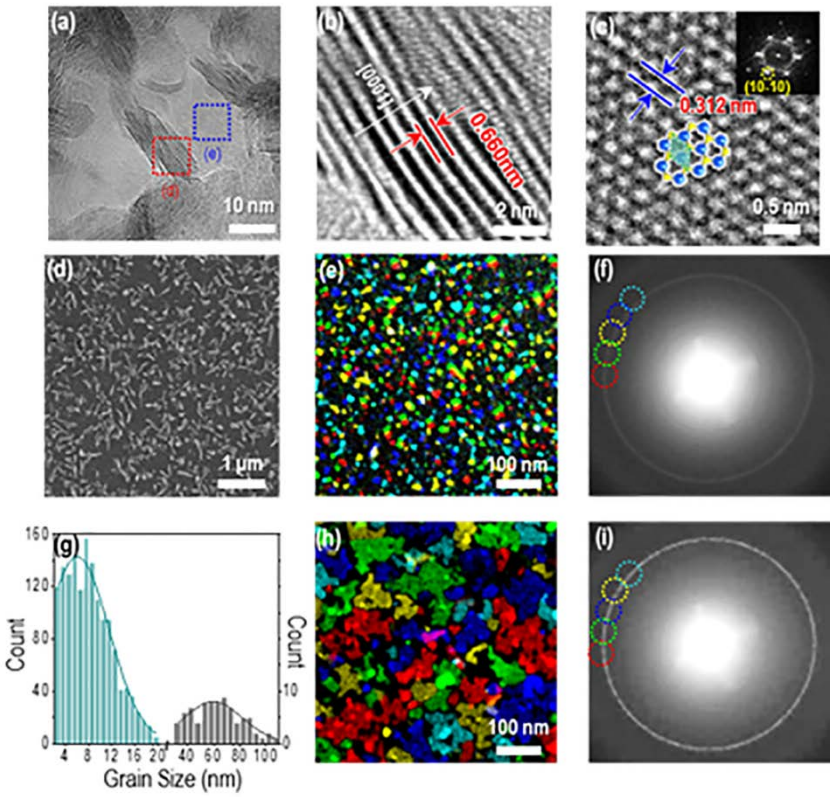

Figure 3.4. (a) Low-magnification transmission electron microscope image of 3D MoS2 film. (b)-(c) High-magnification TEM images of vertically-aligned (red color box) and in-planar region (blue color box) taken from marked areas in (a). (d) Plane view scanning electron microscope image, (e) false-color dark-field-TEM image and (f) selected area electron diffraction (SAED) pattern taken from 3D MoS_2. (**g)** Grain size distribution of 3D MoS_2 film (green) and layer-by-layer grown MoS_2 film (gray). (h) False-color DF-TEM image and (i) SAED pattern taken from layer-by-layer grown MoS_2.

Size from more than five TEM images taken from the entire wafer (see also Figure 3.1. (c)-(g) For the wafer-scale uniformity). In contrast, the lower flux rate growth at an MHC flow rate of 0.0001 sccm and the DES rate of 0.15 sccm

establishes the conventional layer-by-layer growth mode without any vertical MoS_2 films, requiring 16 h to cover up the entire wafer (Fig. 3.4). In this growth mode, the typical grain size was found to be ~60 nm (Figs. 3.3 g and h).

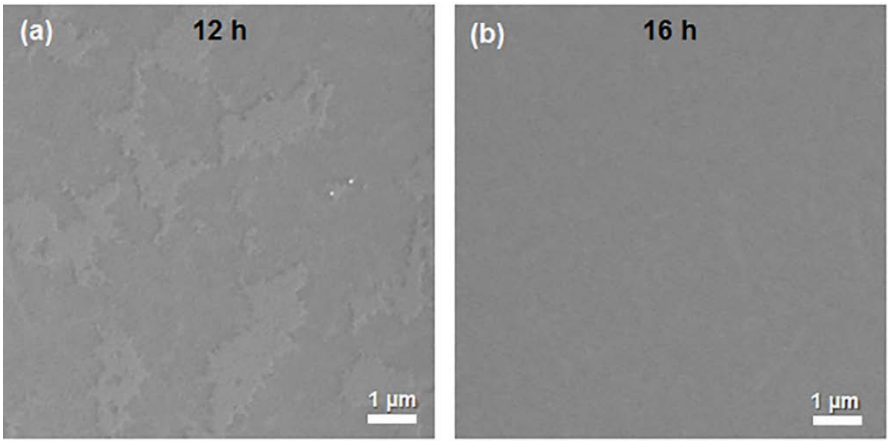

Figure 3.5. SEM image of conventional layer-by-layer/2D MoS_2 growth mode (a) acquired after 12 hour growth (partially covered) and (b) after 16 hour growth (fully covered)

The optical reflectance (R) of 3D $MoS_2/TiO_2/p$-Si and TiO_2/p-Si samples was measured in the wavelength (λ) range of 400 nm to 1000 nm at an incident angle 40° and in the incident angle (θ) range of 10° to 70° at λ = 550 nm (**Fig. 3.5**). The arithmetic mean of the R vs. λ at θ = 40° and the R vs. θ measured at λ = 550 nm are found to be 35.2% and 34.0% for the TiO_2/p-Si and 21.9% and 21.9% for the 3D $MoS_2/TiO_2/p$-Si photocathode, respectively. The θ- and λ-dependent R of both the samples are smaller than that of the pristine TiO_2/p-type Si because of a gradient refractive index, 2.545/2.64/5.6[92,93]. The refractive index of the 3D MoS_2 structures covering 50% of the TiO_2/p-Si area was estimated to 2.545, considering the refractive index of the MoS_2 in parallel direction and areal density[94,95]. More importantly, in the 3D $MoS_2/TiO_2/p$-Si photocathode,

the variation of R in both R vs. θ and R vs. λ is negligible, indicating that the 3D MoS_2 film has omnidirectional and broadband antireflective properties for *p*-Si, presumably because of the size effect below the diffraction limit[96].

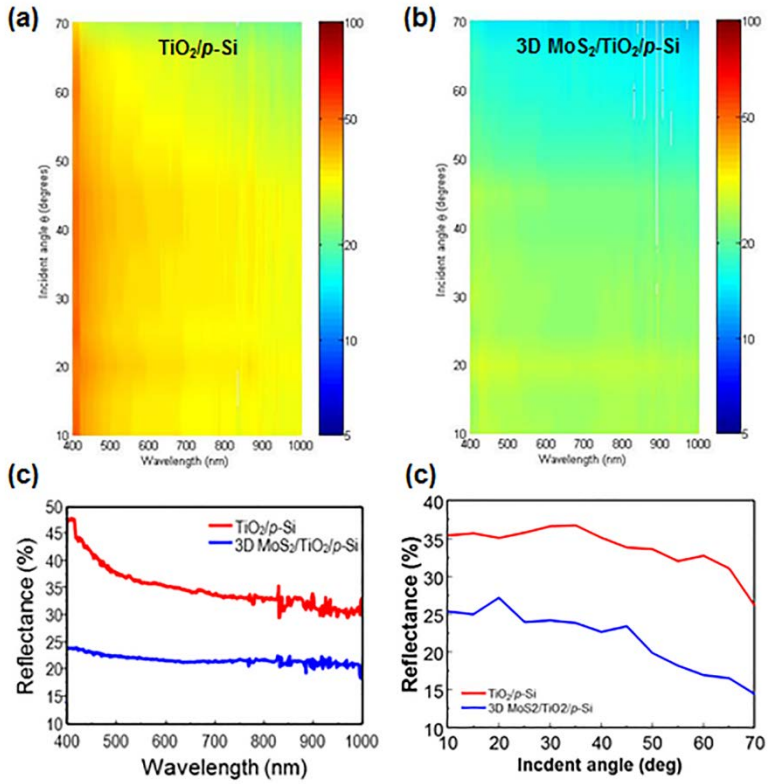

Figure 3.6. Incident angle dependent reflectance of, (a) TiO_2/*p*-Si (b) 3D MoS_2/TiO_2/p-Si (c) Reflectance vs. wavelength spectra of 3D-MoS2/TiO2/p-Si (blue) and bare TiO_2/*p*-Si (red) at the incident angle of 40°. (d) Reflectance plotted against incident angle for the TiO_2/*p*-Si, and MoS_2/TiO_2/*p*-Si photocathodes at wavelength of 550 nm.

Evidently, the 3D film texture was achieved by growth kinetics controls in the MOCVD growth. For example, the higher precursor flow rate substantially increases the numbers of nucleation sites for MoS_2 embryos and the growth rate, resulting in smaller grains and various vertical textures in the growth products,

respectively (Figs. 1i and 3a). Based on the cross-sectional TEM images, such 3D features were categorized into three types (Figs. 3.6b–d): (i) the direct vertical growth on the top of either TiO_2 or the bottom MoS_2 layers, (ii) the second one occurs when the two propagating MoS_2 layers collide head-on, pushing them in the upright direction, and (iii) when the MoS_2 layers are bent and rolled over, presumably at the defect sites.

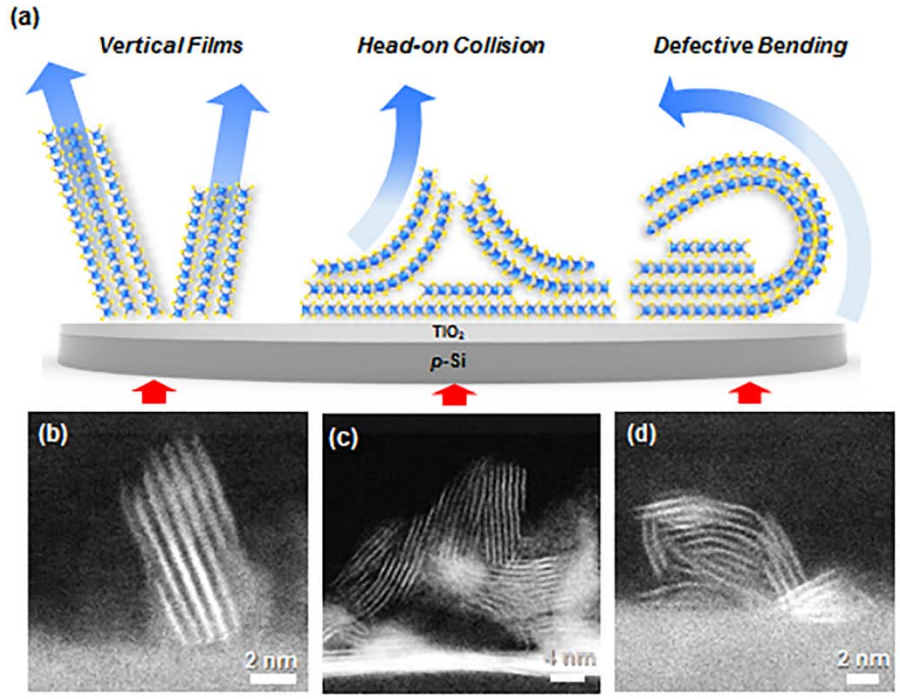

Figure 3.7. (a) Schematic illustration of vertically aligned textures observed in 3D MoS_2 films at high precursor flux rate. (b)-(d) Representative cross-sectional high-angle annular dark field-scanning TEM (HAADF-STEM) images showing different growth features.

3.4.2. Photoelectrochemical properties

The linear sweep voltammograms (LSV) of our 3D $MoS_2/TiO_2/p$-Si (blue color), 2D layered $MoS_2/TiO_2/p$-Si (red color), and TiO_2/p-Si (black color) photocathodes is shown Figure 3.7. The saturation current density of the 3D $MoS_2/TiO_2/p$-Si is ~37 mA cm^{-2}, whereas it was 33 and 32 mA cm^{-2} for the layered $MoS_2/TiO_2/p$-Si and TiO_2/p-Si, respectively. The enhanced saturation photocurrent density of $MoS_2/TiO_2/p$-Si photocathodes is due to the decrease of the *R* that increases the charge generation efficiency of the photocathode. The Chronopotentiometry of both 2D and 3D $MoS_2/TiO_2/p$-Si photocathodes at 1.00 mA cm^{-2} was measured using chopped light as shown in Fig. 3.7b. The onset potential of TiO_2/p-Si photocathode was found to be –0.41V, whereas it was 0.2 and 0.35 V for the 2D $MoS_2/TiO_2/p$-Si and 3D $MoS_2/TiO_2/p$-Si, respectively, assuming the onset potential of the photocathode is the potential at which the photocathode can generate a current density of 1.00 mA cm^{-2}. The onset potential of 3D $MoS_2/TiO_2/p$-Si photocathode shifted anodically by 0.76 and 0.15 V relative to those of TiO_2/p-Si and 2D $MoS_2/TiO_2/p$-Si photocathode, respectively, whereas it anodically shifted by 0.61 V for 2D $MoS_2/TiO_2/p$-Si photocathode, compared to that of the pristine TiO_2/p-Si photocathode. The high anodic onset potential shift in the 3D $MoS_2/TiO_2/p$-Si photocathode can be attributed to the existence of MoS_2 edge-sites in high density and much smaller size of grain boundaries, lacking in the 2D layered $MoS_2/TiO_2/p$-Si photocathode. A comparison of the PEC performance between the 3D $MoS_2/TiO_2/p$-Si photocathode and the state-of-the-art photocathodes reported using similar catalytic and optical absorption materials is shown in Fig. 3.7d.

Because of the highly populated edge-sites, the potential of the 3D $MoS_2/TiO_2/p$-Si photocathodes at 1 mA cm^{-2} is lower than those of either $MoS_x/MoS_2/Mo/n^+p$-Si[97] or $MoS_2/Ti/n^+p$-Si[98]. For the saturation current density and the current density at zero bias voltage, our photocathode shows the highest photocurrent density, mostly because of the improvement of charge generation efficiency and lower interfacial charge resistance.

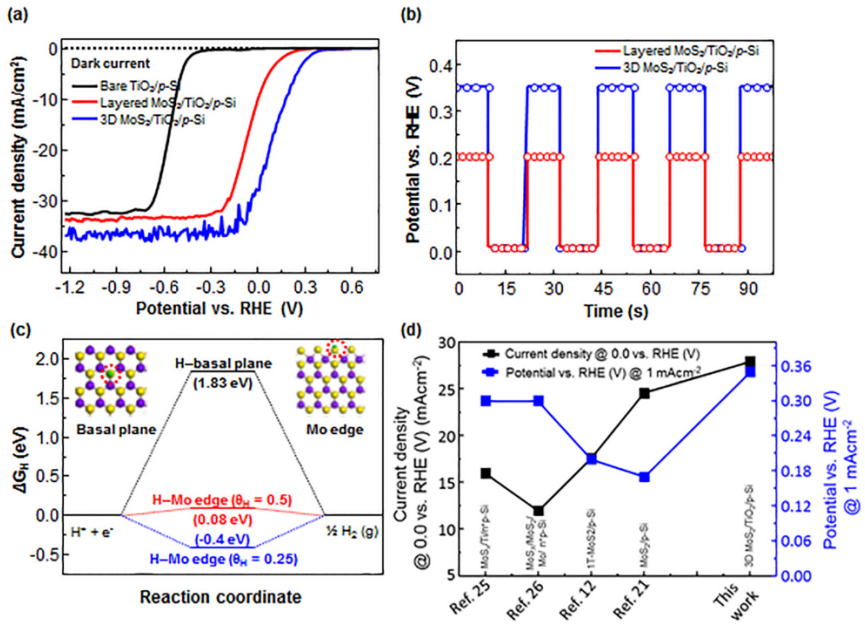

Figure 3.8. Figure 3.7. (a) The LSV of $MoS_2/TiO_2/p$-Si and TiO_2/p-Si (b) The onset potential of layered and 3D $MoS_2/TiO_2/p$-Si at –1 $mAcm^{-2}$. (c) Hydrogen adsorption free energy of MoS_2 basal plane, Mo edge calculated using DFT. (d) Comparison of PEC performance between our 3D $MoS_2/TiO_2/p$-Si and previously reported state-of-the art photocathode that used similar catalyst and photon absorption material.

Electrochemical impedance spectroscopy (EIS) measurements were performed to deduce the charge transfer resistance of the 3D $MoS_2/TiO_2/p$-Si and TiO_2/p-Si photocathodes. The Nyquist impedance plots are shown in Figure 3.8, where the TiO_2/p-Si photocathode has a greater diameter than 3D $MoS_2/TiO_2/p$-Si. The fitted equivalent circuit of the Nyquist plot consists of a constant phase element (CPE) and resistances such as series resistance (*R*s), charge transfer resistance from silicon to TiO_2 ($R_{\_Si}$) and charge transfer resistance from TiO_2 to electrolyte through MoS_2 ($R_{\_TiO2}$), as shown inset of Fig. 3.8c. The fitted charge transfer resistances of the photocathodes are listed in Table 3.1, where the charge transfer resistance from silicon to TiO_2 was almost equal for both the photocathodes, 3D $MoS_2/TiO_2/p$-Si and TiO_2/p-Si, which are 45 and 40 Ω cm^2, respectively. However, the charge transfer resistance from TiO_2 to electrolyte through a MoS_2 was found to be quite small compared to the charge transferred resistance from TiO_2 to electrolytes, which were 128 and 634 Ω cm^2 for 3D MoS_2/TiO_2/p-Si and TiO_2/p-Si photocathode, respectively.

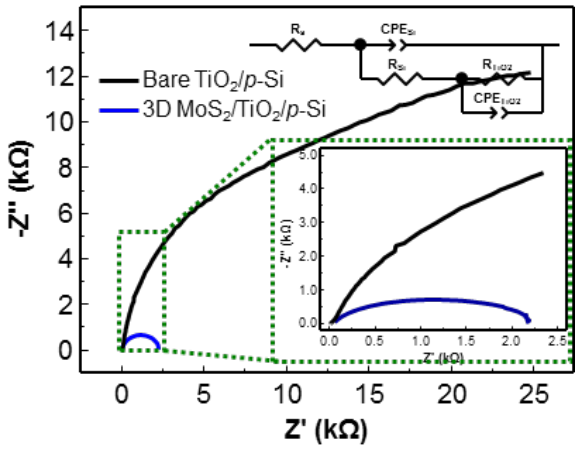

Figure 3.9. Figure 3.8. (a) Nyquist plots of the working electrodes 3D $MoS_2/TiO_2/p$-Si and TiO_2/p-Si, inset is equivalent circuit.

Photocathode	R_{Si} (Ωcm^2)	R_{TiO2} (Ωcm^2)	Appl. volt vs. OCP
TiO_2/p-Si	40.7	4634.4	340 mV
$MoS_2/TiO_2/p$-Si	45.3	128	340mV

Table 3-1. The fitted charge transfer resistance.

The Gibbs free energy of hydrogen adsorption (ΔG_H) on the basal plane and edge sites of MoS_2 was calculated using density functional theory (DFT) to support the experimental results, because Gibbs free energy is considered as a descriptor for HER efficiency (see experimental section for detail of the DFT calculation)[99-102]. The Gibbs free energy of hydrogen adsorption closer to zero indicates the highest catalytic activities of the material for HER[103]. The ΔG_H on the H-Mo edge was considered, because more than half of the 3D MoS_2 surfaces is covered by exposed edges of MoS_2 (Figs. 3.3a and b, 3.6 b–d). For a hydrogen coverage θ_H, 0.5 and 0.25 were considered. Figure 3.7c shows the calculated results of ΔG_H for MoS_2 on the basal plan and Mo edges. On the basal plane of

MoS_2, the ΔG_H was found to be thermodynamically unstable (1.83 eV), indicating that the basal plane is inert for HER. The ΔG_H on the Mo edge sites with 0.5 and 0.25 hydrogen coverage was 0.08 and –0.4 eV, respectively. The obtained ΔG_H values validated the experimental result of EIS and LSV analysis of 3D $MoS_2/TiO_2/p$-Si photocathode.

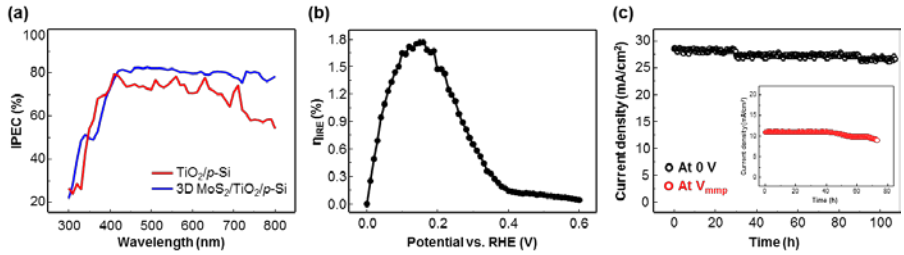

Figure 3.10. Figure 3.9. Efficiency and stability of the photocathode (a) IPCE curves of 3D MoS_2/TiO_2/p-Si and TiO_2/p-Si measured at applied bias voltage of 0.0 V and –0.65 V, respectively. (b) Ideal regenerative cell efficiency of 3D MoS_2/TiO_2/p-Si (c) stability of photocathode,3D $MoS_2/TiO_2/p$-Si at zero vs. RHE bias potential and at the maximum power point potential V_{mpp}.

The incident photon-to-current conversion efficiency (IPCE) of 3D $MoS_2/TiO_2/p$-Si and TiO_2/p-Si samples was measured at a bias voltage of 0.0 and –1.00 V, respectively. The IPCE of the photocathodes are ~85 and 75% for 3D $MoS_2/TiO_2/p$-Si and TiO_2/p-Si, respectively, in the entire visible light spectrum. The ideal regenerative cell efficiency[10] of the 3D $MoS_2/TiO_2/p$-Si photocathode was measured, as shown in Figure 3.9a. The photocathode exhibited V_{mpp} = 0.16 V photovoltage and J_{mpp} = 11.06 mA cm^{-2} current density at the maximum power point. Figure 3.9(b) show the ideal regenerative cell efficiency of the photocathode and was found to be 1.8%. Figure 3.9(c) shows

the measured chronoamperometry of 3D $MoS_2/TiO_2/p$-Si photocathode for an extended time at a bias potential of 0.0 V, and the maximum power point potential (V_{mpp} = 0.16 V) to elucidate the stability of the materials in the electrolyte while generating hydrogen. Therefore, the photocathode is stable for more than 108 h (black color curve) at 0.0 V vs. RHE and ~73 h (red color curve) at the maximum power point bias voltage. The prolonged time stability of 3D $MoS_2/TiO_2/p$-Si photocathode is attributed to the MoS_2 nanostructure that serves as a passivation of the TiO_2/p-Si electrode.

Table 3-2. Summary of the PEC performance of the Photocathode

Photocathode	OP vs. RHE (V)	Saturation J(mA/cm^2)	IPCE %	Reflectance % (Arithmetic mean)	Stability (h)
BareTiO_2/p-Si	– 0.41	32	~70	37	
2D $MoS_2/TiO_2/p$-Si	0.25	33	-		
3D $MoS_2/TiO_2/p$-Si	0.35	37	~85	22	107

3.5. Conclusion

In this chapter an efficient TiO_2 coated 4-inch *p*-Si photocathode with a directly grown 3D MoS_2 HER catalyst was demonstrated. The photoelectrochemical performance of the photocathode for a 3D $MoS_2/TiO_2/p$-Si exhibited the onset potential of 0.35 V with the short circuit current density J_{sc} = 28 mA cm^{-2} and the saturated current density of 37 mA cm^{-2}; for the layered $MoS_2/TiO_2/p$-Si photocathode, the onset potential was 0.2 V at a J_{sc} = 10 mA cm^{-2} and a saturated current density of 33 mA cm^{-2}. The onset potential of the 3D $MoS_2/TiO_2/p$-Si photocathode shifted anodically by 0.76 V relative to the onset potential of the pristine TiO_2/p-Si photocathode. Passivation of the TiO_2/p-Si photocathodes with the MoS_2 layers secured the stable operation for ~181 h without noticeable degradation. The obtained high anodic shift in the 3D $MoS_2/TiO_2/p$-Si photocathode is attributed the high density of exposed edge sites and grain boundaries. The enhanced saturation current of the photocathode resulted from the decrease in optical reflectance. This study paves a way of developing highly efficient and stable water splitting photocathodes using earth-abundant catalysts.

3.6. Reference

1 Stanislaus, A. & Cooper, B. H. Aromatic hydrogenation catalysis: a review. *Catalysis Reviews—Science and Engineering* **36**, 75-123 (1994).

2 Kalikhman, V. & Umanskiĭ, Y. S. Transition-metal chalcogenides with layer structures and features of the filling of their Brillouin zones. *Soviet Physics Uspekhi* **15**, 728 (1973).

3 Brandt, K. Historical development of secondary lithium batteries. *Solid State Ionics* **69**, 173-183 (1994).

4 Auborn, J., Barberio, Y., Hanson, K., Schleich, D. & Martin, M. Amorphous molybdenum sulfide electrodes for nonaqueous electrochemical cells. *Journal of The Electrochemical Society* **134**, 580-586 (1987).

5 Wang, Q. H., Kalantar-Zadeh, K., Kis, A., Coleman, J. N. & Strano, M. S. Electronics and optoelectronics of two-dimensional transition metal dichalcogenides. *Nature nanotechnology* **7**, 699-712 (2012).

6 Ding, Q. *et al.* Efficient photoelectrochemical hydrogen generation using heterostructures of Si and chemically exfoliated metallic MoS2. *Journal of the American Chemical Society* **136**, 8504-8507 (2014).

7 Laursen, A. B., Kegnæs, S., Dahl, S. & Chorkendorff, I. Molybdenum sulfides—efficient and viable materials for electro-and photoelectrocatalytic hydrogen evolution. *Energy & Environmental Science* **5**, 5577-5591 (2012).

8 Hinnemann, B. *et al.* Biomimetic hydrogen evolution: MoS2 nanoparticles as catalyst for hydrogen evolution. *Journal of the American Chemical Society* **127**, 5308-5309 (2005).

9 Wang, Z. M. *MoS2*. (Springer, 2013).

10 Zhao, W. *et al.* Origin of indirect optical transitions in few-layer MoS2, WS2, and WSe2. *Nano letters* **13**, 5627-5634 (2013).

11 Li, G. *et al.* All The Catalytic Active Sites of MoS2 for Hydrogen Evolution. *Journal of the American Chemical Society* (2016).

12 Chung, D. Y. *et al.* Edge-exposed MoS 2 nano-assembled structures as efficient electrocatalysts for hydrogen evolution reaction. *Nanoscale* **6**, 2131-2136 (2014).

13 Haas, A. The Chemistry of Silicon-Sulfur Compounds. *Angewandte Chemie International Edition in English* **4**, 1014-1023 (1965).

14 Chhowalla, M. *et al.* The chemistry of two-dimensional layered transition metal dichalcogenide nanosheets. *Nature chemistry* **5**, 263-275 (2013).

15 Kwon, K. C. *et al.* Wafer-scale transferable molybdenum disulfide thin-film catalysts for photoelectrochemical hydrogen production. *Energy & Environmental Science* (2016).

16 Lin, Z. *et al.* Controllable Growth of Large–Size Crystalline MoS2 and Resist-Free Transfer Assisted with a Cu Thin Film. *Scientific reports* **5** (2015).

17 Ma, D. *et al.* A universal etching-free transfer of MoS2 films for applications in photodetectors. *Nano Research* **8**, 3662-3672 (2015).

18 Lu, Z. *et al.* Universal Transfer and Stacking of Chemical Vapor Deposition-Grown Two-Dimensional Atomic Layers with Water-Soluble Polymer Mediator. *ACS nano* (2016).

19 Kresse, G. & Joubert, D. From ultrasoft pseudopotentials to the projector augmented-wave method. *Physical Review B* **59**, 1758 (1999).

20 Kresse, G. & Furthmüller, J. Efficiency of ab-initio total energy calculations for metals and semiconductors using a plane-wave basis set. *Computational Materials Science* **6**, 15-50 (1996).

21 Kresse, G. & Furthmüller, J. Efficient iterative schemes for ab initio total-energy calculations using a plane-wave basis set. *Physical review B* **54**, 11169 (1996).

22 Perdew, J. P., Burke, K. & Ernzerhof, M. Generalized gradient approximation made simple. *Physical review letters* **77**, 3865 (1996).

23 Perdew, J. P., Ernzerhof, M. & Burke, K. Rationale for mixing exact exchange with density functional approximations. *The Journal of Chemical Physics* **105**, 9982-9985 (1996).

24 Grimme, S. Semiempirical GGA-type density functional constructed with a long-range dispersion correction. *Journal of computational chemistry* **27**, 1787-1799 (2006).

25 Bollinger, M., Jacobsen, K. W. & Nørskov, J. K. Atomic and electronic structure of MoS 2 nanoparticles. *Physical Review B* **67**, 085410 (2003).

26 Zhan, Y., Liu, Z., Najmaei, S., Ajayan, P. M. & Lou, J. Large-area vapor-phase growth and characterization of MoS2 atomic layers on a SiO2 substrate. *Small* **8**, 966-971 (2012).

27 Li, H. *et al.* From bulk to monolayer MoS2: evolution of Raman scattering. *Advanced Functional Materials* **22**, 1385-1390 (2012).

28 Kong, D. *et al.* Synthesis of MoS2 and MoSe2 films with vertically aligned layers. *Nano letters* **13**, 1341-1347 (2013).

29 Aspnes, D. & Studna, A. Dielectric functions and optical parameters of si, ge, gap, gaas, gasb, inp, inas, and insb from 1.5 to 6.0 ev. *Physical review B* **27**, 985 (1983).

30 DeVore, J. R. Refractive indices of rutile and sphalerite. *JOSA* **41**, 416-419 (1951).

31 Pandey, K. *et al.* First step to investigate nature of electronic states and transport in flower-like MoS2: Combining experimental studies with computational calculations. *Scientific Reports* **6** (2016).

32 Fanni, L. *et al.* Tuning the porosity of zinc oxide electrodes: from dense to nanopillar films. *Materials Research Express* **2**, 075006 (2015).

33 Lin, G.-J. *et al.* A broadband and omnidirectional light-harvesting scheme employing nanospheres on Si solar cells. *Nano Energy* **6**, 36-43 (2014).

34 Laursen, A. B. *et al.* MoS 2—an integrated protective and active layer on n+ p-Si for solar H 2 evolution. *Physical Chemistry Chemical Physics* **15**, 20000-20004 (2013).

35 Seger, B. *et al.* Hydrogen production using a molybdenum sulfide catalyst on a titanium-protected n+ p-silicon photocathode. *Angewandte Chemie International Edition* **51**, 9128-9131 (2012).

36 Parsons, R. The rate of electrolytic hydrogen evolution and the heat of adsorption of hydrogen. *Transactions of the Faraday Society* **54**, 1053-1063 (1958).

37 Trasatti, S. Work function, electronegativity, and electrochemical behaviour of metals: II. Potentials of zero charge and “electrochemical” work functions. *Journal of Electroanalytical Chemistry and Interfacial Electrochemistry* **33**, 351-378 (1971).

38 Nørskov, J. K. *et al.* Trends in the exchange current for hydrogen evolution. *Journal of The Electrochemical Society* **152**, J23-J26 (2005).

39 Greeley, J., Jaramillo, T. F., Bonde, J., Chorkendorff, I. & Nørskov, J. K. Computational high-throughput screening of electrocatalytic materials for hydrogen evolution. *Nature materials* **5**, 909-913 (2006).

40 Li, H. *et al.* Activating and optimizing MoS2 basal planes for hydrogen evolution through the formation of strained sulphur vacancies. *Nature materials* **15**, 48-53 (2016).

41 Coridan, R. H. *et al.* Methods for comparing the performance of energy-conversion systems for use in solar fuels and solar electricity generation. *Energy & Environmental Science* **8**, 2886-2901 (2015).

3.7. Appendix: Several cases of edge exposed MoS_2

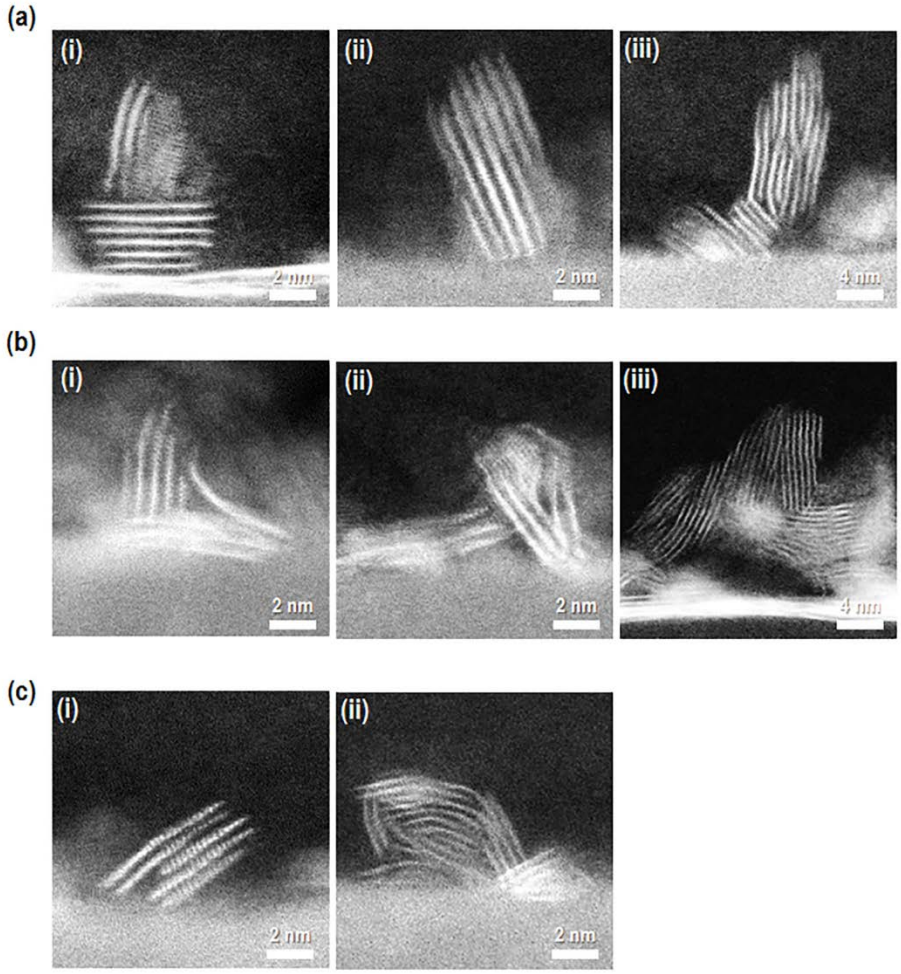

Figure A3.1. (a) Free-standing vertical films (b) edge exposed MoS_2 formed by head-on collision of in-planar crystals (**c)** Defective crystals with edge dislocation and bending

Chapter 4

Dual heteroatom-doping of titanium dioxide nanorods with sulfur and nitrogen for PEC water oxidation

4.1. Introduction

Titanium dioxide is one of the most researched semiconductors for solar energy conversion devices, including solar water splitting (SWS). [1, 2, 3] Although efforts have been made to tune the optical and electronic properties of TiO_2 in order to enhance the charge generation, transport and transfer efficiency without suppressing the photochemical stability, TiO_2 is yet at the rear position in the race of n-type semiconductors for solar water splitting due to a little improvement in the aforementioned drawbacks of TiO_2.[4, 5] Various routes and mechanisms have been developed to adjust the optical and electronic properties of TiO_2 for efficient photoelectrochemical solar water oxidation. [4, 6] For example, thermal treatment of TiO_2 under high oxygen deficient environment results in oxygen vacancies in the structure of TiO_2 and form shallow donors of which energy levels are near to the conduction band of TiO_2. The intentionally introduced impurity energy states can tune the optical properties of TiO_2 nanostructure and show a red shift in the optical absorption that enhances the charge generation efficiency of the photoanode.[7, 8] Similarly, doping of anions such as N,[9-13] C,[14] S,[15, 16] or cations e.g. Cu,[11] Nb,[17] W,[18] Fe, [19] Co,[20] Cr,[21] Mn,[22] and surface coating with precious metals,[23] improve the optical and electrical properties that enhance the photoelectrochemical performances of TiO_2. Furthermore, the codoping of TiO_2 photoanode with both anions and cations, for example, carbon and tungsten, has shown improved photoelectrochemical (PEC) water oxidation performance. The resulted

photoelectrochemical performances are mostly attributed to the enhancement of the photogenerated carriers transport and transfer efficiency of TiO_2. [18] However, a considerable enhancement of the photocurrent density at the 1.23 V vs. RHE was not observed from cocatalyst-free TiO_2 photoanodes due to the high surface and bulk recombination of photogenerated carriers, low photogenerated carrier separation and collection. [18, 24]

The theoretical calculation and experimental studies have shown that the codoping of TiO_2 photoanodes with anions such as sulfur and nitrogen can tune the optical and electrical properties of TiO_2 imposing new dopant energy states near to the top of the valance band, [24-26] as shown in Figure4.1 (a). The optical band gap narrowing of codoped TiO_2 could be due to the mixing of the partially filled N 2*p* states and S 3*p* states with the O 2*p* states.[27] The partially filled states introduced by the nitrogen dopants may serve as recombination centers and affect the performance of the doped photoanode. However, the overall solar-to-hydrogen conversion efficiency of the doped TiO_2 can be better than the undoped TiO_2 due to the higher carrier generation rate than the recombination rate.[28] Sulfur can have several different charge states in the TiO_2 such as S^{-2}, S^{4+}, and S^{6+}: the most probable anionic sulfur (S^{-2}) when the sulfur atom substitutes the oxygen atom, the cationic sulfur (S^{4+}) when the titanium atom of TiO_2 is substituted by the sulfur atom, and the cationic sulfur (S^{6+}) when the formation of pyrosulfate occurs.[29] Both the anionic and cationic sulfur states serve as e^-/h^+ shallow trap sites that promote the catalytic activities of TiO_2 and reduce the recombination rate of photogenerated carriers.[30] Figure 4.1(b) shows a schematic for the adsorption of hydroxide ions (i) on the

titanium and (ii) sulfur atoms at the surface of TiO_2 in the alkaline solution. Proton can transfer from the photoanode to the hydroxide ion with the lower activation energy for TiO_2 doped with sulfur than pristine TiO_2, as shown in Figure 4.1(b) (iii), since the sulfur dopant can act as an effective adsorption site for the hydroxide ion in TiO_2.[26] Therefore, the UV absorption edge of codoped TiO_2 could be shifted toward the visible light wavelength due to the induced impurity levels, and the amount of collected photogenerated carriers could increase due to sulfur ions in codoped TiO_2, which minimizes the recombination rate of photogenerated carriers. Thus, it can result in the enhancement of PEC water oxidation performance of codoped TiO_2 photoanode. However, there is no or limited experimental study to verify the effects of nitrogen and sulfur codoping on the performance of TiO_2 nanorods (NRs) for photoelectrochemical solar water splitting.

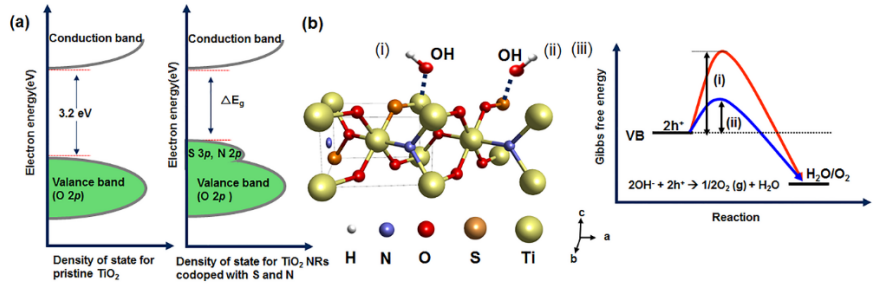

Figure 4.1. Effects of dual heteroatom-doped in the TiO_2. Schematic illustration of density of state for (a) pristine TiO_2 (b) codoped TiO_2 with sulfur and nitrogen

Various methods can be used to synthesize TiO_2 NRs, such as hydrothermal with ex situ and/or in situ codoping of sulfur and nitrogen, electron beam deposition, chemical vapor deposition with ex situ codoping of nitrogen and

sulfur, anodization, and others. [31] However, the hydrothermal synthesis methods could be preferred over other methods for the codoping of anions in the TiO_2 due to low coast and flexibility of the method to use precursor and codoping mechanism. It also enable to synthesize different morphology of nanostructure TiO_2 (see appendix 4).

4.3. Experimental

4.3.1. Synthesis of codoped TiO_2 NRs on FTO/glass and photoanode preparation

The codoped TiO_2 NRs have grown on the FTO/glass using hydrothermal synthesis method with precursors *DI-water*, *HCl* and *tetrabutyl titanate* solutions with the amount of 25 ml and 25 ml, 0.8 ml, respectively. [39] Different amounts of *sulfamic acid* from 5 mg to 15 mg as a source of nitrogen and sulfur were added. The precursors were added sequentially as follows: *DI-water*, *HCl*, *sulfamic acid* and *tetrabutyl titanate* to a glass beaker and stirred vigorously using magnetic stirrer until the cloudy color changed to colorless as shown in Figure 4.2(a). Subsequently, the solutions were transferred to a teflon beaker (100 ml) in which the FTO/glass was placed at the bottom keeping the active side faced up as shown in Figure 4.2(b). The teflon beaker which had the precursor solution and the substrate, FTO/glass, was inserted into the autoclave and sealed properly as shown in Figure 4.2(c). Subsequently it was cooked for four hours at 180°C in an oven and kept inside until the temperature reached room temperature as

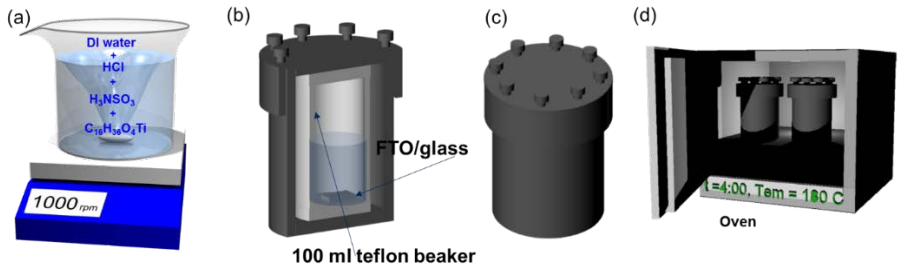

Figure 4.2. Schematics of the hydrothermal synthesis set-ups in sequence. (a) Precursor addition and mixing. (b) FTO/glass substrate inside the Teflon. (c) Tightly sealed autoclave that contains the Teflon which had the precursors and the substrate. (d) Autoclave loaded oven.

Shown Figure 4.2(d). The synthesized codoped sample was removed from the teflon and rinsed repeatedly using DI-water and subsequently annealed at a temperature of 350°C for half an hour in the ambient air. The temperature for annealing was ramped up at the rate of 5°C/minute until it reached the final temperature of, 350°C. The sample was kept inside the furnace until the annealing temperature reached 140°C and then was removed from the furnace.

Four different TiO_2 NRs photoanodes with different amounts of sulfur and nitrogen precursor were prepared to identify the optimum codopant concentration and designated them as: sample one (pristine) a 0.0 mg, sample two (SN1) a 5 mg, sample three (SN2) a 10 mg, and sample four (SN3) a 15 mg of H_3NSO_3 amount of codopant precursor was added. The color of synthesized TiO_2 NRs samples changed from dull white to light yellow while the amount of codopant precursor was increased, as shown in Figure 4.3 (a). Afterwards, all the TiO_2 (S, N) NRs using a blade from the FTO/glass substrate except ~10.0 mm^2 area were removed. A copper wire was connected using

silver past to the conductive side of FTO/glass for the collection of majority charge carriers. The conductive part of the photoanodes except the tail of the copper wire and a 9.74 mm^2 photoactive part, i.e., the area that was exposed to the electrolyte, repeatedly covered by transparent nail polish. To cure the TiO_2 (N, S) NRs photoanodes which were covered with nail polish are kept in the ambient air for a couple of hours, then the photoanodes become ready for PEC measurement as shown in Figure 4.3(b).

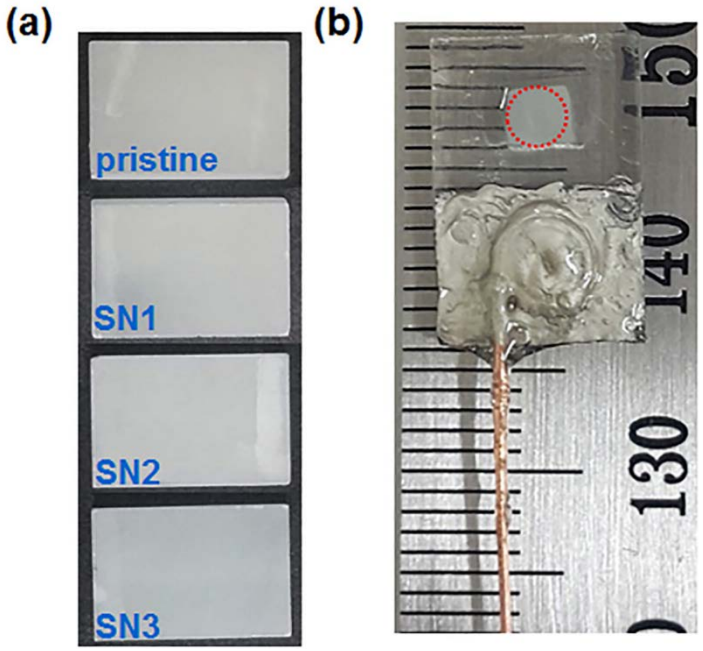

Figure 4.3. (a) Optical image of synthesized TiO2 NRs/FTO glass codoped with different concentration sulfur and nitrogen. (d) Optical image of the prepared photoanode.

4.4. Characterization

4.4.1. Physical Characterization

The morphology of the synthesized pristine and codoped TiO_2 NRs were investigated using field emission scanning electron microscopy (FESEM: MERLIN compact, JEOL). The phase crystallinity of both pristine and codoped TiO_2 NRs was observed with high-resolution transmission electron microscopy (JEM-2100F, JEOL) and X-ray diffractometer (Bruker Miller Co., D8-Advance). The codopant distribution and elemental mapping were analyzed with high resolution X-ray photoelectron spectroscopy (Kratos AXIS-His) and scanning transmission electron microscope coupled with energy dispersive X-ray spectroscopy (JEM-2100F, JEOL). To measure EDS line scan, thick TiO_2 (S, N) NRs were synthesized [37] and a nanorod was cut in an arbitrary position to obtain the distribution of sulfur and nitrogen in the bulk and at the surface of TiO_2 NRs. The EDS line scan data of TiO_2 (S, N) NRs were obtained from the cross section of the cut nanorod and the EDS line scan was measured by FESEM. To identify the consequences of codopant, nitrogen and sulfur, in the optical properties of TiO_2 NRs, a UV-visible absorption spectra were measured with wavelengths ranging from 300 nm to 800 nm. To measure the electrical properties of the synthesized samples a shadow mask with a hole diameter of 200 µm was taped on the top of the samples and subsequently a silver metal contact was deposited using an electron-beam evaporator (KVE-E2004L) at the surface of the masked samples as shown in Figure 4.9 (a) inset. The current-voltage measurements were conducted at room temperature using a probe

station with two probe tips. Afterwards, the conductance of pristine and codoped TiO_2 NRs samples were calculated.

4.4.2. Photoelectrochemical measurement

The photoelectrochemical properties of both pristine and codoped TiO_2 NRs were measured using computer controlled potentiostat (IVIUM Technologies, nSTAT). All the PEC measurement were performed with NaOH electrolyte (pH = 13.6), single compartment cuvette and three electrodes configuration such as, the prepared photoanode, Ag/AgCl electrode and graphite rod were used as working, reference and counter electrode respectively. A Xe arc lamp was used as a light source and calibrated to 100 $mWcm^{-2}$ using a standard silicon photodiode at the sample location. In all of the linear sweep voltammograms measurements, the photoanodes were anodically polarized at the scan rate of 20mV/sec during both illumination and in the dark measurement. The measured potential V vs. Ag/AgCl were converted to reference hydrogen electrode (RHE) using the following Equation 4.1,

$$V_{RHE} = E + E_{Ag/AgCl} + 0.059 \times pH \text{ ----- (4.1)}$$

where E is applied potential vs. Ag/AgCl and $E_{Ag/AgCl}$ is 0.21 V vs RHE and V_{RHE} is the applied potential vs. RHE.

The IPCE, which is equivalent to external quantum efficiency, of the samples was measured at applied bias potential of 0.23 V vs. Ag/AgCl using computer controlled monochromator (MonoRa150) and an amplifier for photocurrent detection. The electrochemical impedance spectroscopy (EIS) was measured at 0.23 V vs. Ag/AgCl with respect to open circuit potential (OCP) and sweeping

in the frequency range of 350 K Hz – 0.1Hz with an AC amplitude of 10 mV. The EIS Nyquist curves were fitted to equivalent circuit using Zplot 2x software. To obtain the carrier concentration of the synthesized TiO_2 NRs, Mott-Schottky (M-S) measurements were performed at frequency of 1 kHz with a sweeping bias potential of 0.0 V- 0.8 V vs Ag/AgCl using the same electrodes and electrolyte presented somewhere above. The carrier density was calculated using the M-S Equation 2,

$$\frac{1}{C_{sc}^2} = \frac{1}{\varepsilon_r \varepsilon_o A^2 e N_D}\left(E - E_{fb} - \frac{KT}{e}\right) \text{----- (4.2)}$$

where C_{sc} space charge layer of the sample, ε_r relative permittivity of the sample, ε_{r_TiO2} is 170, [8], ε_o permittivity of free space, A is active surface area of the measured sample, e is an elementary charge, N_D is carrier density of the measured photoanode, E is applied potential, E_{fb} is flat band potential of the measured material, K and T are Boltzmann constant and temperature, respectively.

The applied bias photon-to-current conversion efficncy (ABPE) measurement was performed using two electrodes, the prepared photoanode and platinum wire without any sacrificial donor/acceptor and single compartment cuvette. The bias potential (V_b) was applied between the working electrode and the counter electrode (Pt wire). The resulting ABPE value were obtained using the following Equation 4.3,

$$\mathrm{ABPE} = \left(\frac{|\mathrm{J}(\mathrm{mAcm^{-2}})|\times(1.23-|\mathrm{V_b}|)(\mathrm{V})}{\mathrm{I}(\mathrm{mWcm^{-2}})}\right)\times 100\% \text{ ----- (4.3)}$$

Where J is the photocurrent density, I the incident illumination intensity ($100 mWcm^{-2}$) and V_b the bias potential, 1.23 V is a thermodynamic water splitting potential.

4.4.3. Theoretical Calculation

Vienna Ab initio Simulation Package (VASP)[40] with PAW potentials is used for the density functional theory (DFT) calculations. We employ the generalized gradient approximation (GGA) for the exchange-correlation functional. The energy cutoff of the plane-wave basis set to 400 eV and the 3×3×4 Monkhorst-pack **k**-point sampling is used for primitive cell of rutile TiO_2. For the defect calculation, we use 144-atom supercell with Γ-only **k**-point which corresponds to same **k**-point density compared to primitive cell. The dopant formation energy is calculated using following Equation 4.4,

$$E_{\mathrm{For}}(\mathrm{doped},q) = E_{\mathrm{tot}}(\mathrm{doped},q) - E_{\mathrm{tot}}(\mathrm{perfect}) + \sum N_i\mu_i + q(\varepsilon_{\mathrm{F}} + \varepsilon_{\mathrm{VBM}}) + E_{\mathrm{corr}}, \text{ --- (4.4)}$$

where E_{For} is the formation energy of dopant, E_{tot} is the total free energy of supercell, q is the charge state, N_i and μ_i are the number and chemical potential of the chemical species i, and ε_F is the Fermi energy with respect to the valence band maximum energy (ε_{VBM}). E_{corr} is the correction energy to remove spurious electrostatic interactions among image charges in the repeated cells. For E_{corr}, we use FNV correction considering the anisotropic dielectric constant.[41,42] We use conventional DFT calculation for the calculation of defect formation energies, and for absorption coefficient calculation, we use HSE06 hybrid functional with 0.25 of the fraction of Fock exchange which result in the band

gap of 3.16 eV. We use the 2×2×2 Monkhorst-pack **k**-point and large number of unoccupied bands for the calculation of optical property to obtain well-converged result.

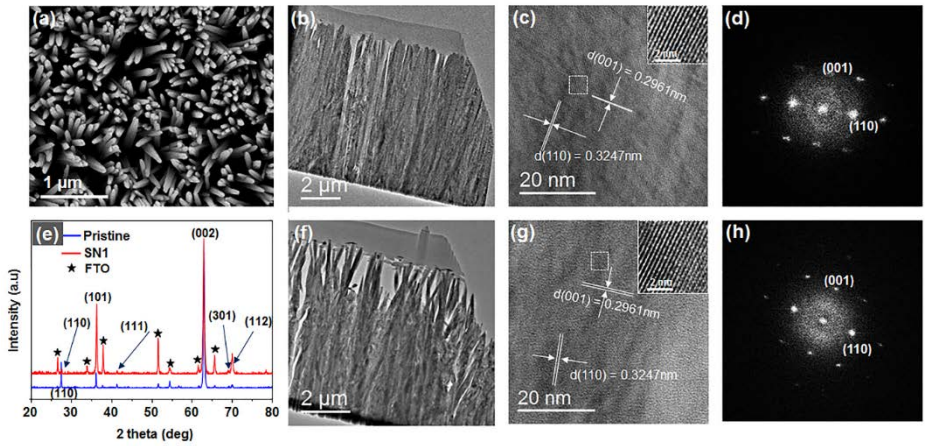

Figure 4.4. SEM and TEM images of codoped and pristine TiO2 NRs, and the corresponding XRD analysis. (a) Planar view SEM image. (b) Cross-sectional TEM image for pristine TiO_2 NRs. (c) High resolution TEM image for a pristine TiO2 NR. The inset is a magnified image for the selected region. (d) Selected area diffraction pattern of the pristine TiO_2 NR. (e) XRD spectra of pristine TiO_2 NRs (blue curve) and codoped TiO_2 NRs (red line). (f) Cross-sectional TEM image of codoped TiO_2 NR. (g) High resolution TEM image of a codoped TiO_2 NR. The inset is a magnified image for the selected region. (h) Selected area diffraction pattern of the codoped TiO_2 NRs.

4.5. Result and discussion

The optical image of the synthesized samples with different sulfur and nitrogen amount (see method section for detail), such as pristine, SN1, SN2 and SN3 are shown in Figure 4.3(a). The color of synthesized TiO_2 NRs samples

changed from dull white to light yellow while the amount of codopant precursor has increased. Figure 4.3 shows the photoanode with the active area encircled by the red dotted line, and the details preparation of the photoanode is presented in the method section. The synthesized pristine TiO_2 NRs and in-situ codoped TiO_2 NRs with nitrogen and sulfur have high aspect ratios (length/diameter), i.e. an average length of 6.7 µm and 150 nm diameter as revealed through scanning electron microscopy (SEM) and

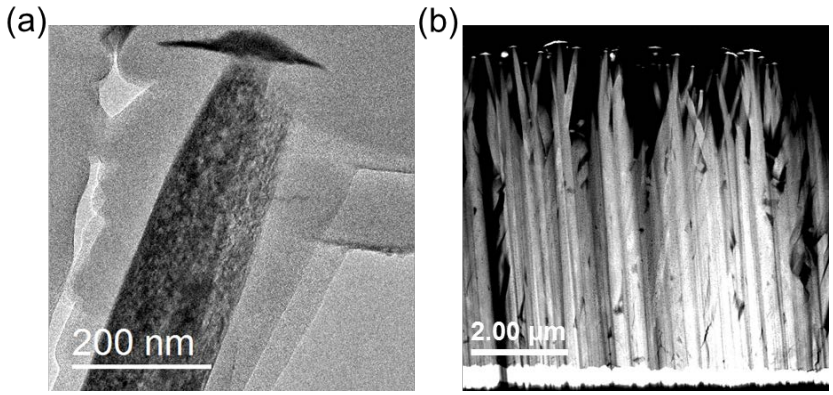

Figure 4.5. The morphology of the synthesized TiO_2 NRs. (a) TEM image of single TiO_2 NR. (b) STEM image of TiO_2 NRs.

Transmission electron microscopy (TEM) as shown in Figure 4.4 and Figure 4.5. The high aspect ratio (length/diameter) nanorods have better optical absorption and short photogenerated carrier diffusion length than planar TiO_2 [32]. TEM and selected area electron diffraction patterns (SAED) measurement reveals that the crystalline phase and the lattice parameter of both pristine and codoped TiO_2 NRs do not show any noticeable difference. It was found that both pristine and codoped TiO_2 NRs are a rutile phase. The lattice plane of {110} and {100} for both pristine and codoped TiO_2 NRs were clearly visible

and the plane spacing parameter d was calculated for both samples. The lattice spacing d_{ijk} are found to be d_{100} = 0.296 nm and d_{110} = 0.325 nm for (100) and (110) planes, respectively, as shown in Figure 4.4(c) and (g). The possible reason for both samples having indistinguishable crystalline phase and lattice parameter may be the low codopant concentration and the negligible atomic radius difference between the codopant and oxygen in the TiO_2 NRs. [9]

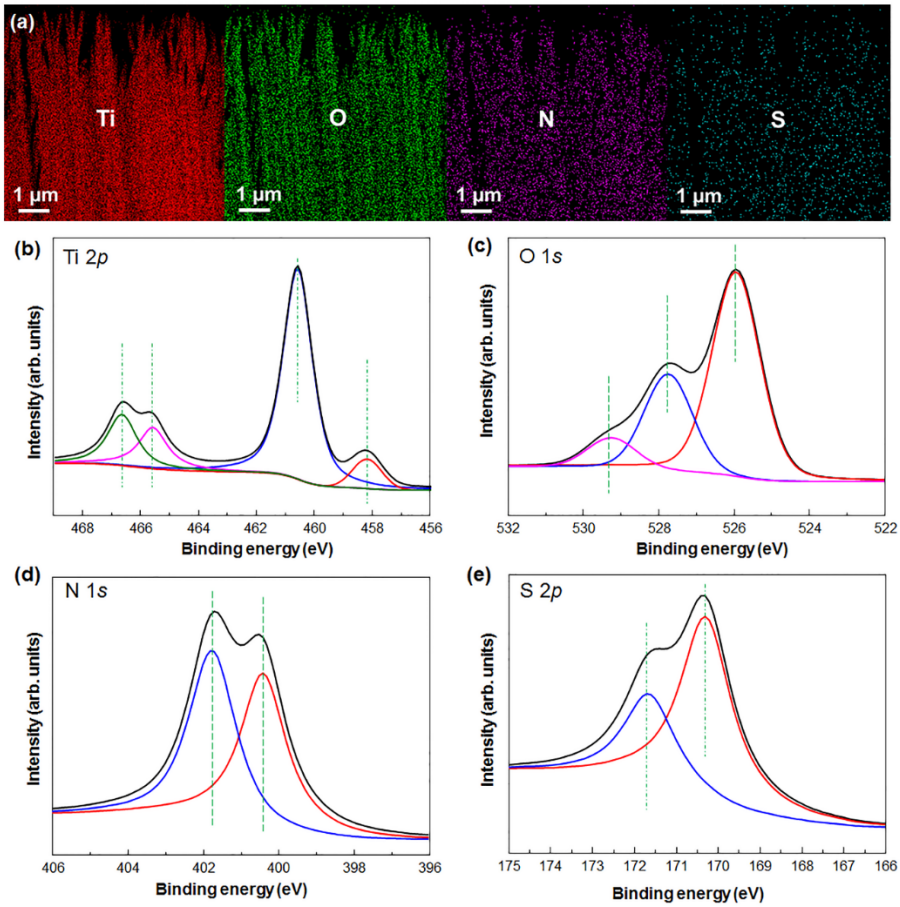

Figure 4.6. EDS and high resolution XPS analysis. (a) Elemental mapping for titanium, oxygen, nitrogen, and sulfur in the synthesized TiO_2 NRs by using STEM. (b)- (e) XPS analysis for Ti 2*p*, O 1*s*, N 1*s*, and S 2*p*, respectively.

Crystallinity and growth habit analysis of the synthesized pristine and codoped TiO_2 NRs was conducted using X-ray diffraction measurement. All samples were found to be a rutile structure of TiO_2 (as confirmed by TEM analysis) with different lattice plane peak intensities, i.e., (002) > (101) > (110) as shown in Figure 4.4(e). The intensity difference suggested that the preferable growth direction could be [001] for both pristine and codoped TiO_2 NRs. Moreover, the intensity of (110) facet for codoped TiO_2 NRs is smaller than the intensity of (101) facet while the intensity of (110) facet for pristine TiO_2 NRs is greater than the intensity of (101) facet. The reason could be that the codopant in the TiO_2 NRs can exist in that facet and discourage the growth of (110) facet while motivating the growth of (101) facet. Scanning TEM (STEM) and field emission SEM (FESEM) equipped with energy dispersive spectroscopy (EDS) reveal that nitrogen and sulfur dopants are uniformly distributed in the entire TiO_2 NRs, as shown in Figures 4.6 (a) and 4.7. The concentration of oxygen in the codoped TiO_2 NRs sample is slightly lower than that of pristine TiO_2 NRs. The observed low oxygen amount in the codoped TiO_2 NRs could be a result of anion dopants, nitrogen and sulfur, which could substitute the oxygen atom in the TiO_2 NRs. [13]

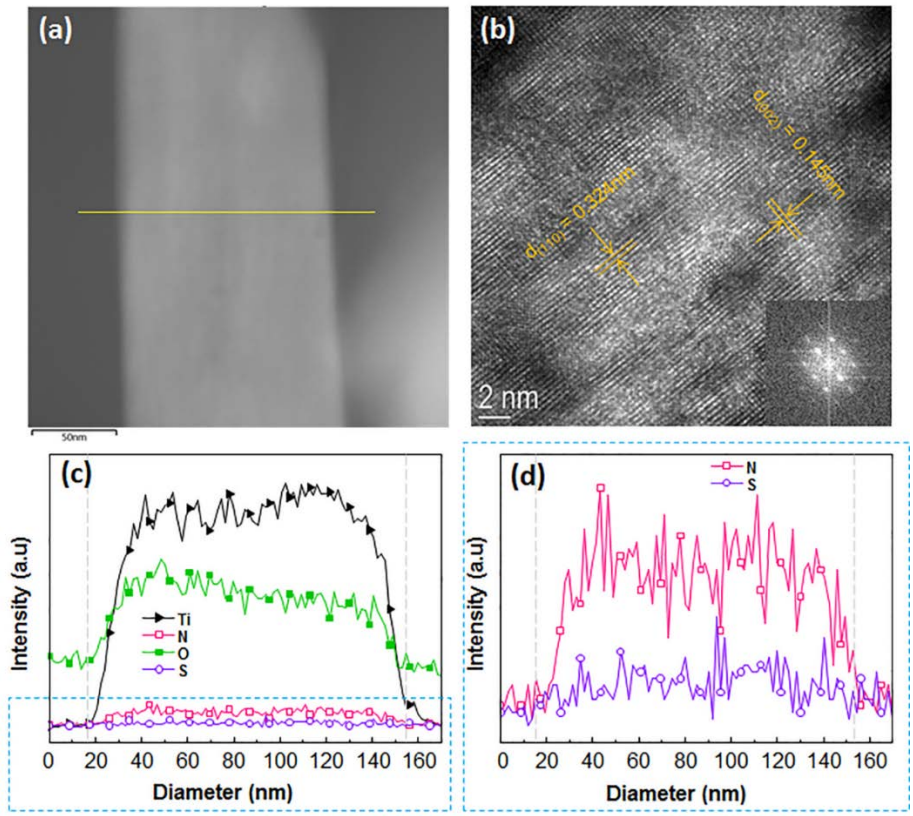

Figure 4.7. (a) TEM image of single TiO_2 (S, N) NRs from SN1 specimens (b) The corresponding HRTEM image, (c)-(d) EDS analysis of Ti, O, N and S profiles

To unveil the chemical states of the codopant (nitrogen and sulfur) in the TiO_2 NRs, high-resolution X-ray photoelectron spectroscopy (XPS) measurements were conducted as shown in Figure 4.6 (b)-(e). The deconvolution of the spectra shows that nitrogen has two peaks in the synthesized TiO_2 NRs at the binding energy of 402 eV and 400.5 eV. The two N 1*s* peaks arise from a Ti^{+3} and N-O bond due to the substitution of nitrogen for oxygen (N_O) and existence of nitrogen atom in the interstitial sites, respectively. The interstitial nitrogen dopant that forms a deeply localized energy state in TiO_2 may serve as a

potential recombination site for photogenerated carriers, while the substitutional nitrogen dopant exists at the shallow energy states near to the valance band of TiO_2.[11] Likewise, the S 2*p* spectrum has two peaks at 170 eV and 172 eV of binding energy; these two peaks may attributed to the oxidation states of S^{4+} and S^{2-} for S atom in the TiO_2 NRs.[15] The anionic sulfur peak reveals that oxygen atom is substituted by sulfur atom (S_O) and the cationic sulfur peak suggests the substitution of titanium atom with sulfur atom (S_{Ti}).

The PEC performance of pristine and codoped TiO_2 NRs was measured and the LSV curves of all samples are presented in Figure 4.8 (a). It is known that the pristine TiO_2 NRs show low current density at 1.23 V vs RHE due to no absorption in the visible light wavelength, low charge transfer and transport properties.[10, 33] Similarly, our pristine TiO_2 NRs show a 0.7 $mAcm^{-2}$ of current density at 1.23 V vs. RHE as shown in Figure 4.8(a) (purple color). The obtained photocurrent density of pristine TiO_2 NRs is less than the theoretical predicted current density of TiO_2.[34] However, all the codoped photoanodes samples, Figure 4.8a (red, blue and green curves), exhibit an excellent PEC performance for water oxidation with current densities of 2.82 $mAcm^{-2}$, 2.45 $mAcm^{-2}$ and 1.7 $mAcm^{-2}$ at 1.23 V vs. RHE for SN1, SN2, and SN3 photoanodes, respectively. The SN1 photoanode has the highest photocurrent density among of all photoanodes, and more specifically it has four times higher photocurrent density than the pristine TiO_2 NRs photoanode at 1.23 V vs. RHE. The overall performance of TiO_2 (S, N) NRs are higher than nitrogen doped TiO_2. The possible reasons could be (i) the high rate of charge generation due to bandgap narrowing that dominates the recombination rate of photogenerated

carriers and (ii) the fast desorption rate of oxygen and charge generation from the presence of sulfur that can also reduce the influence of recombination. Furthermore, in general, the multi-element doping can offer to manipulate the density of photogenerated carriers and carrier kinetics of the host material. Thus, the high photocurrent density of the codoped TiO_2 NRs has confirmed the effectiveness of codoping sulfur and nitrogen pairs in the TiO_2 to enhance the performance of the photoanode. The chronoamperometry of all samples were measured with chopping light with a time interval of about 0.3 s. While the light source was off the photocurrents in all codoped samples, SN1, SN2 and SN3, were slowly reducing to zero as shown in Figure 4.8 (b).

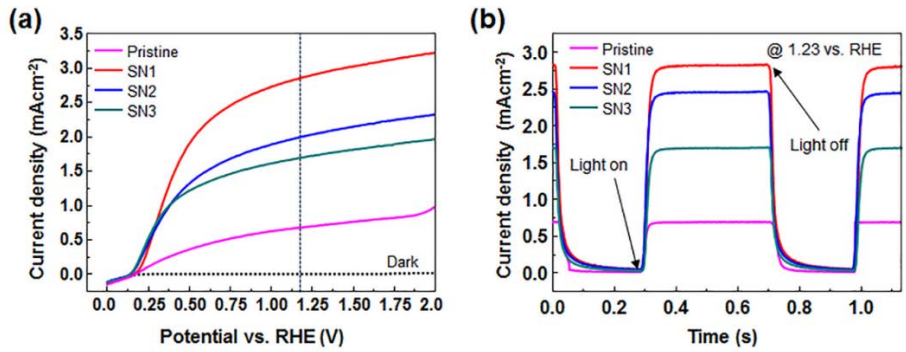

Figure 4.8. (a) Linear sweep voltammograms of pristine and codoped TiO_2 NRs with different doping concentration. (b) The corresponding chronoamperometry of pristine and codoped TiO_2 NRs photoanodes at 1.23 mA cm^{-2}.

It is known that the photocurrent curve behavior in the transient measurement is highly dependent on carrier accumulation and the rate of carrier recombination. Therefore, the slow turnoff of current density in the codoped samples might be attributed to the enhancement of carrier diffusion length.

The electrochemical impedance spectroscopy (EIS) of TiO_2 NRs photoanodes was measured to elucidate the charge transfer in the interface of electrode-electrolyte (R_{TiO2}) and the synthesized TiO_2 NRs-FTO substrate ($R_{TiO2/FTO}$). The corresponding Nyquist plots have shown a single semi-circle which began at the origin as illustrated in Figure 4.9. The fitted equivalent circuit element of the obtained Nyquist data consists of R_s, R_{TiO2}, $R_{TiO2/FTO}$ and constant phase elements (CPE). The corresponding analyzed circuit element values are presented in Table 4.1. Despite the slight variation of Rs value of the photoanodes, i.e., pristine = 17.1 Ωcm^2, SN1 = 12.4 Ωcm^2, SN2 = 13.84 Ωcm^2 and SN3 = 13.8 Ωcm^2, the obtained series resistance (R_s) values confirm that the synthesized photoanodes have excellent photocatalytic performance.

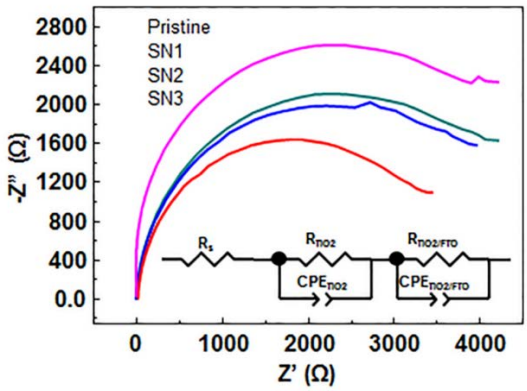

Figure 4.9. Electrochemical impedance Nyquist plots for both pristine and codoped TiO_2 NRs samples and their equivalent circuit.

Moreover, the charge transfer resistance at the electrode-electrolyte interface (R_{TiO2} (Ωcm^2)) of, SN1 = 216.06, SN2 = 362.33, SN3 = 424.7 and TiO_2 NRs - FTO interface ($R_{TiO2/FTO}$ (Ωcm^2)) of, SN1 = 127.9, SN2 = 192.85, SN3 = 229.7,

codoped samples are smaller than the pristine TiO_2 NRs sample (pristine → R_{TiO2} = 676 Ωcm^2 and $R_{TiO2/FTO}$ = 383.63 Ωcm^2).

Table 4-1. Fitted charge transfer and transport resistance

Photoanodes	R_s (Ωcm^2)	R_{TiO2} (Ωcm^2)	$R_{TiO2/FTO}$ (Ωcm^2)
Pristine TiO_2 NRs	17.1	676	383.63
SN1	12.4	216.06	127.9
SN2	13.84	362.33	192.85
SN3	13.8	424.7	229.7

The decrease of charge transfer resistance in the codoped samples indicate that the enhanced photocurrent density values of the codoped samples, specifically in the UV region (wavelength < 400 nm), are partly accredited to the improvement of the carrier transfer efficiency.

The electrical properties of the codoped and pristine TiO_2 NRs were roughly estimated. First a shadow mask with a hole diameter of 200 μm was taped on the top of the samples and subsequently a silver metal contact was deposited using an electron-beam evaporator at the surface of the masked samples. Second the IV measurements were conducted at room temperature using a probe station with two probe tips. Subsiquantly, we calculated the conductance of pristine and codoped TiO_2 NRs samples using the Equations 4.5-4.7 as follows:

$$\rho = R\frac{A}{l} \text{ --- (4.5)}$$

$$R = \frac{V}{I} \text{ --- (4.6)}$$

where ρ is resistivity, R is resistance, A is Area (we used the area of the metal contact), l is the thickness/length of the nanorods, V is the applied voltage and I is the measured current.

$$\sigma = \frac{1}{\rho} \text{ --- (4.7)}$$

Then we calculated the conductance of the TiO_2 NRs samples using equation 4.7 and plotted their conductance value at 1.0 V applied voltage.

The calculated electrical conductance of the TiO_2 NRs was found to be 6.23×10^{-12} Sm^{-1}, 3.9×10^{-8} Sm^{-1}, 2.65×10^{-9} Sm^{-1}, and 2.35×10^{-10} Sm^{-1} for the pristine, SN1, SN2, and SN3 samples, as shown in Figure 4.10 (a). The R_{TiO2} and $R_{TiO2/FTO}$ values of the codoped TiO_2 NRs samples increased while the amount of codopant concentration increased and the conductance of the codoped TiO_2 NRs were decreased when the amount of codopant precursor was increased which could be due to the enhancement of lattice and impurities scattering in the codoped TiO_2 NRs. [35]

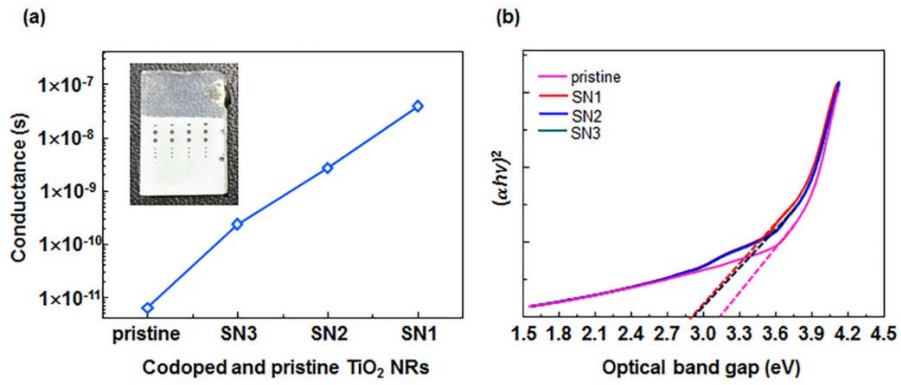

Figure 4.10. (a) The $(ahv)^2$ vs. optical band gap of synthesized TiO_2 NRs. (b) The conductance of pristine and codoped TiO_2 NRs and inset silver metal contact deposited sample.

The optical band gap of the synthesized samples were estimated by using "Tauc plot" using the folowing equation.

$$(\alpha hv)^2 = X(hv - Eg) \text{--- (4.8)}$$

where α is absorbance, h is plank constant, v is frequency of the illuminated light, X is transition probability and E_g is optical band gap. Equation 4.8 can be simplified to the well known constants as e quation 4.9.

$$v = \frac{c}{\lambda} \text{--- (4.9)}$$

where c is the speed of light and λ is the wavelength of illuminated light while absorbance of the synthesized sample was measured. Equation 4.10 was obtained after inserting the well known universal constants and combining equation 4.8 and 4.8.

$$\left(\alpha \frac{1240}{\lambda}\right)^2 = \left(\frac{1240}{\lambda} - Eg\right) \text{--- (4.10)}$$

Therefore, the optical band gap were estimated by extrapolating a straight line at $(\alpha hv)^2 = 0$ to the axis of $(\alpha hv)^2$ versus hv graph.

Therefore, the calculated optical band gap of TiO_2 NRs using a UV visible absorption data and equation 4.10 was 3.1 eV for pristine and 2.88 eV for all codoped TiO_2 NRs samples (SN1, SN2, SN3) as shown in Figure 4.10 (b), which is highly aligned with the estimated band gap using the IPCE onset wavelength. The decrease of the optical band gap of TiO_2 from 3.1 eV to 2. 88 eV for codoped samples attributes to the formation of new defect energy states to the top of valance band of TiO_2 NRs due to the presence of nitrogen and sulfur.

To analyze the ability of the photoanodes to convert the input photons into output electrons, i.e., useful electrons, we measured incident photon-to-current conversion efficiency (IPCE) of the photoanodes at a wavelength of 300 nm to 800 nm at 1.23 V vs. RHE as shown in Figure 4.11 (b). The IPCE values of the photoanodes are 19.1 % at a wavelength of 370 nm, 97.0 % at a wavelength of 360 nm, 75.7 % at a wavelength 350 nm, and 65.1 % at a wavelength of 370 nm for pristine, SN1, SN2, and SN3, respectively.

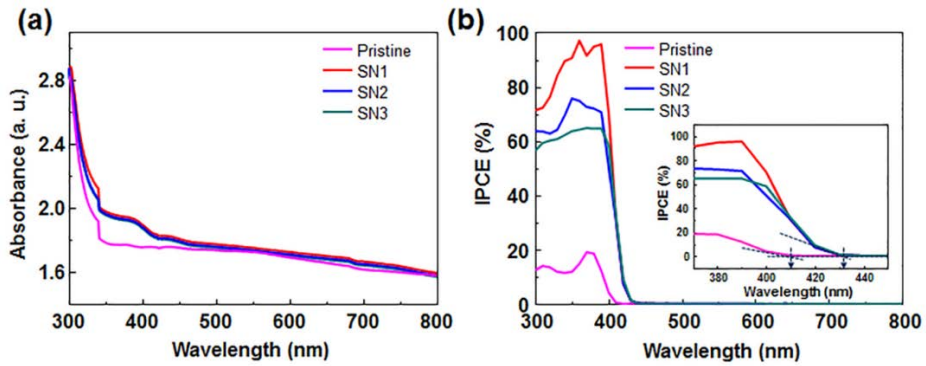

Figure 4.11. Optical absorption spectra of pristine and codoped samples. (e) External quantum efficiency of pristine and codoped TiO_2 NRs.

The IPCE onset wavelength of all the codoped samples, SN1, SN2, and SN3 are ~430 nm, corresponds to the optical band gap of 2.88 eV for codoped samples. The UV visible absorption of all four samples was measured to identify the contribution of the photogenerated charge carriers to the IPCE values of the photoanodes and it was found that the optical absorption of all codoped samples have shown a slight improvement of the entire wavelength of < 450 nm relative to the pristine TiO_2 NRs sample as shown in Figure 4.11 **(b).** It implies that the concentration of photogenerated electron-hole pairs is higher

in the codoped samples, which has a role in the enhancement of IPCE value for the codoped samples.

In comparison with the current densities at 1.23 V vs. RHE of recently reported TiO_2 photoanodes without additional catalysts, in which their performance was improved by doping anions or/and cations, [18, 36] Au decoration, [3] heterojunction. [37] Hydrogen treated, [38] and morphology and surface engineering, [1] and the current density of the codoped TiO_2 (S N) NRs photoanode is plotted in Figure 4.12. The TiO_2 NRs photoanode codoped with nitrogen and sulfur was found to be superior to those photoanodes, particularly the SN1 photoanode has a 11.4 % higher current density (which is indicated by green mark on the dark red bar) at 1.23 V vs. RHE than the hydrogen treated TiO_2 photoanode, [38] which is considered as the best photoanode from co-catalyst free TiO_2 based electrodes that have been reported for PEC water oxidation.

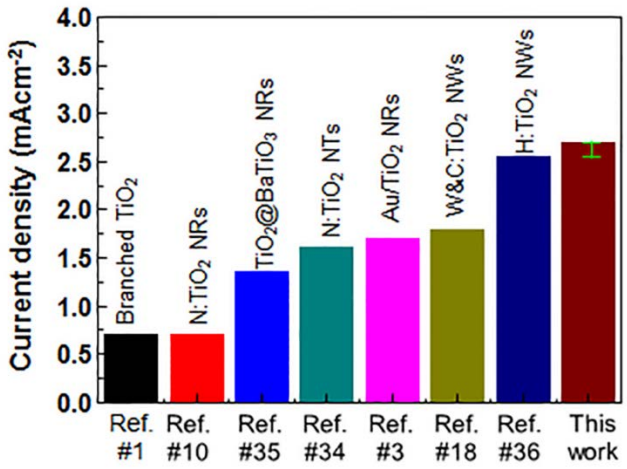

Figure 4.12. Comparing our result with recently published results. The green mark in the dark red bar (our photoanode) indicates the amount of photocurrent difference from the dark blue bar.

The Mott-Schottky (M-S) measurement is performed to determine the effect of codopant in the carrier density of synthesized TiO_2 NRs photoanodes. Consequently, the inverse square of the capacitance of the space charge (C_{sc}) of the nanorod versus electrode potential V for all samples were plotted as shown in Figure 4.13. (a). The slope of M-S plots for all samples are positive and this suggests that the synthesized TiO_2 NRs photoanodes are n-type semiconductor materials. Furthermore, the calculated carrier density of the photoanodes are found to be 8.6×10^{17} cm^{-3}, 6.9×10^{18} cm^{-3}, 5.6×10^{18} cm^{-3} and 3.68×10^{18} cm^{-3} for the pristine, SN1, SN2, and SN3 samples, respectively. The increment of carrier density in the codoped samples could be due to the improvement of charge transfer and transport efficiency of the photoanodes, which is manifested in the enhancement of IPCE in the UV region and chopped light chronoamperometry measurement in which a slow turnoff of current densities

was observed. Another cause for the improvement of carrier density in codoped samples could be the red shift in optical absorption edge from UV (400 nm) to visible region (430 nm) that enhances the charge generation efficiency of the samples. The red shift of optical absorption in the codoped samples occurred due to the formation of new energy state near to the top of the valance band.

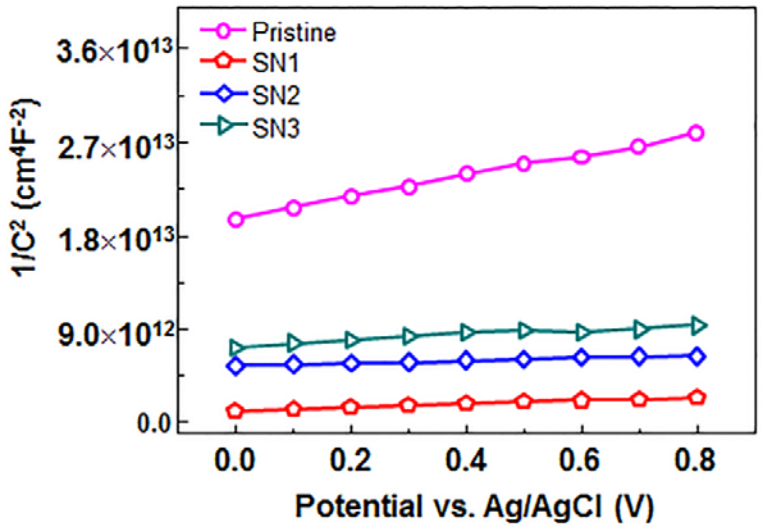

Figure 4.13. Mott-schottky plot for pristine and codoped specimens (SN1, SN2 and SN3)

The applied bias photon-to-current conversion efficiency (ABPE) of the best performing photocathode, SN1, and pristine TiO_2 NRs were measured using the two electrode experiment. The obtained current density using the two electrode experiment is lower than the three electrode experiment as shown in Figure 4.14(a). The decrease in photocurrent density during two electrode experiment is attributed to the enhancement of the thermodynamic water splitting potential. [34] The calculated ABPE of pristine and SN1 using equation 3 was found to be 0.69 % at maximum power point potential of, V_{mpp} = 1.35 V

vs. Pt electrode and 1.49 % at 0.71 V vs. Pt electrode and illustrated in Figure 4.14 (b).

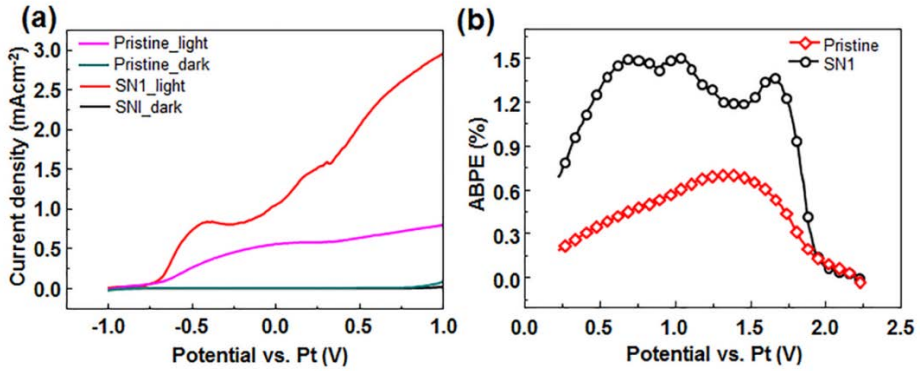

Figure 4.14. (a) Two electrode LSV curves of pristine and SN1 samples. (b) Applied bias photon-to-current conversion efficiency of pristine and SN1 photoanodes.

The chronoamperometry of SN1 samples for an extended period of time was measured to verify the photochemical stability of the codoped photoanode. The measured photocurrent density versus time curve showed that the SN1 photoanode was stable for more than 47.4 hours without any noticeable degradation as shown in Figure 4.15. The photoelectrochemical oxidation of water from codoped samples for an extended period of time confirms that the codoping of nitrogen and sulfur can't impair the intrinsic photochemical stability of TiO_2.

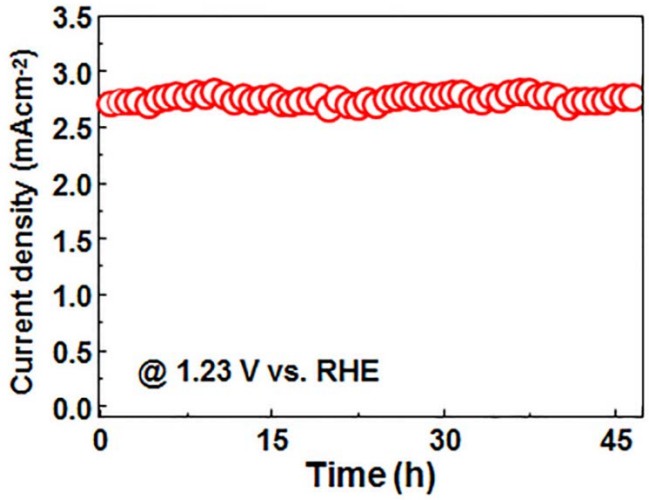

Figure 4.15. Chronoamperometry curve of the SN1 photoanode measured for more than 47 h.

For the better understanding of codopant atom interaction with the host atoms and with each other, the dopant formation energies and optical properties of N-doped, S-doped, and (S, N)-codoped TiO_2 have studied using density functional theory (DFT) (See Section 4 for more computational details). The dopant formation energy calculation shows nitrogen is found to prefer oxygen substitutional site (N_O) while cation substitutional site is very unstable. Interstitial nitrogen requires much higher formation energy compared to N_O in low oxygen partial pressures, but it become comparable to N_O as the formation energy of N_O increases with O_2 pressure. In the case of sulfur, both anion substitution and cation substitution can exist depending on the chemical environment. In high O_2 pressure region, titanium substitutional sulfur (S_{Ti}) is dominant while oxygen substitutional sulfur (S_O) takes majority in oxygen poor condition. These results are well agrees with the XPS analysis shown in

the figure 4.6. To identify the codoping effect in terms of dopant stability, the formation energies of defect complexes with the sum of isolated dopant formation energies was compared as shown in Figure 4.16 (a); both defect complexes of N_O with S_O ([N_O-S_O]), and N_O with S_{Ti} ([N_O-S_{Ti}]) are more stable than sum of each isolated dopants. Especially for N_O-S_{Ti}, the formation energy

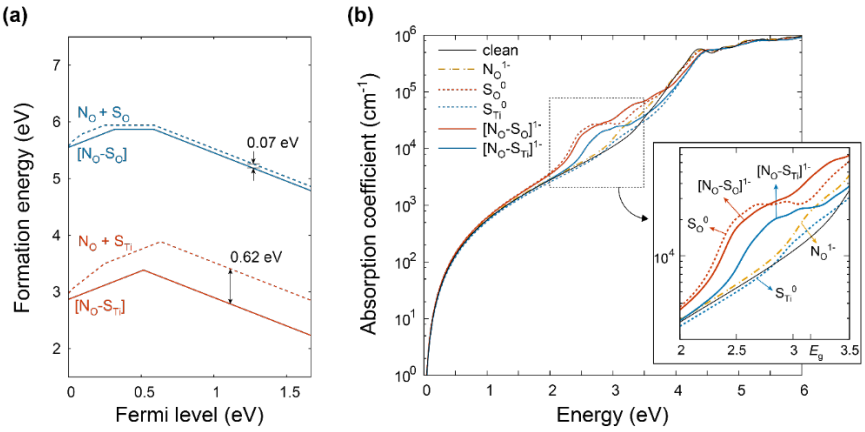

Figure 4.16. (a) Calculated formation energies of defect complexes (solid line) compared to sum of each isolated dopants (dashed line). Chemical potentials are determined from the assumption that chemical potential of oxygen is $E(O_2)$ – 1.5 eV, which is arbitrarily chosen for the good visibility. GGA functional is used for the calculation. (b) Light energy versus absorption coefficient by HSE06 hybrid functional calculation. Absorption coefficient is shown in log scale. The region in the dashed square is magnified in the inset figure.

is lowered by 0.62 eV as N_O and S_{Ti} interact when they are next to each other. This means codoping of nitrogen and sulfur can enhance the dopant stability and higher dopant concentration can be obtained compared to when they are doped separately. Since the binding energy gain of [N_O-S_O] is much smaller

(~0.07 eV) than for [N_O-S_{Ti}], the concentration of [N_O-S_O] in the TiO_2 NRs expected to be negligible. We note that the chemical potentials are chosen in Figure 4.16(a) to provide better visibility for each defect complex, but the relative formation energies can be reversed depending on the chemical environment.

To compare the light absorption efficiency in visible light region, the absorption coefficient of each doped-TiO_2 are calculated in Figure 4.16(b). Each absorption coefficient is calculated using the defective supercells containing each defect or defect complex, corresponding to 1 ~ 2 at. % of dopant concentrations. The charged states of each dopant or dopant complex are determined by assuming that the Fermi level is within the upper region from the mid gap position since undoped TiO_2 is *n*-type semiconductor. First, it is shown that S_O^0 significantly increases absorption in the visible light region while N_O^{1-} and S_{Ti}^0 show almost no contribution in the energy window below 3 eV. However, in the case of [N_O-S_{Ti}] $^{1-}$, the defect complex from codoping makes significant increase of absorption coefficient in the visible light region unlike the monoatomic (sulfur or nitrogen) dopant. This is because the interaction between N_O and S_{Ti} creates deep and localized states in [N_O-S_{Ti}] $^{1-}$ which facilitate the optical absorptions. On the other hand, the [N_O-S_O] $^{1-}$ does not show a significant difference from that of S_O^0. As already shown in Figure 4.16(a), the interaction between neighboring N_O-S_O is weak, so the increase in the visible light region should be solely contributed by S_O^0. We also confirm that the localized state above the VBM of [N_O-S_O] $^{1-}$ is mostly composed with S 3*p* with negligible hybridization with N 2*p*. The dopant configurations and

their partial density of states are shown in Figure 4.17. Since both S^{2-} (S_O^0) and S^{4+} (S_{Ti}^0) are present in our sample, hence both $[N_O\text{-}S_{Ti}]^{1-}$ and S_O^0 contribute to the enhancement of photocatalystic performance and the outperformance of the TiO_2 (S, N) NRs photoanode mostly comes from $[N_O\text{-}S_{Ti}]^{1-}$.

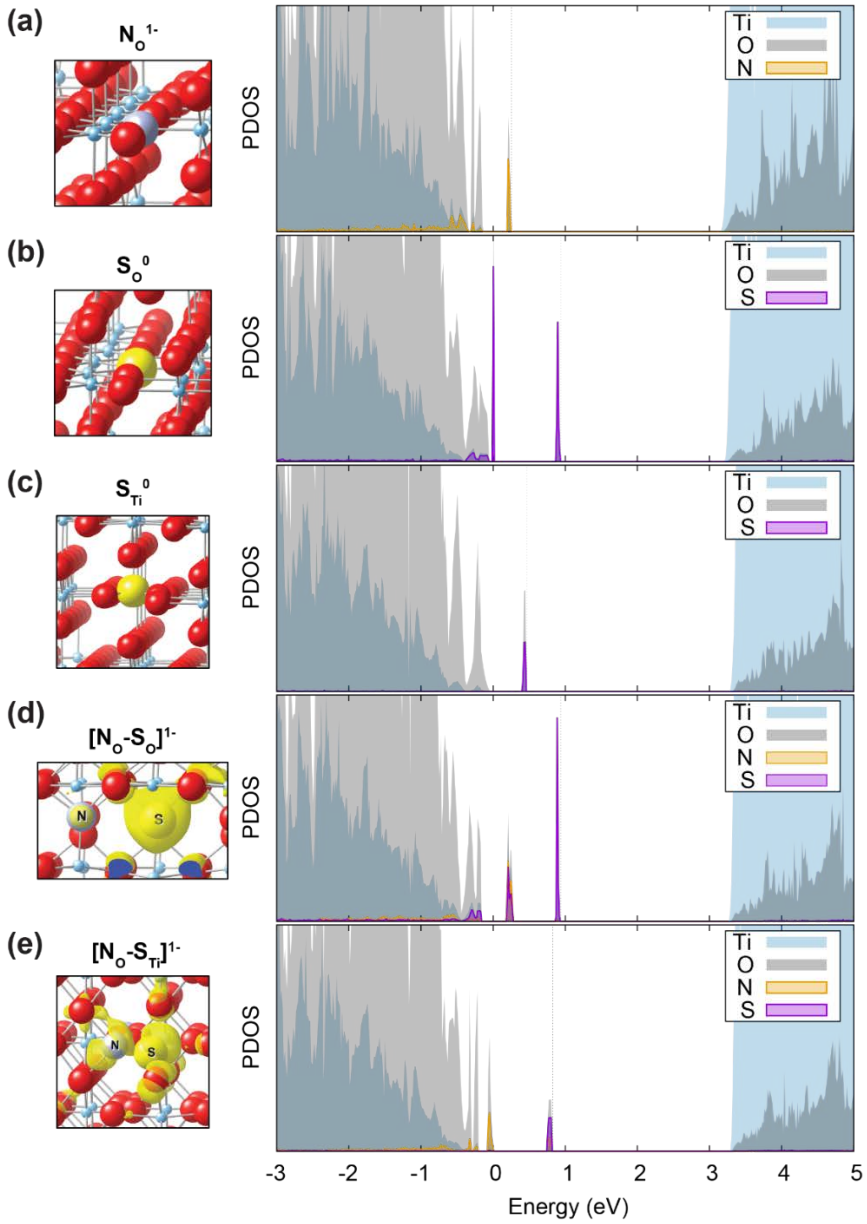

Figure 4.17. Dopant configurations and partial density of states (PDOS) (a) NO^{1-}, (b) S_O^0, (c) S_{Ti}^0, (d) [NO-SO]1-, and (e) [NO-STi] 1-. For (d) and (e), isosurface of highest occupied orbitals is shown in the dopant configuration.

4.6. Conclusion

In this chapter the codoped TiO_2 NRs with sulfur and nitrogen for the application of PEC water splitting was studied. It was found that codoping of nitrogen and sulfur can enhance the photocurrent density of TiO_2 photoanodes without suppressing the photochemical stability of titanium dioxide. The outperformance of codoped TiO_2 NRs photoanodes is due to the intentionally formed impurity energy states at the top of TiO_2 valance band, and enhanced charge transfer and transport properties of the host material. The PEC performance of codoped TiO_2 NRs photoanode is highly dependent on the concentration of codopant precursor. The PEC perforce was decreased when the codopant precursor concentration was increased. The optimum amount of codopant concentration, nitrogen and sulfur, in the TiO_2 NRs shows a 2.82 $mAcm^{-2}$ current density at 1.23 V vs. RHE, which is four times higher than the pristine TiO_2 NRs photoanode, and 1.49% of applied bias-to-current conversion efficiency. Moreover, the codoped TiO_2 NRs photoanode can convert the incident photon to current with 97% efficiency in the UV wavelength region. The interaction of dopant atoms (S, N) with each other and with the host atoms (Ti & O) was studied theoretically, and found that defect complex of $[N_O\text{-}S_{Ti}]$ can enhance both the dopant stability and optical absorption in the visible light region. Although this study only focuses on the codoping of nitrogen and sulfur in TiO_2 NRs, the approach can be extended to other codopant such as acceptor-acceptor, acceptor-donor and donor-donor pairs in the titanium dioxide photoelectrode to enhance the PEC water splitting performance.

4.7. References

1 I. S. Cho, Z. Chen, A. J. Forman, D. R. Kim, P. M. Rao, T. F. Jaramillo, X. Zheng, *Nano Lett*. **2011**, 11, 4978.

2 a) F. E. Osterloh, *Chem. Mater*. **2007**, 20, 35; b)Z. Xu, M. Yin, J. Sun, G. Ding, L. Lu, P. Chang, X. Chen, D. Li, *Nanotechnol*. **2016**, 27, 115401; c) U. Diebold, *Surf. Sci. Rep.* **2003**, 48, 53; d) B. Sun, T. Shi, Z. Peng, W. Sheng, T. Jiang, G. Liao, *Nanoscale Res. Lett*. **2013**, 8, 1.

3 Y.-C. Pu, G. Wang, K.-D. Chang, Y. Ling, Y.-K. Lin, B. C. Fitzmorris, C.-M. Liu, X. Lu, Y. Tong, J. Z. Zhang, *Nano Lett*. **2013**, 13, 3817.

4 G. G. Bessegato, T. T. Guaraldo, M. V. B. Zanoni, Modern Electrochemical Methods in Nano, *Surface and Corrosion Science.* INTECH, Croatia **2014**, 271.

5 S. Y. Chae, P. Sudhagar, A. Fujishima, Y. J. Hwang, O.-S. Joo, *Phys. Chem. Chem. Phys.* **2015**, 17, 7714.

6 a) E. Barborini, A. M. Conti, I. Kholmanov, P. Piseri, A. Podestà, P. Milani, C. Cepek, O. Sakho, R. Macovez, M. Sancrotti, *Adv. Mater*. **2005**, 17, 1842; b) X. Chen, L. Liu, Y. Y. Peter, S. S. Mao, *Sci.* **2011**, 331, 746; c) D.-Y. Wang, C.-H. Li, S.-S. Li, T.-R. Kuo, C.-M. Tsai, T.-R. Chen, Y.-C. Wang, C.-W. Chen, C.-C. *Chen, Sci. Rep.* **2016**, 6; d) Z. Zhang, P. Wang, *Energy Environ. Sci.* **2012**, 5, 6506; e) S. Cho, J.-W. Jang, K.-H. Lee, J. S. Lee, *APL Mater.* **2014**, 2, 010703.

7 X. Pan, M.-Q. Yang, X. Fu, N. Zhang, Y.-J. Xu, *Nanoscale.* **2013**, 5, 3601.

8 H. Wang, G. Wang, Y. Ling, M. Lepert, C. Wang, J. Z. Zhang, Y. Li, *Nanoscale.* **2012**, 4, 1463.

9 S. A. Ansari, M. M. Khan, M. O. Ansari, M. H. Cho, *New J. Chem*. **2016**, 40, 3000.

10 Z. Li, F. Wang, A. Kvit, X. Wang, *J. Phys. Chem. C*. **2015**, 119, 4397.

11 J. Su, Z. Li, Y. Zhang, Y. Wei, X. Wang, *RSC Adv.* **2016**, 6, 16177.

12 J. Tang, A. J. Cowan, J. R. Durrant, D. R. Klug, *J. Phys. Chem. C*. **2011**, 115, 3143.

13 J. Lynch, C. Giannini, J. K. Cooper, A. Loiudice, I. D. Sharp, R. Buonsanti, *J. Phys. Chem. C.* **2015**, 119, 7443.

14 J. H. Park, S. Kim, A. J. Bard, *Nano Lett*. **2006**, 6, 24.

15 T. Ohno, M. Akiyoshi, T. Umebayashi, K. Asai, T. Mitsui, M. Matsumura, *Appl. Catal. A*. **2004**, 265, 115.

16 N. Sharotri, D. Sud, *New J. Chem*. **2015**, 39, 2217.

17 C. Das, P. Roy, M. Yang, H. Jha, P. Schmuki, *Nanoscale*. **2011**, 3, 3094.

18 I. S. Cho, C. H. Lee, Y. Feng, M. Logar, P. M. Rao, L. Cai, D. R. Kim, R. Sinclair, X. Zheng, *Nat. Comm*. **2013**, 4, 1723.

19 a) N. Mathews, M. C. Jacome, C. Angeles-Chavez, J. T. Antonio, *J. Mater. Sci*. Mater. Electron. **2015**, 26, 5574; b) C. L. Luu, Q. T. Nguyen, S. T. Ho, *Adv. Nat. Sci. Nanosci. Nanotechnol.* **2010**, 1, 015008.

20 L. Cai, I. S. Cho, M. Logar, A. Mehta, J. He, C. H. Lee, P. M. Rao, Y. Feng, J. Wilcox, F. B. Prinz, Phys. *Chem. Chem. Phys.* **2014**, 16, 12299.

21 M. M. Momeni, Y. Ghayeb, J. Alloy.Comp. **2015**, 637, 393; H. Zhu, J. Tao, X. Dong, *J. Phys. Chem. C.* **2010**, 114, 2873.

22 Q. Deng, X. Xia, M. Guo, Y. Gao, G. Shao, *Mater. Lett.* **2011**, 65, 2051.

23 C. W. Moon, S. Y. Lee, W. Sohn, D. M. Andoshe, D. H. Kim, K. Hong, H. W. Jang, *Part. Part. Syst.* Charact. **2016**, DOI:10.1002/ppsc.201600340.

24 S. Piskunov, O. Lisovski, J. Begens, D. Bocharov, Y. F. Zhukovskii, M. Wessel, E. Spohr, *J. Phys. Chem. C*. **2015**, 119, 18686.

25 G. Yan, M. Zhang, J. Hou, J. Yang, *Mater. Chem. Phys*. **2011**, 129, 553.

26 J. Chung, J. W. Chung, S.-Y. Kwak, Phys. *Chem. Chem. Phys.* **2015**, 17, 17279.

27 a) P. Ramacharyulu, D. B. Nimbalkar, J. P. Kumar, G. Prasad, S.-C. Ke, *RSC Adv*. 2015, 5, 37096; b) N. Li, X. Zhang, W. Zhou, Z. Liu, G. Xie, Y. Wang, Y. Du, *Inorg. Chem. Front*. **2014**, 1, 521; c) P. Goswami, J. N. Ganguli, *RSC Adv*. **2013**, 3, 8878.

28 a)M. Lu, P. Pichat, *Photocatalysis and water purification: from fundamentals to recent applications*, John Wiley & Sons, Weinheim, Germany **2013**. b) D.-D. Qin, X.-H. Wang, Y. Li, J. Gu, X.-M. Ning, J. Chen, X.-Q. Lu, C.-L. Tao, *J. Phy. Chem. C*. **2016**, 120, 22195.

29 a) J. Rengifo-Herrera, E. Mielczarski, J. Mielczarski, N. Castillo, J. Kiwi, C. Pulgarin, *Appl. Catal. B* Environ. **2008**, 84, 448. b) T. Hirakawa, Y. Nosaka, *J. Phys. Chem. C*. **2008**, 112, 15818.

30 Y.-H. Lin, S.-H. Chou, H. Chu, *J. Nanopart. Res*. **2014**, 16, 1.

31 M. Ge, C. Cao, J. Huang, S. Li, Z. Chen, K.-Q. Zhang, S. Al-Deyab, Y. Lai, *J. Mater. Chem. A*. **2016**, 4, 6772.

32 B. M. Kayes, H. A. Atwater, N. S. Lewis, *J. Appl. Phys*. **2005**, 97, 114302.

33 a) I. S. Cho, J. Choi, K. Zhang, S. J. Kim, M. J. Jeong, L. Cai, T. Park, X. Zheng, J. H. Park, *Nano Lett*. **2015**, 15, 5709; b) G. Ai, R. Mo, H. Li, J. Zhong,

Nanoscale. **2015**, 7, 6722; c) A. Sasinska, T. Singh, S. Wang, S. Mathur, R. Kraehnert, *J. Vac. Sci. Technol. A.* **2015**, 33, 01A152.

34 Z. Chen, H. N. Dinh, E. Miller, SpringerBriefs in Energy, New York. USA **2013**, 49.

35 a) R. E. Hummel, *Electronic properties of materials*, Springer Science & Business Media, NY, USA. **2011**; b) B. G. Streetman, S. Banerjee, *Solid state electronic devices*, Vol. 4, Prentice Hall New Jersey, **2000**; c) R. H. Bube, *Electrons in solids: an introductory survey*, Academic press, NY, USA **1992**. d) W. Choi, A. Termin, M. R. Hoffmann, *J. Phys. Chem*. **1994**, 98, 13669.

36 R. Sharma, P. P. Das, M. Misra, V. Mahajan, J. P. Bock, S. Trigwell, A. S. Biris, M. K. Mazumder, *Nanotechnology*. **2009**, 20, 075704.

37 W. Yang, Y. Yu, M. B. Starr, X. Yin, Z. Li, A. Kvit, S. Wang, P. Zhao, X. Wang, *Nano Lett*. **2015**, 15, 7574.

38 G. Wang, H. Wang, Y. Ling, Y. Tang, X. Yang, R. C. Fitzmorris, C. Wang, J. Z. Zhang, Y. Li, *Nano Lett*. **2011**, 11, 3026.

39 D. M. Andoshe, S. Choi, Y.-S. Shim, S. H. Lee, Y. Kim, C. W. Moon, D. H. Kim, S. Y. Lee, T. Kim, H. K. Park, M. G. Lee, J. M. Jeon, K. T. Nam, M. Kim, J. K. Kim, J. Oh, H. W. Jang. *J. Mater. Chem. A*. **2016**, 4, 9477.

40 Kresse, G. & Hafner, J., *Phys. Rev. B* **47**, 558 (1993).

41 Freysoldt, C., Neugebauer, J., & Van De Walle, C. G., *Phys. Rev. Lett.* **102**, 16402 (2009).

42 Kumagai, Y., & Oba, F., *Phys. Rev. B*, **89**, 1–14 (2014).

Appendix 4


Harvesting Nano-Broccoli Flowers
Dinsefa M. Andoshe, C. W. Moon and Ho Won Jang*
Department of Materials Science and Engineering, Research Institute for Advanced Materials, Seoul National University, Seoul 08826, Republic of Korea *E-mail: hwjang@snu.ac.kr (Ho Won Jang)
SNU 10.0 KV X25.00K W.D 3.1mm 500 nm
Description : TiO2 nano-broccoli flowers were grown on the FTO/ glass using hydrothermal synthesis method

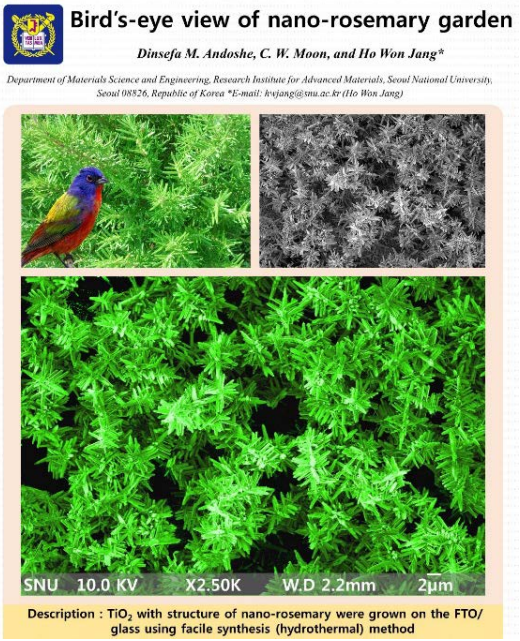
Bird's-eye view of nano-rosemary garden
Dinsefa M. Andoshe, C. W. Moon, and Ho Won Jang*
Department of Materials Science and Engineering, Research Institute for Advanced Materials, Seoul National University, Seoul 08826, Republic of Korea *E-mail: hwjang@snu.ac.kr (Ho Won Jang)
SNU 10.0 KV X2.50K W.D 2.2mm 2μm
Description : TiO2 with structure of nano-rosemary were grown on the FTO/ glass using facile synthesis (hydrothermal) method

Chapter 5

Summary

The drawback of *p*-type Si for PEC water reduction, which are high optical reflectance, high overpotential for solar hydrogen production and photo-electrochemical corrosions were managed by employing different types of earth abundant materials, metal oxide and metal chalcogenide.

To address the aforementioned limitation of *p*-type silicon, a titanium dioxide nanorods were grown on the surface of silicon using facile synthesis methods, hydrothermal method. The heights and diameters of the titanium dioxide nanorods were tuned by controlling the thermal reaction time and growth temperature. The nanorods highly decreased the optical reflectance and overpotential of *p*-type silicon for PEC water reduction. The dramatic reduction of the optical reflectance resulted in enhancement of photocurrent density of the *p*-type silicon photocathode. Furthermore, the *p*-type photocathode was generate for more than three days without noticeable degradation. After very small Pt nanoparticle, 1–2.5 nm diameter, were deposited on the surface of TiO_2 NRs the photocathode (Pt/TiO_2 NRs/*p*-Si) showed turn on potential of 440 mV with short circuit current density of 40 $mAcm^{-2}$.

The incorporation of a MoS_2 thin film with high density of edge sites, which are known to have high catalytic activity for hydrogen evolution reaction, to *p*-type Si is a promising way to develop an efficient photocathode for water

splitting. However, the direct synthesis of MoS_2 thin films on Si substrate using usual chemical vapor deposition techniques remains challenging due to the weak van der Waals force between Si and MoS_2. Therefore, Chapter three of the thesis deals with the direct synthesis of 3-dimensional MoS_2 films on TiO_2-coated 4-inch *p*-type Si substrate. Moreover, the physical, optical and photoelectrochemical properties 3D MoS_2 films in comparison with layered MoS_2 were studied and the 3 D MoS_2 films showed multifunctional properties such as, highly catalytic, antireflective and passivation layer for p-type silicon photocathode. Hence, the three dimensional layer improve the PEC performance of *p*-type silicon.

Chapter 4 describes oxygen evolution reaction, which is the most demanding steps due to the pairing of four electrons and protons to form oxygen-oxygen bond. A titanium dioxide is an attractive candidate for this reaction. However, the photocurrent density of a co-catalysts free TiO_2 is highly suppressed by substantially low photogenerated carrier density, which is resulted from the large optical band gap of TiO_2, and poor carrier kinetics. Therefore, the impact of codopant sulfur and nitrogen in the optical, electrical, photoelectrochemical properties of TiO_2 were studied. The experimental results were supported by analysing the interaction between the codopant atoms and host materials using first-principle density functional theory calculation for all possible dopant configuration complex (S_{Ti}, S_O, N_O and N^{-1}, [S_{Ti} N_O], [S_O N_O]),

and identified how these interaction influence the PEC performance of TiO_2.

List of Publications

1. Dinsefa M. Andoshe, et al. Two-Dimensional Transition Metal Dichalcogenide Nanomaterials for Solar Water Splitting, *Electron. Mater. Lett*. Vol. 11, No. 3 (2015), pp. 323-335.
2. Dinsefa M. Andoshe, et al, wafer-scale antireflective protection layer of solution-processed TiO_2 nanorods for high performance silicon-based water splitting photocathodes *J. Mater. Chem.* A. 2016, 4, 9477.
3. D. H. Kim, D. M. Andoshe, Y. S. Shim, C. W. Moon, W. Sohn, S. Choi, T. L. Kim, M. Lee, H. K. Park, K. T. Hong, K. C. Kwon, J. M. Suh, J. S. Kim, J. H. Lee, and H. W. Jang, Toward High Performance Hematite Nanotube Photoanodes: Charge Transfer Engineering at Heterointerfaces, *ACS Applied Materials & Interfaces* 8, 23793-23800 (2016)
4. C. W. Moon, S. Y. Lee, W. Sohn, Dinsefa M. Andoshe, D. H. Kim, K. Hong, H. W. Jang, Plasmonic Octahedral Gold Nanoparticles of Maximized Near Electromagnetic Fields for Enhancing Catalytic Hole Transfer in Solar Water Splitting, *Part. Part. Syst. Charact.* 34, 1600340 (2017)
5. Kwon, Ki Chang; Choi, Seokhoon; Hong, Kootak, Dinsefa M. Andoshe, Oh, Jeong Hyeon; Kim, Changyeon; Choi, Kyoung Soon; Kim, Soo Young; Ho Won Jang, Tungsten Disulfide Thin Film/*p*-type Si Heterojunction Photocathode for Efficient Photochemical Hydrogen Production, *MRS communication* 2017

6. Ki Chang Kwon and Seokhoon Choi, Joohee Lee, Kootak Hong, Woonbae Sohn, Dinsefa Mensur Andoshe, Kyoung Soon Choi, Seungwu Han, Soo Young Kim and Ho Won Jang, Drastically Enhanced Hydrogen Evolution Activity by 2D to 3D Structural Transition in Anion-Engineered Molybdenum Disuflide Thin Films for Efficient Si-based Water Splitting Photocathodes, *J. Mater. Chem. A.* 2017
7. Dinsefa M. Andoshe, Woonbae Shon, Taemin Ludvic Kim, Ki Chang Kwon, Kootak Hong, Seokhoon Choi, Cheon Woo Moon and Ho Won Jang, Superior Photoelectrochemical Water Oxidation Performance of Titanium Dioxide Nanorods Codoped with Sulfur and Nitrogen,. 2017 (submitted/revised)
8. Dinsefa M. Andoshe, Gangtae Jin, Seokhoon Choi, Ki Chang Kwon, Chang-Soo Lee, Woonbae Sohn, Seung Hee Lee, Jun Min Suh, Jaehyun Park, Hoseok Heo, Jong Kyu Kim, Moon-Ho Jo and Ho Won Jang, Direct assembly of three-dimensional molybdenum disulfide on silicon wafer for efficient photoelectrochemical water reduction. 2017 (submitted)
9. Dinsefa M. Andoshe, and Ho Won Jang, Sulfur inspirited TiO_2 nanorods: A high performance photoanode for oxygen evolution reaction (2017) (in preparation)

국문초록

나노구조와 촉매를 이용한 효율적인 광전기화학적 물분해 전극

전 세계적으로 급증하고 있는 에너지 수요의 대부분은 화석 연료의 연소를 통해 충당하고 있다. 하지만, 화석 연료는 한정된 매장량으로 인해 고갈될 수 있다는 문제와 더불어 연소 생성물로 배출되는 이산화탄소가 지구 온난화를 유발한다는 문제를 가지고 있다. 따라서, 지구 상에 무한히 공급되는 태양 에너지를 이용하여 물을 분해하여, 이를 통해 저장 및 수송 가능한 에너지원인 수소를 생산하는 기술이 주목을 받고 있다. 광전기화학적 물분해 반응은 빛 에너지를 반도체에 조사해 생성된 광전자 · 정공이 전해질 계면으로 수송되어 수소 이온을 수소로 환원시키고, 수산화 이온을 산소로 산화시키는 과정이다. 이 때 사용할 수 있는 반도체 물질 후보군 중에서도 실리콘은 좁은 밴드갭을 가지고 있어 지구상에 조사되는 대부분의 가시광 스펙트럼을 흡수할 수 있다는 장점과, 지각에 풍부하게 존재하는 물질로 가격경쟁력이 있다는 장점이 있다. 하지만, 실리콘 기반 광전극은 수소 생산 반응에 있어 높은 과전압을 필요로 하며, 높은 반사율을

가지고, 전해질 속에서 장기 안정성이 부족하다는 단점이 있다. 이러한 단점들은 용액 공정을 이용하여 길이 및 직경을 제어한 TiO_2 나노 막대를 실리콘 표면에 합성함으로써 극복할 수 있었다. *p*-타입 실리콘 광양전극의 과전압은 TiO2 나노막대를 표면에 성장 시킴에 따라 -0.75 V vs. RHE에서 0.0 V vs. RHE까지 감소하는 것을 확인할 수 있었으며, 반사율은 37% (arithmetic mean) 에서 1.4% 까지 감소하는 것을 확인할 수 있었다. 실리콘의 반사율이 급격하게 감소함에 따라 광양전극의 광전하 생성 효율이 향상되었고, 그 결과 실리콘 광양전극의 포화전류값이 32 mA/cm^2에서 40 mA/cm^2까지 향상되는 것을 확인할 수 있었다. 최종적으로, TiO_2 나노 막대 표면에 1 – 2.5 nm 직경의 Pt 나노입자를 증착한 후에는 440 mV의 개시전위 및 40 mA/cm^2의 단락 전류값을 보이는 우수한 실리콘 기반 광양전극의 특성을 확인할 수 있었다.

효율적인 광전기화학적 물분해 반응을 진행함에 있어, *p*-타입 실리콘의 한계를 극복하기 위해 사용된 두 번째 접근법으로, 3차원 형상을 가진 MoS_2 박막과 TiO_2가 코팅된 Si을 접합하는 연구를 진행하였다. 본 연구에서 사용한 3차원 MoS_2 박막 촉매는 TiO_2가 코팅된 *p*-타입 실리콘 위에 직

접적으로 성장되어, 통상적으로 사용되는 전사법을 이용한 MoS_2 박막과 달리 1) 전사에 소요되는 시간을 단축, 2) 전사에 사용되는 폴리머 잔여물로 인해 발생하는 문제를 사전에 차단, 3) $MoS_2/TiO_2/p$-Si 계면에서의 원활한 전하 수송, 4) MoS_2와 TiO_2 간의 우수한 접합을 기대할 수 있다는 장점이 있다. 또한 MoS_2 박막의 모서리 부분은 수소 발생 반응에 있어 높은 촉매 활성을 보여주는데, 3차원 형상을 가지는 MoS_2 박막은 노출된 모서리가 많다는 특징이 있다. 따라서 3D $MoS_2/TiO_2/p$-Si 광양전극은 0.35 V의 개시 전위 및 28 mA/cm^2의 우수한 광전기화학적 물분해 특성을 나타내었다. 3D $MoS_2/TiO_2/p$-Si 광전극은 TiO_2/p-Si 광전극에 비해 가시광 전 영역에 걸쳐 14% 낮은 반사율을 나타내었고, 이러한 3차원 MoS_2 층의 반사 억제 효과는 TiO_2/p-Si 광전극에 비해 높은 포화 전류를 나타내는 결과를 통해 다시 한 번 확인할 수 있었다. 더불어, 3차원 $MoS_2/TiO_2/p$-Si 광전극은 *p*-타입 실리콘의 단점인 장기 안정성을 개선하여 181 시간 동안 뚜렷한 성능 저하 없이 수소 생산 반응을 지속할 수 있다는 것을 확인하였다.

빛 흡수층 역할을 하는 광음전극으로서의 TiO_2는 가시광 영역에 대한 빛 흡수를 할 수가 없고, 전하 이동성이 떨어진다는 단점이 있다. 이러한 TiO_2

광음전극의 단점은 S (황)과 N (질소) 두 가지 원소의 codoping을 통해 두드러지게 개선할 수 있다는 것을 확인하였다. Codoping 된 TiO_2 (S, N) 나노막대 구조 광음전극은 1.23 V vs. RHE에서 2.82 mA/cm^{2}의 광전류 값을 나타내어 순수한 상태의 TiO_2 나노막대 광음전극의 광전류 (1.23 V vs. RHE에서 0.7 mA/cm^2)에 비해 4배 이상 높은 값을 나타내었다. TiO_2 (S, N) 나노막대 구조 광음전극의 2.82 mA/cm^{2}의 광전류 값은 촉매를 사용하지 않은 TiO_2 광음전극 중에서 보고된 바 중 가장 높은 광전류 값이다. 게다가, TiO_2 (S, N) 나노막대 구조 광음전극의 applied bias photon to-current conversion efficiency (ABPE)와 incident photon-to-current conversion efficiency (IPCE) 값은 각각 1.46%와 97% (360 nm 파장)의 값을 보였다. 모든 도핑물질(S, N)들의 배열은 TiO_2의 전도대와 원자가전자대 사이에 결함/도핑 에너지 준위를 형성한다는 것을 부분 상태밀도 계산을 통해 확인하였다. TiO_2의 [N_O-S_O] 구성은 SO 및 [S_{Ti}-N_O] 구성에 이어 더 높은 광 흡수 계수를 나타냈다. 게다가 S와 N의 codoping은 각각의 원소를 개별적으로 도핑할 때보다 더욱 광흡수계수를 높일 수 있다는 것을 알 수 있었다. 그러나, TiO_2에서 [S_{Ti}-N_O]의 dopant 형성 에너지는 [N_O-S_O]보다 낮아서,

[S_{Ti}-N_O] 구성이 [S_O-N_O] 구성보다 더 존재할 가능성이 높았다. Codoping 된 TiO_2 (S, N) 나노막대 구조 광음전극의 우수한 성능은 주로 E_{CB}와 E_{VB} 사이에 생성된 결함 에너지 상태에 기인한다는 것을 알 수 있었다. S와 N이 codoping된 TiO_2 광음전극은 TiO_2의 안정성에 영향을 미치지 않았으며, 1.23 V vs. RHE에서 58시간 이상의 장기 구동에도 별다른 영향이 없다는 것을 확인하였다.

학번: 2014-31422

딘세파 멘수르